

© 2008

HANHONG CHEN

ALL RIGHTS RESERVED

DYE SENSITIZED SOLAR CELLS USING ZnO NANOTIPS AND Ga DOPED ZnO FILMS

by

HANHONG CHEN

A dissertation submitted to the
Graduate School – New Brunswick
Rutgers, The State University of New Jersey

In partial fulfillment of the requirements

For the degree of
Doctor of Philosophy
Graduate Program in
Electrical and Computer Engineering

Written under the direction of

Professor Yicheng Lu

And approved by

New Brunswick, New Jersey

January, 2008

ABSTRACT OF THE DISSERTATION

DYE SENSITIZED SOLAR CELLS USING ZnO NANOTIPS AND Ga-DOPED ZnO FILMS

By HANGHONG CHEN

Dissertation Director:

Professor Yicheng Lu

Dye sensitized solar cell (DSSC) is a promising and low-cost photovoltaic device. In the DSSC, a monolayer of dye is anchored on the surface of a semiconductor oxide. Photoexcitation takes place inside the dye, and photogenerated charges are then separated at the dye/oxide interface. Nanostructured oxide films are particularly attractive for DSSCs as they provide large surface area for dye anchoring. The crystalline quality of oxide films has significant impact on the charge transport. It is important to reduce the charge traps in the oxide to speed up the charge transport. In the DSSC, the transparent conducting oxide serves as an optical window, which determines the amount of light entering the device, and as the electrode, which extracts photocurrent. In the cell design, the selection of semiconductor oxide and corresponding transparent electrode is critical to achieve efficient light harvesting, charge separation and extraction.

In this dissertation, a novel photoelectrode, consisting of well-aligned ZnO nanotips and a Ga-doped ZnO (GZO) TCO film, is developed for DSSC applications. The n-type semiconductor ZnO nanotips provide large surface area for dye anchoring in conjunction with direct conduction pathways for charge transport, while the GZO film acts as the transparent electrode. ZnO nanotips and GZO films are grown by metalorganic chemical vapor deposition (MOCVD). GZO films (~ 400 nm) with sheet resistance of $\sim 25 \Omega/\text{sq}$ and transmittance over $\sim 85\%$ are achieved. ZnO nanotips have single crystalline quality and show free exciton emissions at room temperature. Photoelectrochemical cells are fabricated using liquid redox electrolyte and semi-solid gel electrolyte, respectively. UV light harvesting, which is directly generated by ZnO photoelectrode, is observed. The DSSC using liquid electrolyte exhibits a quantum efficiency at $\sim 530\text{nm}$ of 65% and power conversion efficiency of 0.77% . By replacing the liquid electrolyte with gel electrolyte in the DSSC with the same structure, the open circuit voltage is increased from 610 mV to 726 mV and the overall power efficiency is increased to 0.89% . The aging testing shows that the DSSC using gel electrolyte has better stability than its liquid electrolyte counterpart.

Dedicated to
My parents and my wife

ACKNOWLEDGEMENTS

I take this opportunity to express my sincere gratitude to my dissertation advisor, Professor Yicheng Lu, for his invaluable guidance during my Ph.D. program study in the Department of Electrical and Computer Engineering. He played an active role in nurturing my research interest and insight throughout my graduate studies and led me to a deep understanding of research methodology in science and technology.

I greatly thank all the members of my dissertation committee, Professor Aurelien Du Pasquier, Professor Paul Panayatatos, Professor Kuang Sheng, and Professor Wei Jiang for devoting their time and expertise to review my dissertation. In addition, I would like to thank Professor Aurelien Du Pasquier for help in the dye sensitized solar cell fabrication and measurements, the results of which I am presenting in this dissertation.

I would like to thank Dr. Yiming Chen, a previous postdoctoral associate in Professor Yicheng Lu's group, for the training me the MOCVD growth technology. My special thanks are owed to all the group members in Professor Lu's group, Mr. Gaurav Saraf, Dr. Jian Zhong, Mr. Jun Zhu, Ms. Ying Chen, Ms. Zheng Zhang, Dr. Pan Wu, Dr. Nuri W. Emanetoglu, Dr. Sriram Muthukumar, Dr. Haifeng Sheng, Mr. Ziqing Duan, and Mr. Pavel Rayes, for their constant help, instructive discussion and friendly collaboration throughout my whole graduate research work in Rutgers University.

TABLE OF CONTENTS

Abstract.....	ii
Acknowledgements.....	v
Table of Contents.....	vi
List of Tables and Illustrations.....	ix
Chapter 1 Introduction.....	1
1.1 Motivation.....	1
1.2 Objectives.....	3
1.3 Dissertation Organization.....	4
Chapter 2 Technical Background	6
2.1 Fundamental Properties of ZnO	6
2.1.1 Crystal Structure of ZnO.....	6
2.1.2 Electrical Properties.....	8
2.1.3 Optical Properties.....	10
2.2 ZnO Transparent Conducting Films.....	12
2.3 Growth Technology of ZnO Nanostructures.....	14
2.3.1 Catalyst Assisted Growth.....	15
2.3.2 Chemical Vapor Deposition.....	18
2.3.3 Thermal Evaporation and Condensation.....	21
2.3.4 Chemical Solution Synthesis.....	23
2.4 Dye Sensitized Solar Cells.....	24
2.5 Metalorganic Chemical Vapor Deposition	32

2.5.1 Rutgers MOCVD System.....	33
2.5.2 Chemicals and Reactions.....	37
2.6 Summary.....	40
Chapter 3 Ga-doped ZnO Transparent Conducting Films.....	42
3.1 Growth Optimization of GZO Films	43
3.2 Electrical and Optical Properties	51
3.3 Summary.....	57
Chapter 4 Growth and Characterization of ZnO Nanotips.....	59
4.1 Growth of ZnO Nanotips on Various Substrates.....	60
4.2 Growth of ZnO Nanotips on GZO Films	71
4.3 Growth Mechanism of ZnO Nanotips.....	75
4.4 Summary.....	81
Chapter 5 ZnO Based Dye Sensitized Solar Cells.....	82
5.1 Device Structure and Operating Principles.....	83
5.2 Solar Cell Testing System.....	89
5.3 DSSC Using Liquid Electrolyte.....	91
5.3.1 ZnO/Liquid Electrolyte Interface.....	91
5.3.2 Photoresponse of ZnO Nanotip-based DSSCs.....	93
5.3.3 Electron Transport in ZnO Nanotips.....	97
5.3.4 Equivalent Circuit Model of DSSCs	100
5.4 DSSCs Using Gel Electrolyte.....	104
5.5 Summary.....	110
Chapter 6 Conclusions and Furture Work	112

6.1 Conclusions.....	112
6.2 Suggestions for Future Work	115
References.....	118
Curriculum Vitae.....	123

Listed Tables

Table 2.1. Some main parameters of wurtzite ZnO bulk crystal. Page 9.

Table 2.2. Vapor pressure and melting point of metalorganic precursors. Page 37.

Listed Illustrations

Figure 2.1. (a) A schematic of ZnO wurtzite crystal structure; (b) The projection of ZnO lattice along the $[11\bar{2}0]$ direction. Page 7.

Figure 2.2. A schematic illustration of a nanoparticle-based dye sensitized solar cell. The device consists of a TCO-coated glass substrate, a dye-sensitized nanoparticle film (thickness of tens of μm), liquid electrolyte and a counter electrode separated by a spacer. Page 24.

Figure 2.3. The molecular structure of ruthenium polypyridine $(\text{Ru}_4\text{N})_2 \text{Ru}(\text{dcbpyH})_2(\text{NCS})_2$ (N719). The tetrabutylammonium ion is denoted as TBA^+ . [81] Page 27.

Figure 2.4. A schematic representation of the energy band diagram of typical dye sensitized solar cells. Page 29.

[Figure 2.5.](#) (a) A schematic diagram of Rutgers MOCVD system for the growth of ZnO film and nanostructures; (b) A schematic diagram of MOCVD growth chamber showing the positions of gas injectors relative to the substrate susceptor. Page 34.

[Figure 3.1.](#) The growth rate of GZO film as a function of substrate temperature. The DEZn and oxygen rate were kept at 100 sccm and 1000 sccm, respectively, the Ga flow rate is kept at 10 sccm. The DEZn and TEGa were kept at 19 °C and 22 °C, respectively. Page 46.

[Figure 3.2.](#) Field emission scanning electron microscope (FE-SEM) images of GZO films grown on different substrate temperature: (a) 380 °C; (b) 450 °C. Page 49.

[Figure 3.3.](#) X-ray diffraction (XRD) spectra of Ga-doped ZnO films grown on glass at substrate temperature of (a) 370 °C; (b) 450 °C. Page 50.

[Figure 3.4.](#) Temperature dependence of electron mobility μ and resistivity ρ of Ga-doped ZnO TCO films. The flow rates of DEZn and TEGa are kept at 100 sccm and 10 sccm, and the GZO films grown at different temperature have the same nominal Ga composition. Page 53.

[Figure 3.5.](#) Electron mobility μ and resistivity ρ of Ga-doped ZnO films as a function of TEGa flow rate. The growth temperature of GZO films is kept at ~400 °C. The DEZn and oxygen flow rate are kept at 100 sccm and 1000 sccm, respectively. Page 54.

[Figure 3.6](#). Transmission spectra of undoped ZnO and Ga-doped ZnO films grown at the similar conditions. The thickness of undoped ZnO and GZO films is ~ 400 nm and the GZO film has a sheet resistance of $\sim 25 \Omega/\text{sq}$. Page 56.

[Figure 4.1](#). Field emission scanning electron microscope (FE-SEM) images of ZnO nanotips grown under un-optimized conditions, (a) on p-Si substrate, (b) on c-Al₂O₃ substrate. Page 60.

[Figure 4.2](#). Field emission scanning electron (FE-SEM) images, showing morphologies of ZnO nanotips under unoptimized growth conditions. Phase reaction results in nanoparticle and the ZnO nanoparticles initiate random nanotip growth on the surface of ZnO nanotips. Page 62.

[Figure 4.3](#). Field emission scanning electron microscope (FE-SEM) images of ZnO nanotips grown at growth temperatures: (a) 350°C, (b) 420°C, (c) 480°C, and (d) 550°C. Page 63.

[Figure 4.4](#). X-ray diffraction (XRD) of ZnO nanotips grown on Si (100) substrates at growth temperatures: (a) 350 °C, (b) 420 °C, (c) 480 °C, and (d) 550 °C. Page 64.

[Figure 4.5](#). Room temperature photoluminescence (PL) spectra of ZnO nanotips grown at substrate temperatures: (a) 350°C, (b) 420°C, (c) 480°C, and (d) 550°C. Page 65.

Figure 4.6. Field emission scanning electron microscope (FE-SEM) images of ZnO nanotips grown on various substrates, (a) GaN/c-Al₂O₃, (b) c-Al₂O₃, (c) Si (100), and (d) glass. Page 66.

Figure 4.7. A field emission scanning electron microscope (FE-SEM) image of ZnO nanotips and ZnO epitaxial films selectively grown on Ti-patterned r-Al₂O₃ substrate. Page 68.

Figure 4.8. X-ray diffraction spectrum of ZnO nanotips and ZnO epitaxial film selectively grown on Ti patterned r-Al₂O₃ substrate. Page 69.

Figure 4.9. Low temperature (12-14 K) micro-cathodoluminescence (MCL) spectra of undoped ZnO nanotips grown on p-Si substrates. The power of the incident electron beam is kept at constant of 2.0 μ W. Curve 1-4 corresponding to the electron beam energy of 1.0 KeV, 5.0 KeV, 10 KeV and 20 KeV, respectively. Page 71.

Figure 4.10. A field emission scanning electron microscope (FE-SEM) images of (a) Ga-doped ZnO TCO films; (b) Sequentially grown ZnO nanotips/Ga-doped ZnO film. The Ga-doped ZnO film is grown at low temperature of ~ 400 °C and the undoped ZnO nanotip array is grown at temperature of ~ 470 °C. Page 72.

[Figure 4.11.](#) X-ray diffraction (XRD) spectrum of ZnO nanotips grown on glass substrate, which is grown under the same growth conditions of the ZnO nanotips grown on Ga-doped ZnO film. Page 73.

[Figure 4.12.](#) Room temperature photoluminescence (PL) spectra; (a) GZO film, (b) ZnO nanotips grown on the GZO film. Page 74.

[Figure 4.13.](#) (a) Field emission scanning electron microscope (FE-SEM) image of a ZnO nanotip array, (b) A FE-SEM image of a single ZnO nanotip grown out of a-plane ZnO epitaxial film, (c) a schematic of typical morphology of ZnO crystal, and (d) a schematic showing the growth habitat of ZnO nanotips. Page 77.

[Figure 4.14.](#) Schematic diagrams of laminar gas flow patterns: (a) flow across a flat surface, (b) flow through a circular pipe. Page 79.

[Figure 5.1.](#) A schematic illustration of dye sensitized solar cell using well-aligned ZnO nanotip array and Ga-doped ZnO TCO film as the photoactive electrode. Page 83.

[Figure 5.2.](#) The energy band diagram of ZnO nanotip-based dye sensitized solar cells. Page 84.

Figure 5.3 The schematic illustration of dye RuN_3 molecules anchoring on ZnO surface.

Page 86.

Figure 5.4. Schematic illustration of solar cell testing system, (a) quantum efficiency measurements; (b) power conversion efficiency measurements. Page 89.

Figure 5.5. An incident photon-to-current conversion efficiency (IPCE) spectrum of the ZnO nanotips in contact with the liquid I^-/I_3^- redox electrolyte. Page 92.

Figure 5.6. Incident photon-to-current conversion efficiency (IPCE) spectra of the ZnO nanotip-based dye sensitized solar cells with three different ZnO nanotip length of 0.8 μm , 1.6 μm , and 3.2 μm . Page 93.

Figure 5.7. I - V characteristics of 3.2 μm ZnO nanotip-based dye sensitized cells in the dark and under the illumination of Xe AM 1.5G (100 mW/cm^2) simulated sunlight. Page 95.

Figure 5.8. Power conversion efficiency (η) and short-circuit current (I_{sc}) of DSSCs as a function of ZnO nanotip length. The photoresponse is measured under the illumination of Xe AM 1.5G simulated sunlight (100 mW/cm^2) with a 1.0 cm^2 cell area. Page 96.

[Figure 5.9](#). Electron transport times of DSSCs built from well aligned ZnO nanotips and ZnO nanoparticles as a function of light intensity (monochromatic light ~640 nm). Electron transport times are determined from the short circuit photocurrent response to a small square wave modulation of the light intensity. The inset shows the time transient time response of ZnO nanotips. Page 99.

[Figure 5.10](#). An electrical equivalent circuit model of solar cells. R_s and R_{sh} are resistors that represent electrical losses. Page 101.

[Figure 5.11](#). The experimental and simulated I - V characteristics of ZnO cells built from ZnO nanotips with length of 0.8, 1.6, 3.2 and 4.8 μm . Page 103.

[Figure 5.12](#). Incident photo-to-electrical conversion efficiency (IPCE) spectra of 3.2 μm ZnO nanotip-based dye sensitized solar cells using gel and liquid electrolyte. Page 106.

[Figure 5.13](#) I - V characteristics of DSSCs built from 3.2 μm ZnO nanotips impregnated with both liquid electrolyte and gel electrolyte. The photoresponse is measured under the illumination of Xe AM 1.5G simulated sunlight ($100 \text{ mW}/\text{cm}^2$) with a 1.0 cm^2 cell area. Page 108.

[Figure 5.14](#). Power efficiency changes as a function of thermal stress time under the illumination of halogen light source producing the equivalent of one sun irradiation at the temperature of $\sim 100^\circ\text{C}$. Page 110.

Chapter 1 Introduction

1.1 Motivation

It is projected that the world energy consumption will increase by about 70% between 2000 and 2030. Fossil fuels, accounting 80% of all the energy consumed world widely, are facing rapid resource depletion. [1] The energy reserves of fossil fuels throughout the whole world in 2002 are projected to last 40 years for oil, 60 years for natural gas and 200 years for coal. Because of a growing demand for energy, combined with the depletion of fossil resources, global warming and climate change, there is an urgent need for environmentally sustainable energy technologies.

Photovoltaic technology provides clean and renewable energy that can reduce the world's dependency on fossil fuels. Currently, the dominant photovoltaic technology is based on solid-state pn junction devices, in which semiconductor absorbers produce electron-hole pairs and the electron-hole pairs are separated by a build-in electrical field in the pn junction to generate electricity. The main semiconductor absorbers used in solid-state solar cells include polycrystalline silicon, [2] amorphous silicon, [3] cadmium telluride (CdTe), [4] and copper indium gallium diselenide Cu (In, Ga)Se₂, [5] etc. These types of solar cells have high power conversion efficiency; however, suffer from high manufacture cost. Dye sensitized solar cell (DSSC) is one of the low cost alternatives for the conventional pn junction based solar cells, and commercially promising because it can be made from low-cost materials and do not require elaborated manufacture facilities.

A typical DSSC consists of a dye sensitized photoelectrode, electrolyte, and a counter electrode. The photoelectrode is composed of a semiconductor oxide film and a transparent conducting oxide (TCO) film. As the light-harvesting dye is present in a monolayer, the surface area of the semiconductor oxide must be substantial. Nanostructured materials have high surface-to-volume ratio, therefore, are particularly suitable for anchoring dye molecule. Since a power conversion efficiency of 10.4% was demonstrated by Grätzel, dye-sensitized TiO₂ nanoporous films have been at the forefront of research for DSSCs. [6,7] The electron transport in the semiconductor oxide is dominated by diffusion, so it is important to reduce charge traps in the nanoscale oxide film to speed up the charge transport. However, nanoparticle films usually have high defect density and large interface area, which act as charge traps. The electron transport in nanoparticle films relies on a trapping-detrapping process, a slow mechanism that reduces the charge extraction efficiency. If direct conduction pathways from the point of electron generation to the collecting electrode existed, the electron transport efficiency will be significantly improved.

In the DSSC, the transparent conducting oxide serves as an optical window, which determines the amount of light entering the device, and as the electrode, which extracts photocurrent. Indium doped tin oxide (ITO) and fluorinated tin oxide (FTO) are the most widely used TCO materials, [8,9] however, the scarcity and high cost of indium and toxicity of tin oxide have limited their large-scale use in these devices. In cell design, the selection of semiconductor oxide and corresponding transparent electrode is critical to achieve efficient light harvesting, charge dissociation and extraction.

ZnO is another attractive, but less explored, wide band gap semiconductor oxide for DSSCs. Due to its multi-functionalities and easy synthesis of various low dimensional structures, ZnO material has stimulated growing research interest in recent years. [10,11] DSSCs built from ZnO nanoparticles have achieved the second highest efficiencies after TiO₂. [12] Ga-doped ZnO (GZO) is also a promising TCO alternative, as it offers advantages, such as abundant source material, low cost, and non-toxicity. Recently, Ga-doped ZnO achieved low sheet resistance and high transmittance, which is close to ITO and FTO. [13,14] Hence, both ZnO nanostructures and GZO films are promising materials for DSSCs. If ZnO nanostructures and GZO films can be sequentially grown on low-cost substrates at low growth temperature, it provides a low cost and high efficient photoelectrode for DSSC applications.

1.2 Objectives

In this dissertation, we investigate the growth of ZnO nanotips and GZO films using metalorganic chemical vapor deposition (MOCVD), and explore their applications in the DSSCs. We optimize the growth parameters, such as chamber pressure, substrate temperature, and metalorganic precursors flow rates and ratios. The morphology, crystalline structure, electrical and optical properties are comprehensively characterized using various characterization tools, such as X-ray diffraction (XRD), Field emission scanning electron microscopy (FE-SEM), transmission spectrometry, photoluminescence spectrometry (PL), cathodoluminescence (CL) spectrometry and Hall measurements.

After optimizing the growth parameters of GZO films and ZnO nanotips, we integrate ZnO nanotips and GZO films on glass substrates through temperature-modulated

MOCVD growth. We optimize the thickness of GZO films and Ga doping level to balance the sheet resistance and transmittance for transparent electrodes. We also optimize the growth of ZnO nanotips on the GZO films to achieve high aspect ratio and maximize the surface area of ZnO nanotip array for dye anchoring.

The hybrid structure of ZnO nanotips/GZO is sensitized with light-harvesting dye molecules and photoelectrochemical cells are fabricated using both liquid redox and semi-solid gel electrolytes. The solar cell process conditions are optimized. The quantum efficiency and energy conversion efficiency are characterized. The charge transfer at the ZnO/dye interface is studied by time-dependant photocurrent response measurements. The I - V characteristics of solar cells are simulated using a one-diode equivalent circuit model to identify the limiting factors for cell performance. The stability of the DSSCs is studied by aging test.

1.3 Dissertation Organization

In Chapter 1, the motivation and objective for the research work of this dissertation is introduced. An overview of technical background is presented in Chapter 2. The following topics are covered: crystalline structure of ZnO, electrical and optical properties, ZnO transparent conducting oxide, growth technologies of various ZnO nanostructures, principles of dye sensitized solar cells, the current progress of ZnO materials for dye-sensitized solar cells applications. The Rutgers MOCVD growth system is introduced and the specific design considerations associated with ZnO material growth are discussed. In Chapter 3, the growth optimization and characterization of Ga-doped ZnO TCO films is discussed in detail. The optimization of ZnO nanotips, and

comprehensive characterization of ZnO nanotips, the growth mechanism of forming well-aligned ZnO nanotips is discussed in Chapter 4. In Chapter 5, the prototype ZnO-based dye sensitized solar cells is demonstrated. ZnO-based DSSCs using both liquid and gel electrolyte are fabricated and the spectral response and I - V characteristics under simulated solar illumination are studied. The parameters of solar cells are analyzed using a one-diode equivalent circuit model. The device stability is studied by aging test. Finally, conclusions and recommendations for future work are presented in Chapter 6.

Chapter 2 Technical Background

2.1 Fundamental Properties of ZnO

2.1.1 Crystal Structure of ZnO

ZnO crystal has a wurzite hexagonal structure (space group $P6_3mc$) with lattice parameters $a = 3.24982 \text{ \AA}$ and $c = 5.20661 \text{ \AA}$. The crystal structure of ZnO can be described as two interpenetrating hexagonal-close-packed (hcp) sublattices, each of which consists of one type of atom displaced with respect to each other along the c-axis direction by the amount of bond length of Zn-O. The ratio of lattice parameter $c:a$ is 1.602, which is slightly less than the value of 1.633 for ideal hexagonal close packed structures. The Zn-O bond length is 1.992 \AA parallel to the c-axis. In ZnO unit cell, O^{2-} ions (by convention) occupy the (0, 0, 0) and (0.6667, 0.3333, 0.5) positions, Zn^{2+} ions occupy the (0, 0, 0.3825) and (0.6667, 0.3333, 0.8825) positions. The crystal structure of ZnO and its projection along ZnO $[11\bar{2}0]$ direction are shown in [Figure 2.1](#).

The tetrahedral coordination in ZnO results in non-central symmetric structure, and consequently piezoelectricity and pyroelectricity. The main low-index planes in ZnO include ZnO (0001), ZnO(000 $\bar{1}$), m-plane ZnO(10 $\bar{1}0$), and a-plane ZnO(11 $\bar{2}0$). The alternating positively charged Zn-terminated (0001) planes and negatively charged O-terminated (000 $\bar{1}$) planes creates a normal dipole moment and spontaneous polarization along the c-axis direction, resulting in divergence in surface energy. To maintain the structure stability, crystals with polar surfaces generally form facets or exhibit massive

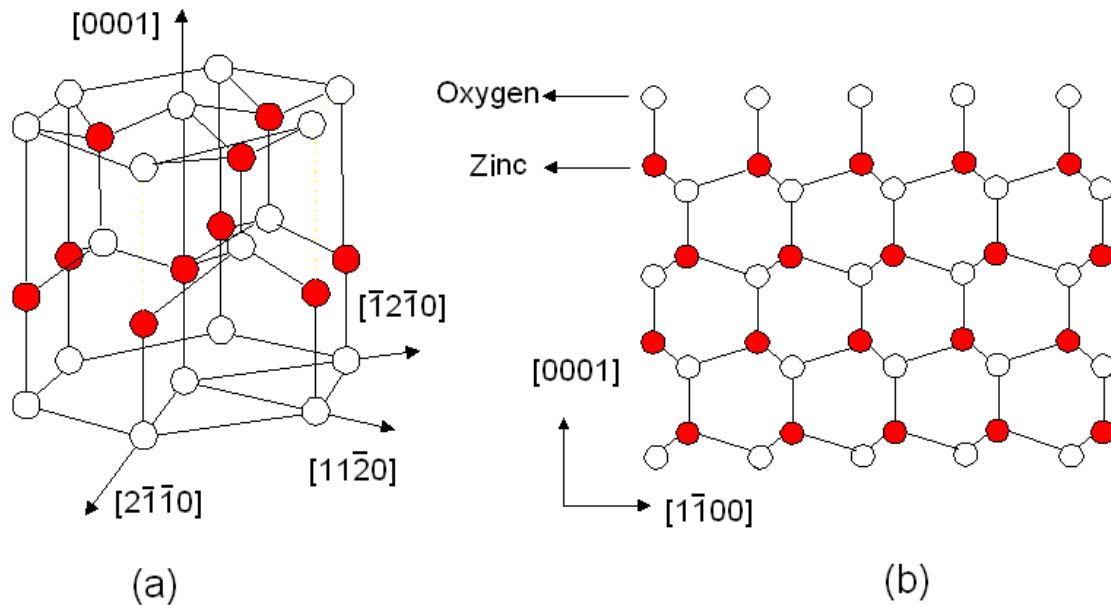


Figure 2.1. (a) A schematic representation of ZnO wurtzite crystal structure; (b) The projection of ZnO lattice along the $[11\bar{2}0]$ direction.

surface reconstructions. ZnO polar surfaces are, however, flat, stable and have no surface reconstruction. Scanning tunnel microscopy (STM) investigation reveals that ZnO (0001) surface has terraces with a single layer step with a height of ~ 2.7 Å. [15,16] A high density of triangular pits and islands with size of several angstroms is consistently observed on the terraces. The stabilization mechanism of the polar Zn-(0001) surface is through the formation of a high density of one-layer high, triangular islands with O-terminated step edges, which results in the cancellation of net dipole moments at the polar surface. The geometric structure of ZnO (000 $\bar{1}$) surfaces has hexagonal terraces of double steps (~ 5.4 Å), and the terraces are typically terminated by step edges including 120° angles. The Zn and O terminated surfaces have different physical and chemical

properties. Two non-polar low index planes of ZnO are the m-plane ZnO(10 $\bar{1}$ 0) and a-plane ZnO(11 $\bar{2}$ 0). The non-polar (10 $\bar{1}$ 0) surface shows well-defined flat terraces separated by mono-atomic steps, running either along the [0001] or $[1\bar{2}10]$ directions. ZnO (11 $\bar{2}$ 0) plane is the roughest of all four low-indexed surfaces, and it has wide and deep grooves running along the $[1\bar{1}00]$ direction, and the two sides of the grooves are parallel to the polar (0001) and (000 $\bar{1}$) planes.

2.1.2 Electrical Properties

The band structure of a semiconductor material is important for fundamental scientific understanding of its electrical and optical properties as well as for determining its potential applications. The conduction band of wurtzite ZnO is mainly constructed from the *s*-like state having Γ_7^c symmetry, whereas the valence band is a *p*-like state, which is split into three bands due to the influence of crystal-field and spin-orbit interactions. [17] The near-band-gap intrinsic absorption and emission spectrum is dominated by transition between the three valence bands and the conduction band. The related free-exciton transitions from the conduction band to these three valence bands or vice versa are usually denoted by *A* (also referred to as the heavy hole), *B* (also referred to as the light hole), and *C* (also referred to as crystal-field split band). ZnO has a direct band gap of 3.37 eV at room temperature. [18] ZnO has an exciton binding energy as high as 60 meV at room temperature, which is much larger than those of other wide band semiconductors like ZnSe (22 meV) and GaN (29 meV). Stable excitons can survive up to room temperature, which theoretically facilitates low-threshold voltage stimulated emission for

light emitting devices. [19] The main physical parameters of ZnO bulk crystal are listed in Table 2.1.

Table 2.1. Some main parameters of wurtzite ZnO bulk crystal. [Ref 20]

Physical Parameters	Values
Space group, lattice type	P6 ₃ mc (Wurtzite)
Lattice constant, (Å)	a = 3.24982; c = 5.20661
Thermal expansion coefficient (@ 500°C (10 ⁻⁶ K ⁻¹))	a = 8.2; c = 4.9
Band gap E _g (RT), (eV))	3.37
Exciton bonding energy, (meV)	60
Electron effective mass m [*] /m _e	0.24
Hall mobility constant of electrons, cm ² /V·s	120
Static dielectric constant (ε ₀)	7.77 for E⊥c, 8.91 for E//c
High frequency dielectric constant (ε _∞)	3.70 for E⊥c, 3.78 for E//c

Undoped ZnO shows *n*-type conductivity because of atom ratio of zinc to oxygen deviation from stoichiometry. The *n*-type conductivity of ZnO may be attributed to native point defects, like oxygen vacancies (V_o) and zinc interstitials (Zn_i). Although it is experimentally known that unintentionally doped ZnO is *n* type, the origin of donors is still in controversy. In literature, it is generally believed that oxygen vacancy is the main reason for *n*-type conductivity [21,22]. On the other hand, Look *et al.* suggested that Zn_i rather than V_o is the dominant native shallow donor in ZnO with an ionization energy of about 30 ~ 50 meV. [23] However, a first-principles study suggested that none of the native defects show a high concentration of shallow donor characteristics. [24] Hydrogen atoms in ZnO lattice are tightly bound to the oxygen atoms, forming O-H bonds with a bond length of about 1.0 Å. Hydrogen in ZnO exists exclusively in the positive charge state, [25,26] it has also been suggested that the *n*-type conductivity of unintentionally

doped ZnO films is due to hydrogen, which acts as a shallow donor with ionization energy about 30 meV. [27] This assumption is valid since hydrogen is always present in all growth methods and can easily diffuse into ZnO in a large amount due to its high diffusivity. First-principles calculations also suggested that unintentionally incorporated hydrogen act as a source of conductivity and behave as a shallow donor in ZnO. [25] The typical background carrier concentration in undoped as-grown ZnO is around 10^{16} cm^{-3} . Intentionally *n*-type doping of ZnO is relatively easy and group-III elements (B, Al, Ga, and In) have been extensively investigated as *n*-type dopants. The p-type conductivity remains the bottleneck for practical devices applications that requires ZnO pn homojunctions. The main limitation of p-type conversion lies in the facts that: (1) the energy level of potential acceptors tend to be deep, and thus have a small fractional ionizations at room temperature; and (2) lattice energetics tends to greatly favor donors. Donors always tend to be dominant, and are easily formed as compensation centers if acceptors are intentionally introduced. [28] Recently, p-type ZnO conductivity has been reported by several researchers and it opens the possibility to fabricate good-quality short wavelength optoelectronic devices. [29,30,31,32] However, the roles of the acceptor dopants and origin of p-type conductivity must be better understood, and the reproducibility and stability of p-type conductivity in ZnO has yet to be improved.

2.1.3 Optical Properties

In very pure ZnO crystals, where the screening effect of free carriers is almost absent, electrons and holes are produced by the absorption of a photon to form excitons, which give rise to sharp emission lines in low temperature PL spectra. The prominent line in

low temperature PL spectra is the A exciton with energy in the range of 3.375 ~3.378 eV and an exciton binding energy of 60 meV. [33] In comparison to the A exciton, the B free exciton is usually weak, and about 12.7 meV apart from the A exciton. Bound excitons are extrinsic transitions and are related to dopants or defects. In high quality ZnO, the neutral shallow donor-bound-excitons (DBE) often dominate due to the presence of unintentional (or doped) donors and/or shallow donor-like defects. The recombination of bound excitons typically gives rise to sharp emission lines with characteristic photon energy to each donors or defects. The most intense DBE line is observed at 3.3605 eV. Many sharp donor- or acceptor-bound excitons were reported in the narrow range of 3.348~3.374 eV. [34] The fine exciton emission lines of I_4 , $I_{6/6a}$, I_8 , I_9 have been resolved using high-resolution photoluminescence (PL) spectroscopy by Meyer. [35] However, the chemical origin and binding energy of the most common donor and acceptor atoms remain unclear. Another characteristic of the neutral-donor-bound-exciton transition is the two-electron satellite transitions (TEST) positioned at 3.3158 eV. These transitions involve radioactive recombination of an exciton bound to a neutral donor leaving the donor in the excited state, leading to a transition energy which is less than the DBE energy by an amount equal to the energy difference between first and ground state of the donor bound excitons and their excited states. With the presence of both donor and acceptor dopants in ZnO, Donor-acceptor-pair (DAP) emission is also identified in ZnO with energy of around 3.22 eV. Longitudinal optical (LO) phonon replicas are also observed in the PL spectra with a characteristic energy separation of 71-73 meV. [36,37]

2.2 ZnO Transparent Conducting Films

Transparent conducting oxide (TCO) films play a critical role in many optoelectronic devices, such as flat panel displays, light emitting diodes (LEDs), photovoltaics, and energy efficient windows. [38,39] Tin-doped indium oxide (ITO) films have been widely used as a TCO films because of their high transmittance in the visible wavelength region and low resistivity comparable to metals. [40] For example, ITO was used in liquid crystal display (LCD) in the "stitching" on an LCD screen, which holds in place the thousands of tiny liquid crystals that produce pictures. However, the indium raw material is very expensive and has led to increasing manufacture cost. Now days, the real concern is whether there is going to be enough indium material to meet industry demand. All these concerns have stimulated extensive research for low cost alternatives. ZnO, doped with group III elements (B, Al, Ga, In), is a promising relatively inexpensive alternative TCO material with electrical and optical properties comparable to those of ITO.

Unintentionally doped semiconductor ZnO shows n-type conductivity due to the presence of point defects such as oxygen vacancies and hydrogen impurities, which act as shallow donors in ZnO. Doping ZnO with group III elements (B, Al, In, Ga) leads to stable n-type conductivity in ZnO films. [41,42,43] The deposition temperature of ZnO based TCO ranges from room temperature to $\sim 400^{\circ}\text{C}$. The electron carrier concentration can be tuned by adjusting the concentration of group III dopants. Aluminum-doped ZnO (AZO) films with a visible transmittance of 85% and a resistivity of $\sim 3 \times 10^{-4} \Omega\cdot\text{cm}$, comparable to that of ITO films, have been achieved by magnetron sputtering. [44] AZO films are stable in Ar gas ambience at temperatures up to 600°C , and in air up to 400°C . [42] The optimized AZO films, i.e. low stress, low resistivity, high Hall mobility, and

high visible wavelength transmittance are obtained at substrate temperatures $\sim 250^{\circ}\text{C}$. [41] Ga-doped ZnO (GZO) films grown on c-plane sapphire substrates by electron beam evaporator are highly transparent ($>80\%$) in the visible–near infrared ranges, and the optical band gap exhibits a blue shift for the as-deposited films. Ga-doped ZnO films with 2 at% Ga doping have achieved resistivities approaching those of ITO. [45,46] The transition from an insulator to a metallic conductor can be explained by the increase of carrier concentration and the formation of a degenerate conduction band due to the shallow ionization energy of the donors, as suggested by Mott. [47] Ga-doped ZnO TCO films exhibited a metallic-semiconductor transition (MST) behavior at low temperature. The $\text{Zn}_{0.95}\text{Ga}_{0.05}\text{O}$ films exhibited a resistivity close to $1.4 \times 10^{-4} \Omega \cdot \text{cm}$ and transmittance $> 80\%$ in the visible wavelength region. [48] It is interesting to find that heavily Ga-doped ZnO TCO films exhibited better reliability. The resistivity of 12.4 wt% Ga-doped ZnO films is $1.3 \times 10^{-3} \Omega \cdot \text{cm}$ and changes by less than 3% over a 2000-hour reliability test at a temperature of 85°C and a humidity of 85%. [49]

ZnO TCO films have been widely used in thin film solar cells as the front windows and transparent electrodes. [50] In $\text{Cu}(\text{In}, \text{Ga})\text{Se}_2$ devices, textured ZnO TCO can significantly improve the light absorption. [51] Recently, it was found that ZnO TCO film could be used as the transparent electrode for p-type GaN. [52,53] The efficiency of GaN light-emitting devices is significantly affected by the transparent ohmic contacts to p-type GaN. Contacts with low specific resistance, high thermal stability, and high transparency are of great importance in improving the efficiency of the light output of GaN LEDs. Indium-oxide-doped ZnO (IZO) has also been reported for transparent ohmic

contact to the *p*-GaN. The light output power of an LED with an IZO/*p*-GaN contact was improved by 34% compared to that of a GaN LED with a Ni/Au ohmic contact. [54]

2.3 Growth Technology of ZnO Nanostructures

Nanomaterials possess grain sizes on the order of less than 100 nm. They manifest extremely fascinating and useful properties, which can be exploited for a variety of applications. Since nanomaterials possess unique chemical, physical, and physical, electrical and optical properties, they can be used for a wide variety of device applications. The applications of nanomaterials includes nanoscale electronic devices such as transistors, resistors, and capacitors, and gas sensors and biosensor employing their high sensitivity to the changes in various parameters, they are designed to measure, A variety of materials, such as Si, GaAs, GaN, ZnO, TiO₂ have been extensively investigated. One-dimensional (1D) ZnO nanostructures, such as rods, wires, belts and tubes, have attracted much attention due to their unique physical, electrical and optical properties. [55] ZnO nanostructures are useful for understanding the dependence of physical, electrical, and optical properties on crystal dimensionality. ZnO nanostructures are also promising building blocks for nano-electronic and nano-optoelectronic devices. For example, low dimensional ZnO nanostructures are expected to further lower the lasing threshold due to carrier confinement effects; ZnO nanostructures are also expected to play an important role as both interconnects and functional units in fabricating electronic, optoelectronic, electrochemical, and electromechanical nano-scale devices.

In the past decade, various growth technologies have been developed for the synthesis of ZnO nanostructures, including chemical vapor transfer and condensation (CVTC)

process via vapor-liquid-solid mechanism (VLS), metalorganic chemical vapor deposition (MOCVD), chemical vapor deposition (CVD), thermal evaporation and condensation, and synthesis through chemical solutions. Each technology has its intrinsic advantages and therefore is suitable for specific applications.

2.3.1 Catalyst Assisted Growth

Catalyst assisted growth is one of the most widely used techniques for the synthesis of ZnO nanostructures. It has certain advantages, such as simple system design, fast growth rate, and low cost. The synthesis of ZnO nanostructures is usually carried out in a horizontal quartz tube furnace. ZnO and graphite powder mixture is used as the Zn source, and Ar/O₂ mixture as the carrier gas. The source materials are placed in an alumina boat positioned at the center of the tube furnace, where the temperature is the highest. The substrates are placed in the downstream of the carrier gas flow. Zn vapor are generated by the reduction of ZnO powder by graphite. As the Zn vapor is transferred to the substrates, the nucleation and growth of ZnO nanostructures take place on the catalyst particles. [56]

A well-accepted mechanism of the CVTC process is the so-called vapor-liquid-solid (VLS) mechanism, which was first proposed by Wagner and Ellis to produce micrometer-sized whiskers in the 1960s. [57,58] According to the VLS mechanism, the precursor Zn vapor forms a eutectic liquid with the catalyst at a temperature higher than its eutectic point. Gold and tin have been explored as the catalyst metal for ZnO nanowire growth. Zn forms eutectic liquid with Au and Sn at the temperature of ~ 642°C (Au content 66wt.%) and 198 °C (Sn 85 wt.%), respectively. [59] The eutectic liquid surface

has a large accommodation coefficient and is therefore a preferred deposition site for incoming Zn atoms. As the eutectic liquid becomes supersaturated with Zn, the growth of ZnO nanowires occurs at the interface of the catalyst and the crystalline substrate. The requirement for the metal catalyzed growth is as following: (a) the catalyst metal must form eutectic liquid with the reactive species Zn; (b) the catalyst metal should be more inertial than Zn; (c) the gas flow rate should be fast to remove the byproducts quickly, and the adopted atoms are either incorporated into ZnO nanostructures or are immediately pumped away; (d) the growth temperature for ZnO nanostructures via VLS mechanism must be above the eutectic temperature.

Taking Au as an example, Au catalyst clusters can be prepared by thermal annealing of thin Au films (2~10 nm) deposited using electron beam evaporation, or by directly spin-coating Au colloidal. The diameters of the ZnO nanowires are determined by the size of the alloy droplet, which is in turn determined by the original size of the catalyst clusters. With proper control of the growth conditions, such as substrate temperature, chamber pressure, and gas flow pattern, various ZnO nanostructures, including nanowires, nanotubes, nanobelts, nanorings *etc.* have been synthesized. [55,60] By carefully tuning the ratio of the oxygen partial pressure and the Zn vapor pressure, ZnO tetrapods with different size have been synthesized. [61] ZnO nanorods grown on a-plane sapphire usually exhibit good alignment along the substrate surface normal, however, on Si substrate, the ZnO nanorods are usually randomly oriented. To achieve aligned ZnO nanorods on Si substrate, a thin layer of ZnO film was first deposited on the Si substrate, serving as the buffer layer. [62]

P. Gao *et al.* also reported the VLS growth of ZnO nanowires using Sn as the catalyst. [63] The ZnO nanostructures are grown on a single-crystal ZnO substrate. It was found that ZnO substrate surface termination has great effects on nanowire growth. Uniform, long, and epitaxially aligned ZnO nanowires are grown on Zn-terminated (0001) surface, indicating that the Zn-terminated (0001) surface is effective for growing nanostructures. Short ZnO nanotrunk are grown on the O-terminated ($000\bar{1}$) surface, indicating the O-terminated ($000\bar{1}$) surface is chemically inert for ZnO growth.

Site-specific growth of ZnO nanowires has been demonstrated on patterned substrates. H. Yan *et al.* have achieved the positional control of ZnO nanowire growth by patterning a-plane Al_2O_3 ($11\bar{2}0$) substrate with Au catalyst. [61] The Au catalytic nanoclusters are prepared from self-aggregation of thin Au films deposited by e-beam evaporation. ZnO nanowire arrays with a narrow diameter distribution are grown on the Au-covered area. X. Wang *et al.* demonstrated the site-specific growth of ZnO nanowires on hexagonal patterned Au substrates by a non-lithographic method. [64] A monolayer of polystyrene micro-spheres was coated on the surface of a- plane Al_2O_3 ($11\bar{2}0$) substrate, which served as the shadow mask for Au deposition. The electron beam evaporated Au species penetrated through the spaces between the polystyrene spheres and formed a network of hexagonal patterns. ZnO nanowire clusters are grown only on the Au catalysts via VLS mechanism and form separated ZnO nanorod clusters. Non-lithographic self-assembly of ZnO nanowires was also demonstrated using anodic alumina oxide (AAO) film as the shadow mask. [65] Nucleation sites of the ZnO nanorods are defined by patterning Au nanodots through the AAO film. ZnAs_2 was used as the ZnO source and the growth is carried in a tube furnace at temperature of 600°C . The self-assembled vertically aligned

ZnO nanorods grown on GaN exhibited hexagonal facets, and have a uniform diameter of 60 nm and a length of 400 nm. The CVTC process is a simple, robust growth technique, and offers flexibility for controlling the morphologies of ZnO nanostructures. However, the growth temperature is usually as high as 900 °C, and aligned ZnO nanostructures have to be grown on crystalline substrates like GaN, SiC and a-Al₂O₃ (11 $\bar{2}$ 0).

2.3.2 Chemical Vapor Deposition

Compared with the CVTC process, the MOCVD technique offers advantages, such as catalyst-free growth, low growth temperature, controllable *in-situ* doping, and precise control of growth rate, high reproducibility, and capability of large-scale mass production. The growth of ZnO nanostructures usually employs Diethylzinc (DEZn) and oxygen as the Zn source and oxidizer, respectively. The vapor phase synthesis involves the following steps: (a) generation of reactants; (b) transportation of reactants to the substrate surface; (c) adsorption of chemicals at the growth surface; (d) nucleation and growth, and (e) removal of unwanted reaction byproducts. Depending on the metalorganic flow rate, the growth dynamics of ZnO can be either mass flow controlled or thermo-diffusion controlled. The growth rate of the Zn-terminated (0001) plane is found to be much faster than that of other crystal planes, thus ZnO nanostructures usually exhibit c-axis orientation. In the case of ZnO nanostructures, in order to achieve higher aspect ratio, high metalorganic mass flow rate is always preferred in order to suppress the in-plane growth, and the growth dynamics should be in the thermo-diffusion controlled region. The typical growth temperature is kept in the range of 300 °C to 500 °C. Due to its low growth temperature, various materials can be used as the substrates, including

GaN, [66] sapphire, [67,68] silicon, [69] and glass. [70] TEM characterization reveals that MOCVD grown ZnO nanorods are of single crystalline quality, and with low density of dislocations and stacking faults. Under the optimized growth conditions, ZnO nanowires exhibit a dominant near band edge (NBE) emission peak at 3.29 eV with negligible deep-level emission.

The formation of ZnO nanostructures during the MOCVD growth is very complicated, not only depending on the growth temperature, pressure, precursor flow rate, and DEZn to O₂ ratio, but also depending on specific chamber design and flow pattern. In certain flow pattern, the chamber pressure has significant effect on the morphology of the ZnO nanostructures. For instance, the morphology changes of ZnO from nanorods to nanotubes, and then to nanowalls were observed as the chamber pressure was reduced from 10 torr to 0.06 torr. [71] Growth temperature determines the kinetic energy and the diffusion length of the reacting species on the growth of the reacting species, and consequently the relaxation time and incorporation rate of the reacting species at the growth surface. Ogata investigated the temperature dependence of ZnO growth mode using MOCVD. [72] It was found that columnar structures of ZnO with small diameter of 10~50 nm are grown at low temperature of about 500 °C. The diameter of the nanorods increases with the increase of growth temperature. The ZnO nanorods turn into flat films at a growth temperature of about 900 °C. Park investigated the effects of growth time on the orientation and morphology of ZnO nanoneedles grown on Si. [69] It was found that ZnO nanoneedles increase in both their diameters and length over growth time. However, the length of the ZnO increases much faster than the diameter, which suggests that nanoneedle formation originates from a higher growth rate along the c-axis direction than

along the in-plane directions. Using synchrotron radiation XRD, it was found that the *c*-orientation of the ZnO nanoneedles was formed within less than 3 minutes growth time and the crystal orientation was unchanged during the subsequent growth.

Substrates also play a significant role in the formation of ZnO nanostructures. The morphology and alignment of ZnO nanowires grown on Si, sapphire, GaN, and single crystal ZnO substrates have been compared under the same growth conditions. [73] It was found that all the ZnO nanowires exhibit a preferred orientation along the *c*-axis with uniform diameter and length. The typical diameter the ZnO nanowire is in the range of 20 nm to 200 nm, and the length of the nanowires is proportional to the growth time. ZnO nanowires grown on crystalline substrates, including *c*-Al₂O₃ (0001), *a*-Al₂O₃ (11 $\bar{2}$ 0), GaN (0001), and ZnO (0001) single crystal substrates all have in-plane epitaxial relation with the substrates, which was verified by X-ray Φ scan. On Si (100) and Si (111) substrates, however, the ZnO nanowires don't exhibit in-plane epitaxial relationship with the substrate. A continuous ZnO layer was observed between the ZnO nanowires and the Si substrates. It was proposed that the ZnO crystallites that nucleated on the amorphous substrate surface may be randomly oriented, and the columnar structure is a result of either competitive blocking of all crystallites whose *c*-axis is pointing away from the surface normal, or of a preferential orientation of the ZnO nuclei on the relatively flat SiO₂ surface as they reach critical size. [70]

Acetylacetonate hydrate (Zn (C₅H₇)₂·xH₂O) is used as the Zn precursor. The Zn (C₅H₇)₂·xH₂O source is vaporized at ~130 °C in the first furnace zone, and the vapor is carried by a N₂/O₂ gas into the second temperature zone of the furnace. The Zn (C₅H₇)₂·xH₂O vapor reacts with the oxygen to form ZnO nanorods on the substrate

surface. The typical growth temperature was kept at ~ 500 °C. Si (100) substrate was used as the substrate with HF treatment. [74] Using HR-TEM, an amorphous layer with thickness of ~ 3 nm was observed at the interface of ZnO nanorods and Si (100). Elemental mapping analyses using EELS found that the amorphous interfacial layer is composed of Si and O elements. No ZnO amorphous or polycrystalline layer was observed at the ZnO/Si interface, indicating that ZnO nanorods nucleate at the Si substrate with preferred c-axis orientation. The as-grown ZnO nanorods exhibited a strong PL emission of ~ 380 nm at room temperature with a negligible green band emission. Due to its simple system design, low cost precursor materials, and low growth temperature, CVD provides a relatively cheap growth method for the synthesis of ZnO nanostructures.

2.3.3 Thermal Evaporation and Condensation

In CVTC process, the formation of eutectic liquid is the critical step to initiate the ZnO nanostructure growth. It is interesting to find that ZnO nanorods can also be synthesized by thermal evaporation without the assistance of a catalyst. R. Wang *et al.* has demonstrated the synthesis of ZnO nanorods using thermal evaporation of ZnO powder. [75] ZnO nanorods are synthesized via a two-step pressure-controlled thermal evaporation. Silicon (100) substrate and zinc powders are inserted into a horizontal quartz tube with 1 mm gap between the sources and the substrate. As distinct from the conventional method of thermal evaporation, neither catalysts nor additives are used. The furnace pressure was 15 torr and the substrate temperature was kept at 550 °C. Well aligned ZnO nanorods are grown on ZnO substrate with hexagonal facets. The ZnO

nanorods have an average diameter of 400 nm with diameters in a range of 15–25 nm. The spacing between individual nanowires is around 60 nm. The nano-scale spatial pattern could be attributed to the adsorption-desorption kinetics and nonlinear diffusion of atoms in a deposited layer. ZnO nanowires on Si layers using GaN buffer have been observed at the low temperature of 500 °C through Zn evaporation and oxidation without the assistance of catalyst. [76] The ZnO nanowires have a nearly uniform diameter of 40 nm and length of 330 nm. The nanowires grow on a wetting film of an interconnected vortex-like structure. An empirical model is proposed to explain the growth process. Spatially resolved CL measurements show a sharp and intense emission (I8 line) from the nanowires, while weak and red shifted luminescence from the wetting layer. The CL indicates the existence of tensile stress in the wetting layer while the nanowires are fully relaxed. ZnO nanowires are also realized in a horizontal resistance furnace by thermal evaporation of Zn powder at 500 °C. The substrates are located generally upstream of the gas flow by distances of 2~3 cm from the Zn source. The tube was evacuated to a background pressure of 10^{-5} mbar. In order to introduce oxygen, the Ar gas was bubbled through DI water. The chamber pressure was kept constant at 200 mbar and the gas flow at 60 sccm. A high-density well-aligned ZnO nanorod array grown on an undoped ZnO film has also been reported using direct evaporation of ZnO powders. [77] The ZnO nanorod array was synthesized in a horizontal tube furnace. The precursor, a molar ratio of 1:1 mixed ZnO powder and graphite powder, is placed in the closed end of a quartz tube. The ZnO film/ Si substrate was placed 7 cm away from the evaporation source in the quartz tube. The quartz tube is then heated to 1150 °C and held at this temperature for 5~10 min. In the meantime, a dry airflow is introduced through the tube furnace and the

pressure in the tube is finally adjusted to about 70 torr. The temperature of the substrate is kept in the range of 700–900 °C. A layer of black product developed on the entire substrate surface.

2.3.4 Chemical Solution Synthesis

A novel chemical route of microemulsions was reported for the growth of well-proportioned and crystallized ZnO nanorods using dodecyl benzene sulfuric acid sodium salt (DBS) as the modifying and protecting agent. [78] The novelty of this procedure can be appreciated by the successfully well-ordered growth of perfect crystallized ZnO nanorods under easily controlled and mild conditions. The *in-situ* reduction in microreactors of the Zn salt originating from microemulsions results in Zn(OH)_2 precursors. By the thermally activated treatment of the precursor-containing solution, the time-dependent growth of ZnO rods will be sluggishly generated. Selective growth of ZnO can also be achieved by patterning the substrate with self-assembled monolayers (SAMs). The process consisted of microcontact printing (μCP) of 11-mercaptopundecanoic acid ($\text{HSC}_{10}\text{H}_{20}\text{COOH}$) SAM micropatterns on a silver coated substrate. The chemically patterned Ag surfaces were then inserted into a dilute aqueous zinc nitrate ($\text{Zn(NO}_3)_2$) and hexamethylenetetramine (HMT; $(\text{CH}_2)_6\text{N}_4$) solution that was held at 50-60 °C for several hours to nucleate and grow ZnO nanorods. Microcontact printing creates a surface that is not homogeneous to ZnO nucleation: high barrier at SAM covered regions and low barrier at bare Ag regions. Consequently, the growth is selective and the organic template controls the spatial placement of ZnO nanorods.

2.4 Dye Sensitized Solar Cells

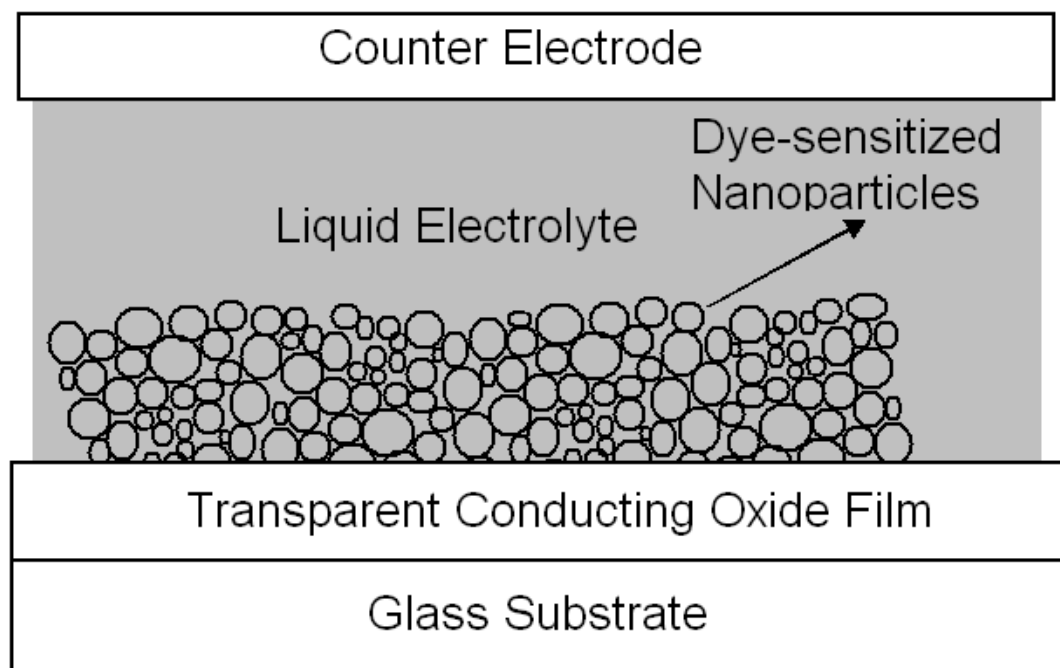


Figure 2.2. A schematic illustration of a nanoparticle-based dye sensitized solar cell. The device consists of a TCO-coated glass substrate, a dye-sensitized nanoparticle film (thickness of tens of μm), liquid electrolyte and a counter electrode separated by a spacer.

The basic function of a solar cell is to absorb incoming light, create electron-hole pairs, and transfer the charges to the collection electrodes. The concept of dye-sensitization was invented in order to find a photoelectrochemical cell based on a semiconductor, which is stable against photocorrosion and yet absorbs light in the visible region. Many semiconductor oxides like TiO_2 , SnO_2 and ZnO satisfy the first requirement; however, they only absorb UV light because of their wide band gap. An alternative approach to extend their spectral response is to attach dye molecules absorbing the visible light onto

the semiconductor surface: dye-sensitization. Grätzel and co-workers first achieved a breakthrough with the use of nanostructured TiO_2 films deposited on a conducting substrate.

Typical DSSCs consist of four components: a working electrode, a monolayer of dye molecules, an electrolyte, and a counter electrode. The working electrode includes a transparent conducting oxide (TCO) film and a nanostructured semiconductor oxide. The typical structure of DSSCs is shown in [Figure 2.2](#). The incoming light is incident on the cell through the TCO electrode. A monolayer of dye molecules attached to the surface of the oxide absorbs the incident photons and generates electron-hole pairs. The charges are dissociated and injected into the conduction band of the oxide. The electrons diffuse through the oxide layer to the collecting electrode. The electrons are then transported through the external circuit and reach the counter electrode. The electrolyte obtains the electrons and restores the oxidized dye molecules. The detailed functionality of each component is described as following:

The energy band gap of dye molecules needs to be adjusted to overlap with the visible light wavelength and harvest the light efficiently. The dye bis(tetrabutylammonium)cis-bis(thiocyanato) bis (2,2'-bipyridine-4 carboxylicacid, 4'-carboxylate) (II) (abbreviated as RuN3) is so far one of the most efficient and most studied dyes for DSSCs. The molecular structure of RuN3 is shown in [Figure 2.3](#). Dye RuN3 is adsorbed on the surface of the nanostructured semiconductor of the working electrode in an ethanolic solution. The bonding between the dye and semiconductor should give high stability, dense packing and efficient carrier injection. The dye exists in two redox states in the solar cell (Ru^{2+} and Ru^{3+}). The valence level of the neutral ruthenium (Ru 4d) contains

eight electrons (d^8), and therefore Ru^{2+} and Ru^{3+} have six and five d-electrons, respectively. The redox potential for the dye (Ru^{2+}/Ru^{3+}) dissolved in ethanol is 1.1 V versus normal hydrogen electrode (NHE), corresponding to the energy -5.6 eV versus to vacuum energy level. The highest occupied molecular orbital (HOMO) are entirely of Ru and NCS character, and the lowest unoccupied molecular orbital (LUMO) are mainly of dicarboxybipyridie (DCBPY) ligand character. The dye absorbs light between 300-800 nm. The absorption maximum of the dye is found to be in the visible wavelength region of 400-550 nm and is due to metal to ligand charge transfer (MLCT) transitions, i.e. an electron localized mainly on the Ru-NCS center in the initial state is transferred to the orbital set on the DCBPY ligand.

The role of the semiconductor is mainly to provide a large surface area and transport electrons towards the collecting electrode. Key factors in device design are the careful control of morphology of the nanostructured semiconductor, leading to the efficient dissociation of generated electron-hole pairs, and subsequent transport of charge carriers. A variety of nanostructured materials, including TiO_2 , SnO_2 , ZnO , have been used as the oxide layer. The nanostructured semiconductor oxide exhibits a large surface area. The oxide layer provides a larger surface area for dye anchoring, and increases the interface between the dye-sensitized semiconductor and the electrolyte. The charge transport properties in the DSSCs remains to be elucidated and the details around the transport mechanism are not fully understood. The macroscopic carrier transport in the nanostructured semiconductor is commonly assumed to be dominated by diffusion because of the absence of a significant electrical potential gradient in the film. [79] In the case of TiO_2 nanoparticle film, a driving force for the electron flow, through the porous

network toward the conducting substrate, may be the equilibrium of the electron density through the film. Several groups have reported the existence of the sub-band gap states lying below the conduction band edge of the nanostructured TiO_2 . These sub-band gap states are believed to be involved in the diffusion process and are discussed mostly in terms of a trapping/detrapping mode, and by a hopping model. The diffusion coefficient and the back reaction rate of electrons have been found to depend strongly on the electron occupation of band gap/conduction band driven states of the TiO_2 nanoparticle films. [80]

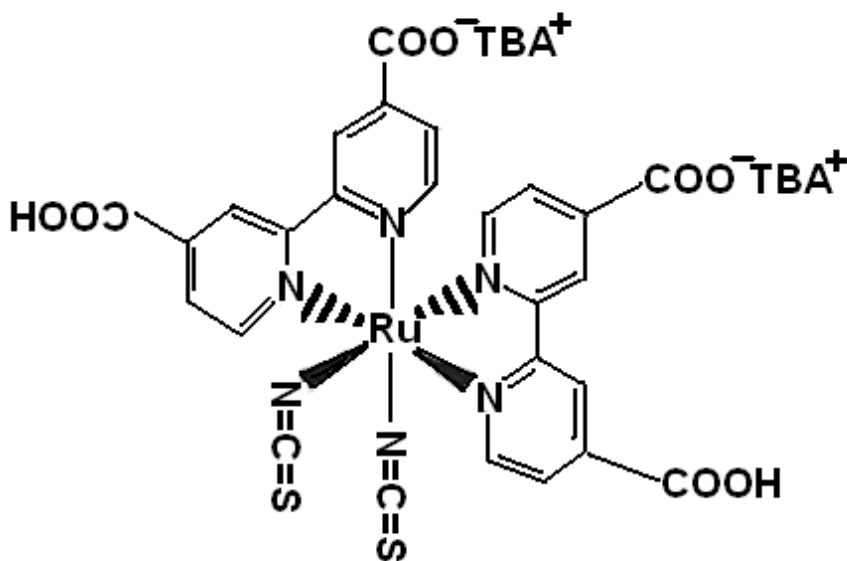


Figure 2.3. The molecular structure of ruthenium polypyridine $(\text{Bu}_4\text{N})_2 \text{Ru}(\text{dcbpyH})_2(\text{NCS})_2$ (RuN3). The tetrabutylammonium ion is denoted as TBA^+ . [81]

ZnO has the similar band gap and electron affinity as TiO_2 , making it a possible candidate as a semiconductor oxide for DSSC. ZnO is a direct wide-band gap semiconductor ($3d^{10}4s^2$) with a band gap of ~ 3.30 eV at room temperature. The valence and the conduction bands have the s-type and p-type characters, respectively. Due to the

ease of synthesizing low dimensional nanostructures, ZnO has stimulated a growing interest, and a variety of ZnO nanostructures, including nanotips, nanotubes, nanobelts and nanorings, have been reported. [82,83,84] Among them, well-aligned ZnO nanotips are promising for DSSC applications, as they provide a direct conduction pathway from the position of electron-hole pair generation to the collecting electrode. The electron transport may benefit from the high electron mobility of ZnO nanotips. The well-aligned ZnO nanotips will provide large surface area for charge separation and direct conduction pathway for charge transfer.

An electrolyte is attracted into the inter-electrode space of the dye-sensitized ZnO nanotips by the capillary force. The electrolyte should have high conductivity and be able to penetrate the ZnO nanotip arrays. The redox system iodide/triiodide dissolved in an organic solvent is the basis of the electrolyte. Organic solvent is used instead of water-based ones, since the dye is unstable in water. The mixing of iodine and a salt of iodide forms the iodide/triiodide. The redox potential of an electrolyte based on 0.5 M LiI and 0.05 M I₂ is about +0.3 V versus NHE, corresponding to an energy level of -5.0 eV from vacuum.

The light is shining on the cell from the TCO side. The TCO film acts as the optical window and the collecting electrode that determines the amount of light that enters the absorber and influences strongly the extraction of the photoelectrical current. A Pt thin film is placed on the electrolyte with a spacer. Platinum electrode will be used as the counter electrode as it provides a high work function of 5.2 eV. Furthermore, the platinum can improve the short circuit current through a catalytic reduction effect of triiodide.

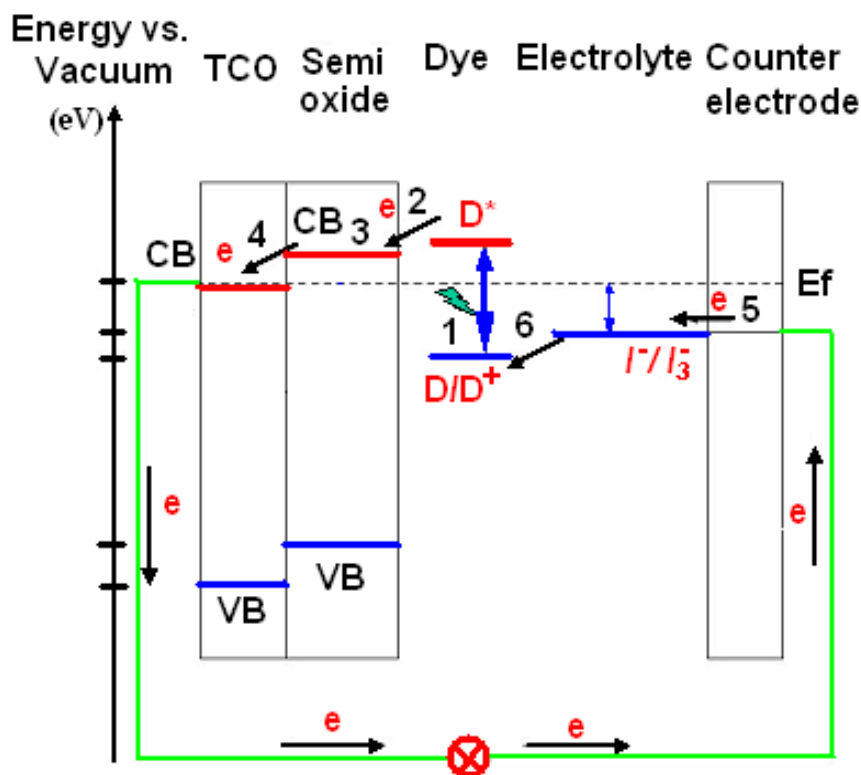


Figure 2.4. A schematic representation of the energy band diagram of typical dye sensitized solar cells.

DSSCs differ from conventional devices in that they separate the function of light absorption from charge carrier transport. The photoexcitation occurs in the dye molecules and the charge separation occurs at the dye/ZnO interface. As the different components of the DSSCs are brought into contact, they will equilibrate by exchanging charges. At dark, the Fermi levels of the working electrode and the counter electrode are in equilibrium with that of the electrolyte redox couple. When the working electrode is illuminated under open-circuit conditions, the Fermi level of the counter electrode and electrolyte is unchanged, whereas the Fermi level of the working electrode changes, producing the

open-circuit voltage (V_{OC}). The energy level diagram of the cell components and electron transfer under illumination is illustrated in [Figure 2.4](#).

The initial charge separation is driven by photoexcitation of the dye (1) and is followed by electron injection into the ZnO conduction band (2), resulting in a positively charged dye (D^+) and negatively charged ZnO nanotips. The electron injection occurs through the carboxylate-zinc linkage. The linkage constitutes a strong coupling to the Zn 4s conduction band orbital. After the injection, the electron is transported through the ZnO nanotips (3) to the back electrode (4) to perform electrical work in the load circuit. The original state of the dye (D) is subsequently restored by electron donation usually from the iodide in the electrolyte (5). The current in the electrolyte is carried to the counter electrode by the redox couple, where the iodide is replenished, in turn, by reduction of triiodide (6). The counter electrode should be efficient in transferring electrons to the electrolyte. The charge separation in the DSSC does not depend on a build-in electrical field, but mainly relies on a competition between forward and backward electron transfer kinetics at the semiconductor/dye/electrolyte interface. The electron injection rate for the excited dye into the conduction band of TiO_2 was found to be in the nanosecond region. The backward electron transfer from the conduction band of the semiconductor to the oxidized dye was found to strongly depend on applied potential. The backward electron transfer between conduction band electron and triiodide has been found to occur in the millisecond time regime. The redox couple of the electrolyte (I/I_3^-) should be aligned so that there is a “down hill pathway” for the electron transport in the closed circuit, i.e. the reaction path is thermodynamically self-sustainable.

The original state of the dye is subsequently restored by electron donation from the hole conductor electrolyte. The regeneration of the sensitizer by the hole conductor intercepts the recapture of the conduction band electron by the oxidized dye. The hole conductor is regenerated in turn at the counter-electrode, and the circuit is completed via electron migration through the external load. The efficiency of solar cells devices is determined by the generation of excitons, and the dissociation and transport of the free charge carriers to the collection electrode. [85]

Dye sensitized solar cells (DSSCs) have attracted much attention since the initial report of O'Regan and Grätzel on realization of high efficiency at low cost. Central to the DSSCs is a thick layer of crystalline nanoparticle TiO_2/ZnO layer (5-20 μm), on which a light absorbing dye/pigment/organometallic complex is anchored. This complex contacts with a redox electrolyte and Pt is used as the electrode. Dye-sensitized TiO_2 nanoparticle films have been at the forefront of research, and photon conversion efficiency of 10.4 % has been demonstrated. [6] However, nanoparticles based DSSCs rely on trap-limited diffusion for electron transport, a slow mechanism that can limit electron extraction efficiency. ZnO nanowires can be grown on various substrates. These nanowires have an average diameter of several tens of nanometers and a length of up to tens of micrometers, resulting in a high aspect ratio, thus providing large surface areas for anchoring the dye molecules, and meanwhile acting as the direct conducting pathways for the photo induced electrons. P. Yang et al. have reported ZnO nanowire-based DSSCs with a full Sun power efficiency of 1.5%. [80] The FTO substrate was first covered with a thin layer of ZnO nanoparticles as the seed layer. ZnO nanowires were grown on FTO substrates from aqueous solutions containing 25 mM zinc nitrate hydrate and polyethylenimine. The ZnO

nanowire arrays are first sensitized in a solution (0.5 mM 1–1) of $(\text{Bu}_4\text{N})_2\text{Ru}(\text{dcbpyH})_2(\text{NCS})_2$ (RuN3 dye) in dry ethanol for one hour and then sandwiched together and bonded with thermally platimzed FTO counter electrodes separated by a gasket (surlyn). The internal space of the nanowires was filled with a liquid electrolyte (0.5 M LiI, 50 mM I_2 , 0.5 M 4-tertbutylpyridine in 3-methoxypropionitrile) by capillary action. ZnO nanowires with a dendritic structure grown by CVD have also been used to construct DSSCs. [86] The dendritic ZnO nanostructures were grown from zinc acetylacetonate hydrate $(\text{Zn}(\text{C}_5\text{H}_7\text{O}_2)_2 \cdot x\text{H}_2\text{O})$ and oxygen by multiple steps. ZnO nanowires with 100 nm diameters nucleate spontaneously on top of a thin polycrystalline ZnO film that deposits on FTO substrate during the initial stages of growth. Dye was loaded by attaching the dye to the nanowire surface in 1.0 mM aqueous KOH solution. It was found that the product of charge injection and collection efficiencies is approximately 70%. This high internal quantum efficiency confirms that the main reason for the lower current density from nanowire-based cells compared to ZnO nanoparticle-based cells is the low light harvesting efficiency. The DSSCs exhibited energy conversion efficiencies of 0.5%.

2.5 Metalorganic Chemical Vapor Deposition

2.5.1 Rutgers MOCVD System

Chemical vapor deposition (CVD) is a process to produce nonvolatile solid thin films using chemically reactive volatile compounds. CVD is a versatile and dynamic technology that has been widely used in the deposition of various semiconductor,

dielectric and metal thin films, particularly high quality epitaxial semiconductor films for solid-state electronics. Since it was first developed in the 1880's in the production of incandescent lamps, this technology has been developing fast. Various CVD technologies now are available for specific material deposition, such as plasma-enhanced CVD (PECVD), low pressure CVD (LPCVD), photo-assisted CVD (photo-CVD), metalorganic CVD (MOCVD), and their hybrids. [87] Among these technologies, MOCVD is particularly important for the epitaxial growth of high quality semiconductor thin films and has been widely used for compound semiconductor material growth. The MOCVD growth system in Rutgers University is shown in [Figure 2.5\(a\)](#). The MOCVD system is composed of three main parts: the reacting chamber, the gas delivering system, and the control system.

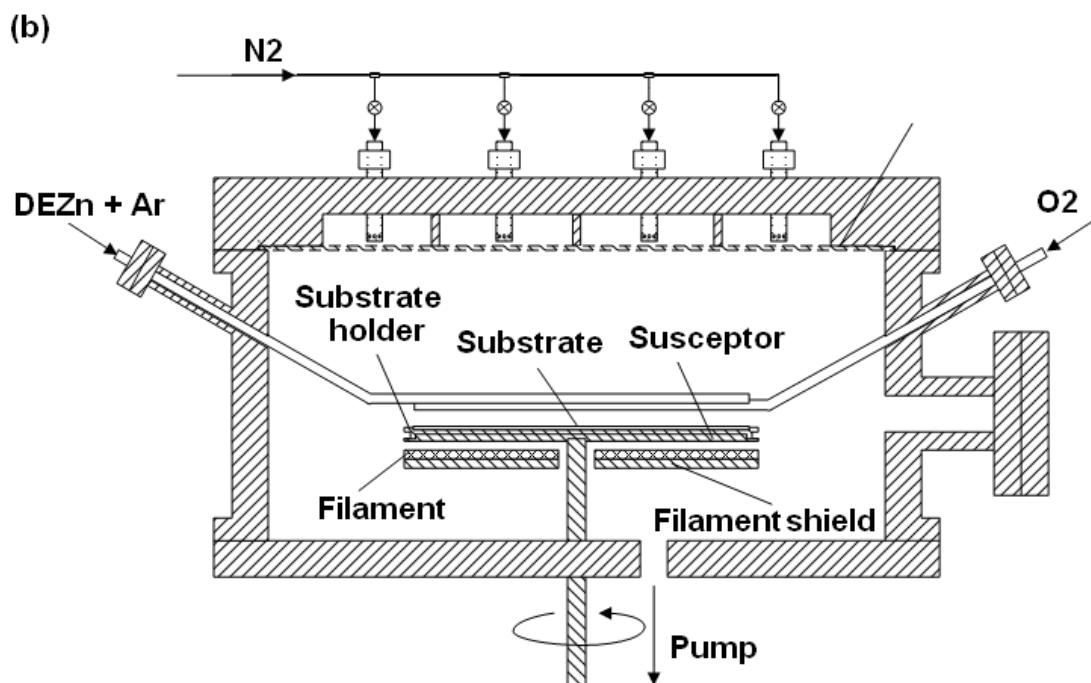
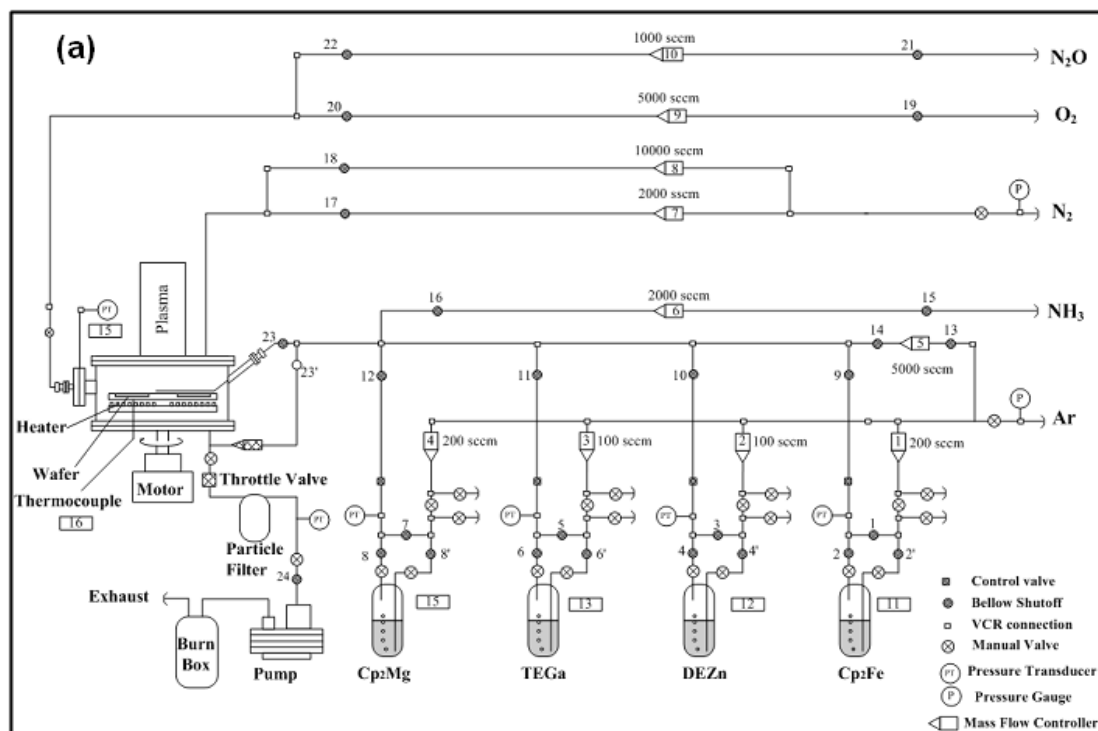


Figure 2.5. (a) A schematic diagram of Rutgers MOCVD system for the growth of ZnO film and nanostructures; (b) A schematic diagram of MOCVD growth chamber showing the positions of gas injectors relative to the substrate susceptor.

The Rutgers MOCVD growth system uses a vertical rotating-disc reactor. The substrates are loaded face-up into a horizontal 3-inch stainless steel susceptor. A resistive filament made from Kanthal AF alloy is placed closely underneath the susceptor to heat the substrates. A thermocouple is inserted into the narrow space between the heating filament and the susceptor to monitor the substrate temperature. The susceptor is connected to a motor via electrical feedthroughs and can rotate at high speed. Metalorganic precursors and gases flow from the top of the susceptor and exit through an exhaust at the bottom. The high-speed rotation of substrates leads to uniform growth of ZnO films and nanostructures. To prevent the phase reaction between the Zn precursor and oxygen, the oxygen and zinc precursors are introduced into the chamber through separated line injectors as shown in [Figure 2.5\(b\)](#). This injector configuration provides the separation of metalorganics from O₂ gas before reaching the substrate surface. A small transit time for the gaseous species is achieved through the high speed of gases injected from the tiny holes of the line injectors and the short distance from the injectors to substrate, resulting in a reduction of gas phase reaction and particle formation. To further reduce the transit time and prevent phase reaction, high top flow of N₂ is introduced from the ceiling to push the metalorganics and oxygen gas further down to the substrates. A microwave plasma system is installed at the top of the reactor for *in-situ* substrate cleaning and surface treatment of as-grown ZnO films and nanostructures.

MOCVD technology utilizes metalorganic compounds as the metal precursors. In the growth of ZnO nanostructures, Diethylzinc (DEZn, Zn(C₂H₅)₂) and high purity oxygen are used as the Zn source and oxidizer, respectively. Triethylgallium (TEGa, Ga(C₂H₅)₃) is used as the Ga doping source. The metalorganic bubblers are placed in thermal bath

tanks and kept at constant temperatures to stabilize the vapor pressure in the bubbler. High purity Ar gas flows through the bubblers and transports the metalorganic vapors into the reactor at constant flow rate. Due to the small flow rate of carrier gas and the high vapor pressure of metalorganics, the metalorganic vapors in the bubblers are always staying in saturated conditions, resulting in a constant delivery rate of metalorganic vapors. At the exit of the bubblers, the metalorganic vapors are further diluted by high purity Ar gas before entering the chamber, resulting in highly uniform gas mixing. The flow rate of the metalorganics is precisely controlled by the carrier gas flow rate. The mass flow rates are controlled by MKS mass flow controller (MFC) with proper range selection. To stabilize the chamber pressure, a throttle valve is installed before the roughing pump to automatically regulate the chamber pressure.

The flow pattern in the chamber is characterized by a boundary layer of gas flux being dragged around the susceptor surface and thrown outwards by centrifugal force. This centrifugal pumping action also sucks down the gases toward the susceptor. When the susceptor is heated, the gas above the susceptor is heated and may rise up due to buoyancy, and then falls again after being re-cooled. This instability develops into turbulence. Turbulence can result in undesirable longer vapor residence time and lead to gas phase reactions. In the case of ZnO growth, such flow patterns have to be avoided since small particles formed due to gas-phase reactions may stay in the reactor and grow, and degrade the quality of ZnO films. These circulating patterns can be avoided by maintaining a large downward gas flow. In the MOCVD, a large volume of top flow N₂ gas is constantly introduced from the chamber ceiling.

2.5.2 Chemicals and Reactions

In organic compounds, the Zn–C bond is predominantly covalent and the C–Zn–C group is linear as a result of *sp*–hybridization. [88] In agreement with their non-polar characteristics, these compounds are among the most volatile metalorganics. Vapor pressures of most metalorganic compounds are given by

$$\log(P(\text{torr})) = B - A/T \quad (2.1)$$

where P (torr) is the metal organic vapor pressure, T (K) is the bubbler temperature, A and B are constants related to the properties of metalorganic materials. The constants A and B of some metalorganic compounds and their vapor pressures at 298K are listed in Table 2.2.

Table 2.2. Vapor pressure and melting point of metalorganic precursors.					
Metalorganic precursor		Pressure at 298 K (mm Hg)	A	B	Melting point (°C)
Zn(C ₂ H ₅) ₂	DEZn	12	2109	8.28	-28
Zn(CH ₃) ₂	DMZn	300	1560	7.80	-42
Ga(C ₂ H ₅) ₃	TEGa	5.0	2162	8.08	-82.3
Mg(C ₅ H ₅) ₂	Cp ₂ Mg	0.04	3556	10.56	176
Fe(C ₅ H ₅) ₂	Cp ₂ Fe	0.005	3680	10.27	171

The flow rate of metalorganic vapors (sccm) is determined by the following equation

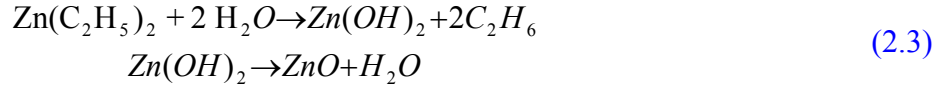
$$F_{MO} = (P_{MO} / P_{Bubbler}) \times F_C \quad (2.2)$$

where F_{MO} and F_C are the flow rates of the metalorganic vapor and carrier gas, respectively. P_{MO} is the vapor pressure of the metalorganic and $P_{Bubbler}$ is the bubbler pressure.

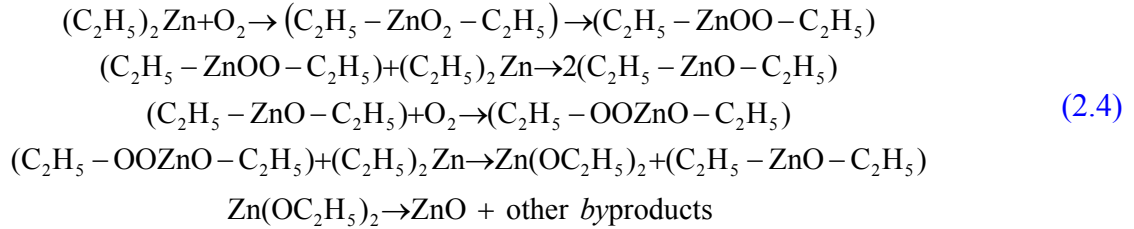
From Eq. 2.2, it is clear that the metalorganic flow is proportional to the metalorganic vapor pressure. The selection of metalorganic sources is an important consideration in MOCVD growth, as it determines the concentration of source material in the reactor to achieve the desired deposition rate. Though Dimethylzinc (DMZn) can be used to achieve high growth rate due to higher vapor pressure, Diethylzinc (DEZn) is more advantageous due to the following reasons:

- (i) In comparison to DMZn, DEZn reacts more steadily with O_2 and H_2O . It is relatively easy to control the growth rate and limit the gas phase reactions, particularly for high quality epitaxial films.
- (ii) When DEZn molecules are absorbed onto the substrate surface, the molecules are thermally cracked and reduced ethyl radicals can be eliminated as ethylene. DMZn may introduce carbon contamination at growth temperatures of $400\text{ }^{\circ}\text{C} \sim 500\text{ }^{\circ}\text{C}$.

Therefore, to reduce gas phase reaction and ease the control of growth rate, we choose DEZn as the zinc precursor. The melting point of DEZn is -28°C , and the boiling point is 117°C and 30°C at pressures of 760 mm Hg and 27 mm Hg, respectively. The strongly electrophilic (accepts an electron) characteristics of zinc ions largely determine the chemical behavior of DEZn. They are electron deficient compounds in that the number of low-lying orbitals available for bonding (four) is greater than the number of bonding electron pairs (two). This presence of vacant orbitals for bonding explains the tendency of DEZn to form complexes with compounds containing hetero-atoms with free electron pairs (O, N, P, S etc.). This serves to explain the great chemical reactivity of DEZn. DEZn is highly susceptible to be attacked by oxygen and water vapor. The reaction of DEZn with water is given by



while the reaction with oxygen is more complicated. [89] A probable reacting route is given by



The MOCVD growth of ZnO crystal includes the following steps:

- (a) The metalorganics DEZn are vaporized in the bubblers and transported to the chamber by the high purity carrier gas. In our system, we use argon gas.
- (b) A relatively stationary boundary layer is formed close to the substrate surface, and the reacting species (metalorganics and oxygen) diffuse through the boundary layer and are absorbed at the growth surface.
- (c) The absorbed species diffuse at the surface of growth planes to the lowest energy positions. The metalorganic molecules react with the oxygen to form ZnO crystals.
- (d) Byproducts such as CH_4 , C_2H_5 , and CO_2 , are volatile. They are desorbed from the growth plane and pumped away.

MOCVD technology offers some advantages for ZnO nanotip growth. First, it has a relatively low growth temperature. The typical growth temperature of ZnO nanostructures using MOCVD is in the range of 350 °C to 500 °C, which is much lower than the typical growth temperature via vapor-liquid solid mechanism (VLS) process

(~950 °C). The low growth temperature is of particularly interest as it opens up the opportunities to grow ZnO on various substrates, therefore extending the realm of ZnO nanostructures for device applications. Secondly, unlike thermal evaporation and condensation process via VLS, no catalysts or ZnO nanoparticle seed layers are required to initiate the ZnO nanotip growth. Hence, as-grown ZnO has high crystalline quality and low impurity concentration. Third, ZnO nanotips grown on lattice mismatched or amorphous substrates also exhibit preferred c-axis orientation as those on lattice matched substrates. It is interesting to find that well-aligned ZnO nanotips can also be grown on lattice-mismatched substrates (Si, c-Al₂O₃, Au) and amorphous substrates (glass and thermally grown SiO₂). Hence, various choices of substrate are available for ZnO nanotip growth, including GaN, c-Al₂O₃, Si, glass and metals like Ti and Au. All the ZnO nanotips grown on these substrates show uniform size and are well aligned along the substrate surface normal. The growth of the well-aligned ZnO nanotips at low temperature is of particularly interest as it provides a way to grow ZnO nanotips on cheap substrates like glass and stainless steel for solar cell applications.

2.6 Summary

In this chapter, an overview of technical background is presented. The following topics are included: (1) fundamental properties of ZnO, (2) ZnO transparent conducting films, (3) growth technology of ZnO nanostructures, (4) dye-sensitized solar cells, and (5) Rutgers MOCVD for ZnO growth. In the first part, a brief introduction of fundamental properties of ZnO, including the crystal structure, electrical properties, and optical properties, is presented. In the second part, the properties and application of ZnO

transparent conducting oxide films is reviewed. In the third part, we summarize the growth technology of ZnO nanostructure, including catalyst associated growth, chemical vapor deposition, thermal evaporation and chemical solution synthesis. The advantage and potential application of each growth technology is discussed. In the fourth part, we introduced the principle and operating principle of dye sensitized solar cells. The recent process of ZnO nanostructured-based dye sensitized solar cells is summarized. Finally, we introduce the Rutgers MOCVD system and the specific reactor design for ZnO material growth is discussed.

Chapter 3 Ga-doped ZnO Transparent Conducting Films

Undoped ZnO shows n-type conductivity due to the existence of native defects such as oxygen vacancy (V_o), zinc interstitials (Zn_i), and hydrogen interstitials in the ZnO lattice. [90,91,92] Even though undoped ZnO films can achieve fairly high carrier concentration, the defects and hydrogen interstitials induced conductivity is thermally unstable and the conductivity is significantly reduced when annealed in oxygen ambience at a temperature of 400 °C. [93] In order to obtain thermally stable conductivity, it is necessary to introduce intentional dopants in the ZnO lattice. According to semiconductor physics theory, the substitution of Zn^{2+} ions with group III ions (B^{3+} , Al^{3+} , Ga^{3+} , In^{3+}) generates extra electrons, resulting in n-type conductivity. It has been reported that the doping of group III elements can significantly increase the conductivity of ZnO material due to the relatively low ionization energy of the dopants. [94,95,96] Among group III elements, gallium has an ionic radius of 0.62Å and a covalent radius of 1.26Å, which is the closest to those of zinc (0.74 Å and 1.31 Å). The bond length of Ga-O (1.97 Å) is close to that of Zn-O (1.86 Å) and offers the advantage of minimizing the deformation of ZnO lattice at high substitutional gallium concentration. [97] Furthermore, gallium has a higher equilibrium oxidation potential and is less reactive with oxygen ambience, making it a better choice of doping candidate.

Both Physical phase deposition (PVD) (such as sputtering and pulse laser deposition) and chemical vapor deposition (CVD) can be used for GZO film deposition. Of these two technologies, CVD has relatively lower capital cost and it is capable of producing mechanically tough films of large areas and acceptable electrical and optical properties.

In PVD, either metallic or metal oxide targets may be used. Metal targets are almost certainly cheaper to manufacture, but have a significant doping problem associated with them. During reactive sputtering, nodules tend to form on the target surface. These distort the distribution of the electric field across the surface and make the rate of erosion (and, consequently, the deposition rate as well) somewhat erratic. If oxide targets are used, radio frequency sputtering must be used. The ceramic targets themselves are typically manufactured by sintering mixtures of individual oxides. The oxide targets are more expensive and present challenging issues of recycling. Although it is straightforward to reprocess a metal target, the target composition may vary with time. Therefore, in considering the manufacturability and cost, CVD is the preferred technique. In this chapter, we will present the growth and characterization of GZO transparent conducting films using MOCVD. Ga-doped ZnO is a promising candidate for cost-effective TCO material. In order to achieve practical applications, it is important to optimize the growth parameters. In this chapter, we focus on the optimization of growth parameters, such as Ga doping level, Zn/O ratio and substrate temperature.

3.1 Growth Optimization of GZO Films

The growth of Ga-doped ZnO (GZO) films is carried out in a vertical flow and rotating disc MOCVD reactor. Diethylzinc ($\text{Zn}(\text{C}_2\text{H}_5)_2$, DEZn) and oxygen are used as Zn precursor and oxidizer, respectively. Triethylgallium ($\text{Ga}(\text{C}_2\text{H}_5)_3$, TEGa) is used as the Ga doping source. The metalorganic bubblers are placed in thermal bath tanks and kept at constant temperatures. High purity argon gas flows through the metalorganic bubblers and transport the precursor vapor to the reactor. DEZn and TEGa vapors are premixed

before entering the chamber and further diluted by high purity Ar gas. DEZn and TEGa react violently with oxygen and phase reaction may take place even at room temperature. In order to suppress the phase reaction, a high flow of nitrogen is further introduced from the top ceiling of the reactor chamber to push the precursors and oxygen gas downwards to the substrates.

The growth rates of ZnO crystal in different low-indexed crystalline directions follow the order: $\text{ZnO}[0001] > \text{ZnO} [01 \bar{1} 0] > \text{ZnO} [01 \bar{1} 1] > \text{ZnO}[000 \bar{1}]$. [98,99] Because of the fastest growth rate along $\text{ZnO} [0001]$ c-axis direction, as-grown ZnO usually exhibits a columnar structure. As the GZO film is used for the purpose of TCO electrodes, the formation of separated columnar structures is undesirable, as they block the lateral current from spreading. In order to obtain a dense GZO film structure, it is necessary to suppress the fast growth rate along the c-axis direction, and the formation of nanotip-like columnar structures.

The MOCVD growth of ZnO crystal involves two stages: the nucleation and subsequent growth. The nucleation process of ZnO film is governed by the Gibbs free energy change ΔG , which is given by

$$\Delta G = \Delta H - T \cdot \Delta S \quad (3.1)$$

where T is the absolute temperature, ΔH is the enthalpy change and ΔS is the entropy change during the chemical reaction.

According to the second law of thermodynamics, the spontaneous chemical reaction occurs when the ΔG is negative. In order to grow dense epitaxial films, it is essential that nuclei form as an oriented seed at very initial growth stage. A small negative value of ΔG , the chemical Gibbs free energy per unit volume, is required to foster a low

nucleation rate of large critical-sized nuclei. The incoming reacting species impinges on the nuclei surface. They diffuse to the lattice sites and are incorporated. Then, in the following growth stage, the crystallites expand laterally and emerge with neighboring ones to form a continuous film. As the crystallites have the in-plane epitaxial relationship with the substrates, the as-grown films exhibit a single crystal quality. In the case of Ga-doped ZnO grown on r-plane sapphire substrates, ZnO films follow epitaxial relationship $\text{ZnO } (11\bar{2}0) // \text{Al}_2\text{O}_3 (01\bar{1}2)$ and $\text{ZnO } [0001] // \text{Al}_2\text{O}_3 [01\bar{1}1]$, implying that the c-plane of GZO films is lying in the growth plane.

On the other hand, if ΔG were large, the likelihood of a high rate of heterogeneous nucleation, or even homogeneous nucleation of solid particles within the gas phase, would be enhanced. The large driving force for chemical reaction tends to promote random orientation and then polycrystalline formation, which is the case of GZO films grown on various lattice-mismatched or amorphous substrates, such as SiO_2 and glass. At the initial nucleation stage, the metalorganic molecules diffuse through the static boundary layer and are chemically absorbed onto the substrate surface. The metalorganic molecules are strongly bound to the oxygen-terminated or hydroxylated surface and form a continuous monolayer at the substrate surface. The strong chemical absorption of metalorganic molecules to hydroxylated surface have been successfully used to realize atomic layer deposition (ALD), in which the metalorganic molecules and oxidizer are released into the chamber alternatively to achieve precise layer-by-layer deposition. [100].

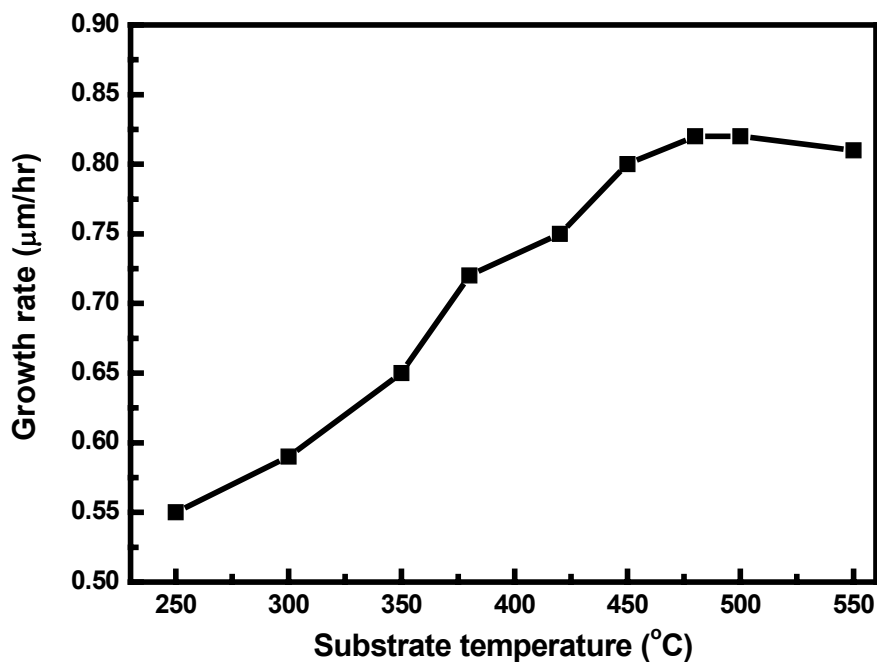


Figure 3.1. The growth rate of GZO film as a function of substrate temperature.

The DEZn and oxygen rate are kept at 100 sccm and 1000 sccm, respectively, the Ga flow rate is kept at 10 sccm. The DEZn and TEGa are kept at 19 °C and 22 °C, respectively.

In MOCVD growth, oxygen and metalorganic vapors are introduced into the chamber simultaneously and reaction rate is much faster compared with ALD technology. With the presence of excessive oxygen, the metalorganic molecules absorbed onto the substrate surface are cracked and oxygen atoms are attached to Zn ions to form strong Zn-O bonds. The $-C_2H_5$ radicals are desorbed from the growth surface and may further oxidized in oxygen ambience and pumped away. The ZnO nuclei are quickly formed at the kinks, ledges, dislocations, etc., which serve to stabilize nuclei of different sizes. Due to the large Gibbs free energy change ΔG , a high nucleation rate of ZnO at heterogeneous

substrate is expected. Since there is no in-plane epitaxial relationship between the nuclei and glass substrates, the initial nucleation at the substrate surface is a random process.

After the formation of initial ZnO nuclei, temperature plays a significant role in subsequent growth stage, therefore determining the morphology and crystalline structure of the GZO films. [Figure 3.1](#) shows the growth rate of the GZO films as a function of substrate temperature. The bubbler pressure of DEZn and TEGa precursor are kept at 700 torr and 800 torr, respectively. The DEZn, TEGa and the oxygen flow rate are kept at 100 sccm, 10 sccm and 1000 sccm, respectively. The high oxygen flow is helpful to improve the stoichiometry of GZO films as ZnO has strong tendency to form oxygen vacancies. As the growth temperature increases from 250 °C to 400 °C, the growth rate linearly increases from 0.55 $\mu\text{m/hr}$ to 0.81 $\mu\text{m/hr}$.

At low growth temperature, the Zn and O reacting species have low kinetic energy. As the Zn and O atoms are adsorbed onto the growth planes, it takes long time to diffuse to the lattice position and the crystallite barely has change to increase in size before surrounded by the newly formed nuclei. Therefore, the growth of GZO film is kinetically limited and the growth rate is independent of the precursor flow rate. As the temperature increases, the kinetic energy of the reacting species increases. The diffusion rates of Zn and O at the growth surface increase, resulting in shorter relaxation time and higher incorporation rate into ZnO lattice and the polycrystalline ZnO has a larger crystalline size. As growth temperature further increases, due to the lowest surface energy of ZnO (002) crystalline planes, the ZnO crystallites quickly elongate along the c-axis direction. The growth rate along c-axis orientation becomes dominant, and the GZO films form textured films with c-axis normal pointing to the direction of the substrate surface

normal. As the substrate temperature further increases beyond 450 °C, the growth rate no longer increases, which implies that the GZO growth is mass flow rate controlled. In order to obtain dense films, we keep the growth temperature below 400 °C. The as-grown polycrystalline films are composed of small size crystallites. A typical morphology of GZO film grown at 380 °C is shown in [Figure 3.2\(a\)](#). The GZO films forms a dense film structure with relative smooth surface. At substrate temperature of ~400 °C, the GZO films start to form columnar structure as shown in [Figure 3.2\(b\)](#).

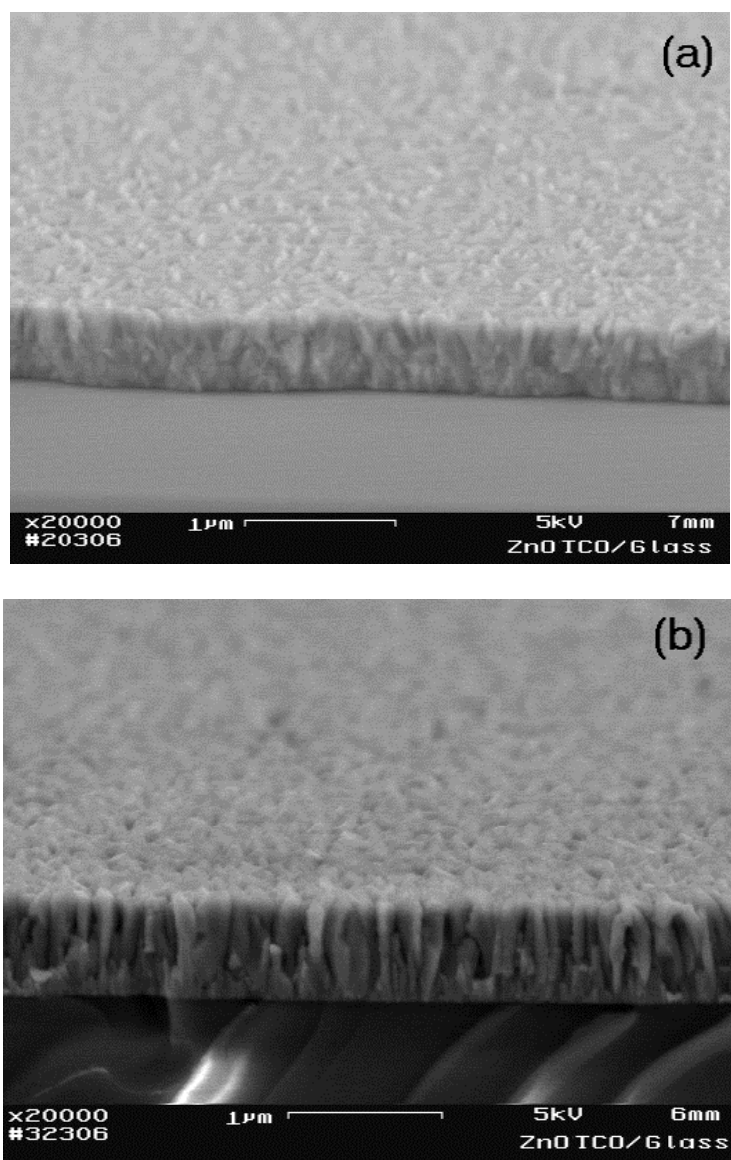


Figure 3.2. Field emission scanning electron microscope (FE-SEM) images of GZO films grown on different nominal substrate temperatures: (a) 380 °C; (b) 450 °C.

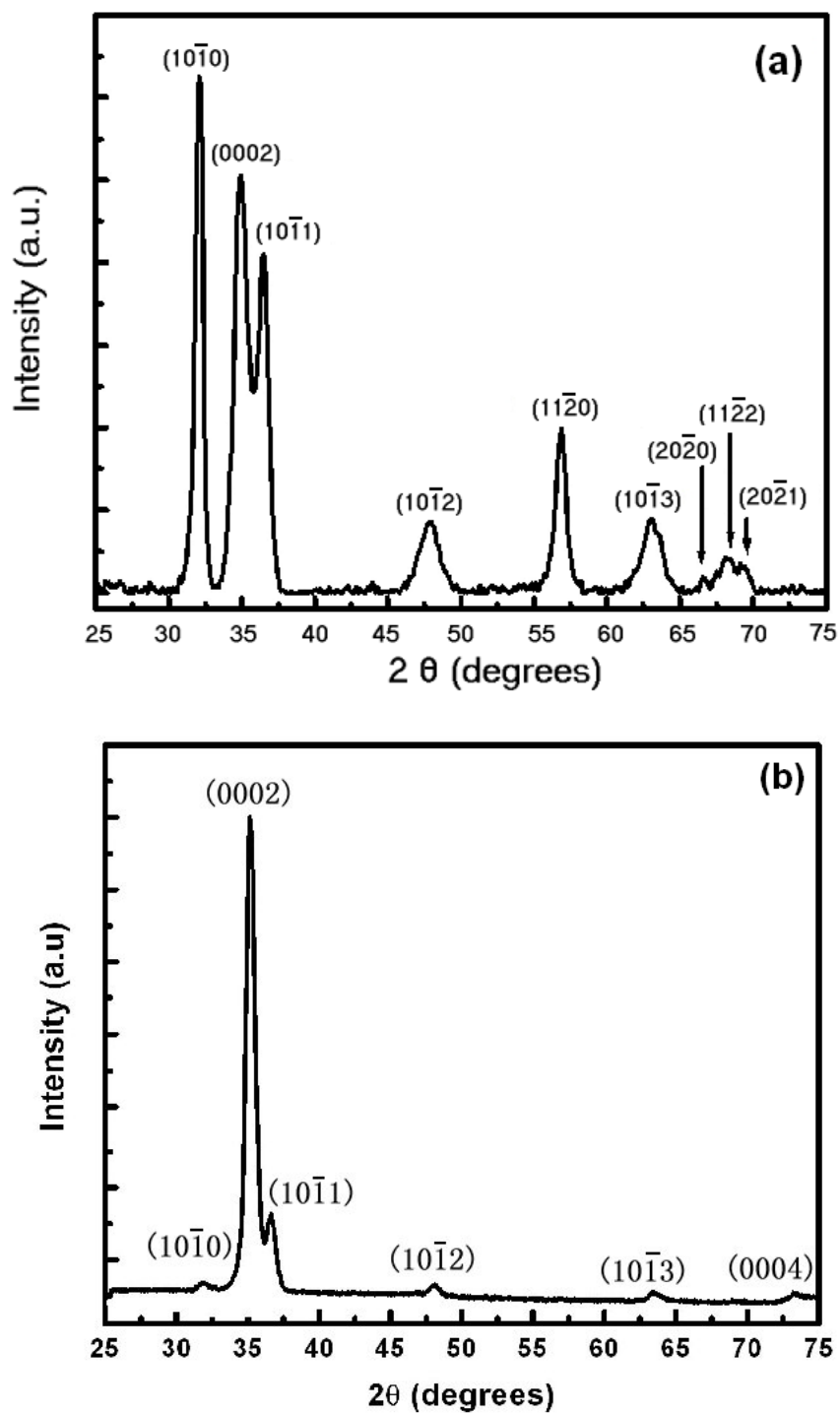


Figure 3.3. X-ray diffraction (XRD) spectra of Ga-doped ZnO films grown on glass at substrate temperature of (a) 380 °C; (b) 450 °C.

Figure 3.3 shows the X-ray diffraction spectra of GZO films grown at two different temperatures. At low growth temperature 380 °C, besides the peaks from ZnO (0002) and ZnO (0004), the peaks from other low-indexed ZnO crystalline planes, such as ZnO (10 $\bar{1}$ 0) , ZnO (10 $\bar{1}$ 1) , and ZnO (10 $\bar{1}$ 2) , are also present with strong intensity, indicating that the GZO film has a polycrystalline structure. As the temperature is increased to 450 °C, the dominant diffraction peak is from the ZnO (0002) crystalline plane, and the intensity of other low-indexed planes, such as ZnO (10 $\bar{1}$ 0) and ZnO (10 $\bar{1}$ 1) is significantly reduced, which indicates that the GZO films have a preferred c-axis orientation. The change from polycrystalline structure to c-axis textured film is consistent with SEM observations.

3.2 Electrical and Optical Properties

To characterize the electrical properties of GZO films, the sheet resistance of the GZO films is measured using Van der Pauw configuration. The GZO samples are cut into a square shape with an area of about 0.8 mm \times 0.8 mm. Four InSn alloy dots are placed at the four corners of GZO samples. Good InSn ohmic contact to GZO films is verified. During the measurement, a constant current is applied to a pair of adjacent corners and the voltage drop across the second pair of electrodes is measured. In order to determine the electron mobility coefficient mobility of GZO films, Hall measurement is carried out at room temperature. A magnetic field normal to the sample surface is applied to the GZO films. The voltage across a pair of diagonal corners is measured while a constant current is applied to the other diagonal pair. Maintaining the same configuration, the voltage is measured when the applied current is reversed and when the magnetic field is

reversed. The whole procedure is repeated for a second probe configuration. The electron mobility μ of GZO films is given by

$$\frac{1}{\mu} = \frac{1}{\mu_{ph}} + \frac{1}{\mu_{im}} + \frac{1}{\mu_b} \quad (3.2)$$

where, μ_{ph} ($\text{cm}^2/\text{V}\cdot\text{s}$), μ_{im} ($\text{cm}^2/\text{V}\cdot\text{s}$), μ_b ($\text{cm}^2/\text{V}\cdot\text{s}$) are the electron mobility components due to phonon scattering, impurity and defect scattering, and boundary scattering, respectively.

As the GZO film has carrier concentration as high as $10^{20}\sim 10^{21} \text{ cm}^{-3}$ and has polycrystalline or textured film structures, μ_{im} and μ_b are the dominant limiting factors of the electron mobility at room temperature. Figure 4.4 shows the temperature dependence of electron mobility and resistivity of light gallium doped ZnO films. At low growth temperature of 310 °C, the polycrystalline GZO film exhibits a Hall mobility of 2.05 $\text{cm}^2/\text{V}\cdot\text{s}$. The low electron mobility may be attributed to the small crystalline size and high defects concentration. As the growth temperature increases from 310 °C to 380 °C, the electron mobility monotonously increases. By increasing the growth temperature, the grain size of the GZO films increases and the crystalline quality is improved; therefore the scattering associated with the grain boundary and defects is reduced. The highest Hall mobility of 5.19 $\text{cm}^2/\text{V}\cdot\text{s}$ is obtained at the growth temperature of ~ 380 °C. At the growth temperature increases beyond 380 °C, the Hall mobility of the ZnO slightly decreases, even though the crystalline quality of GZO films is further improved. At high growth temperature, as-grown ZnO usually exhibits a textured structure, which is confirmed by FE-SEM images. Due to the highest growth rate along the ZnO (0001) direction, the GZO films have preferred c-axis orientation (Figure 4.2). The decrease in Hall mobility may attribute to the formation of columnar structure and suppress the

lateral current spreading. To decrease the sheet resistance of the GZO films, the formation of columnar structure should be avoided. However, another important parameter of TCO films is its light trapping capability. It is observed that textured ZnO films can be the efficient trapping structure for thin film solar cells; [101] In thin film solar cells, the incident light are scattered by the columnar structures in the textured ZnO TCO films, and pass through a longer optical path and increase the absorption by the absorber. Therefore, there exists a tradeoff between electron mobility and efficient light trapping capability of the GZO films. The optimal temperature window for GZO films is in the range of 370 °C ~ 400 °C.

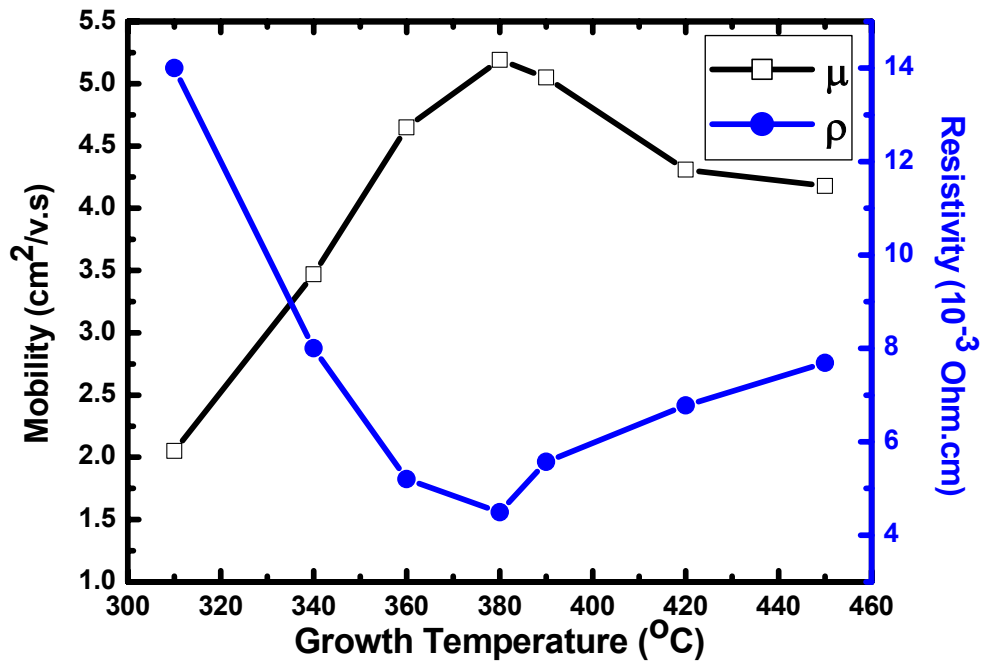


Figure 3.4. Temperature dependence of electron mobility μ and resistivity ρ of Ga-doped ZnO TCO films. The flow rates of DEZn and TEGa are kept at 100 sccm and 10 sccm, and the GZO films grown at different nominal temperature have the same nominal Ga

composition.

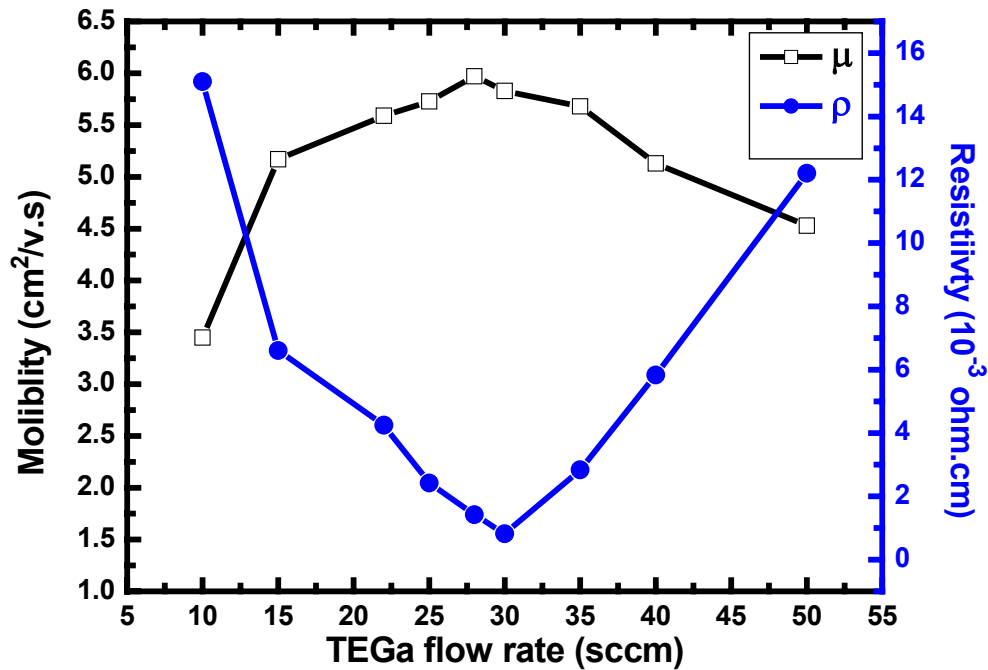


Figure 3.5. Electron mobility μ and resistivity ρ of Ga-doped ZnO films as a function of TEGa flow rate. The growth temperature of GZO films is kept at $\sim 400^\circ\text{C}$. The DEZn and oxygen flow rate are kept at 100 sccm and 1000 sccm, respectively.

The resistivity of GZO films is also related to the ion scattering. The ionized impurity scattering increase with gallium concentration until peak electron concentrations is reached. The electron concentration of the GZO film is a function of the gallium doping concentration. As a small amount of gallium is introduced into the film, the gallium atom is ionized into Ga^{3+} and replaces Zn^{2+} . One free electron is produced from one Ga^{3+} ion. The electron density therefore increases with the gallium concentration. At high gallium concentration, the free electron density begins to decrease because an increasing number

of dopant atoms form neutral defects instead of substituting the ZnO ions, and these neutralized gallium atoms do not contribute free electrons. The amount of electrically active gallium in the film is measured by the doping efficiency, which is defined as the ratio of number of free electrons in the film to the gallium concentration. There exists an optimal gallium concentration, which leads to the highest carrier concentration. [Figure 3.5](#) shows the electron mobility of GZO films as a function of TEGa precursor flow rate. It is interesting to find that at low TEGa flow, corresponding to low Ga doping level, the mobility of GZO films increases with the Ga doping level. The highest Hall mobility of the GZO films is $5.97 \text{ cm}^2/\text{V}\cdot\text{s}$ at carrier concentration of $1.05 \times 10^{21} \text{ cm}^{-3}$. The lightly doped GZO films have enhanced photoluminescence in comparison to undoped ZnO films. We assume that the lightly Ga-doped GZO films have better film quality with lower defects concentration. The detailed physical mechanism is not clear. As the TEGa flow is above 30 sccm, the mobility starts to decrease. The excessive Ga atoms do not incorporate into the ZnO lattice and do not contribute free electrons; instead, they may be located at the interstitials and even form ZnO, acting as defects, reducing the film quality. Room temperature PL spectra verify that the near band gap emission (NBE) of GZO films is significantly quenched at higher Ga doping level.

The stability of GZO films at various gas ambiances at high temperature is important in applications such as optoelectronic devices and solar cells processing. The GZO films with different Ga doping level in annealing in the air ambience at temperature from 300 °C to 600 °C for one hour. There is no significantly conductivity loss observed after the annealing.

The optical transmittance and sheet resistance are two important parameters for TCO films. In solar cells, the TCO films act as both the optical window and the collecting electrode, which determine the amount of light entering the absorbers and influence the extraction of photo-induced charges. Reduction of the resistivity requires an increase in the carrier concentration and the increase of carrier concentration reduce the transmittance. Versus is also true. High conductivity (or low sheet resistance) is balanced against high transmittance; therefore, a tradeoff between transmittance and sheet resistance has to be considered.

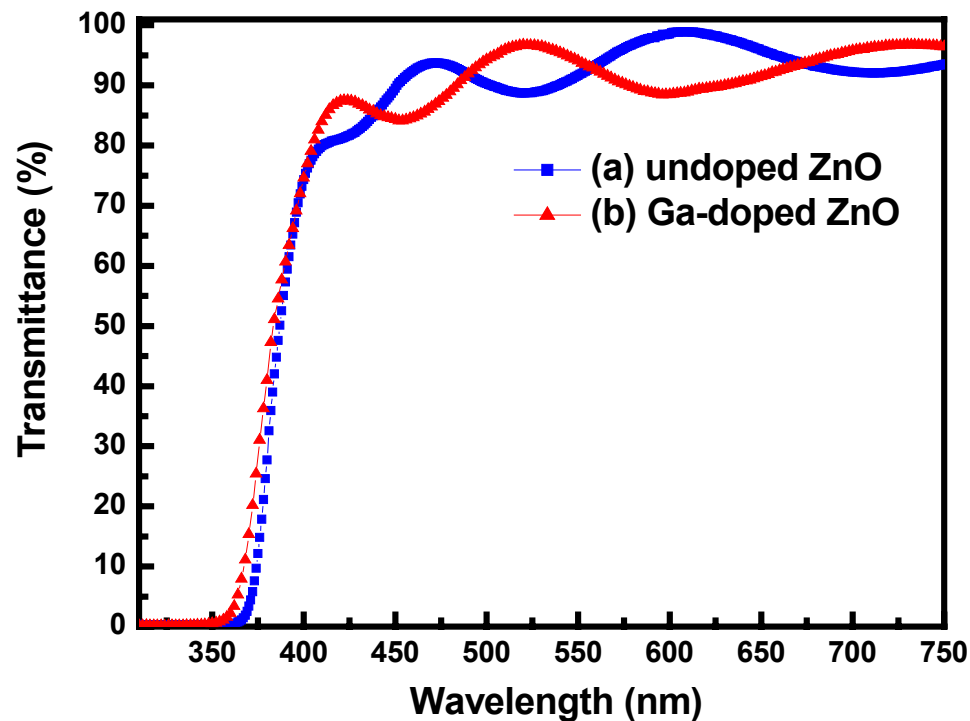


Figure 3.6. Transmission spectra of undoped ZnO and Ga-doped ZnO films grown at the similar conditions. The thickness of undoped ZnO and GZO films is ~ 400 nm and the GZO film has a sheet resistance of $\sim 25 \Omega/\text{sq}$.

Figure 3.6 shows the transmittance of undoped ZnO and GZO films. The undoped ZnO (400 nm) have a transmittance in visible wavelength over 89% as shown in curve a. In the UV region, the optical transmittance of ZnO film falls sharply due to the onset of the fundamental absorption in this region. The energy gap (E_g) can be estimated by assuming a direct transition between the valence and conduction band. For the undoped ZnO, the absorption edge is around 370 nm. For the GZO films (400 nm, sheet resistance of $\sim 25 \Omega/\text{sq}$) grown at optimized conditions, a transmittance above 85% in the visible wavelength is obtained. The absorption edge of the GZO films shifts to a shorter wavelength of ~ 359 nm. A blue shift of the absorption edge with increasing Ga doping level is observed, which is due to the Burstein–Moss effect associated with higher electron concentration in the conduction band of ZnO. [102]

3.3 Summary

We demonstrated MOCVD growth of Ga-doped ZnO TCO films on glass substrates using MOCVD. The growth parameters are optimized to balance the sheet resistance and transmittance in the visible wavelength. The morphology and crystallinity are characterized by scanning electron microscope and X-ray diffraction, respectively. At low growth temperature ($\sim 380^\circ\text{C}$), the GZO films have a polycrystalline structures. As the growth temperature increases above 400°C , the GZO films start forming columnar structures. It is found that the optimal growth temperature window is in the range of $380 \sim 400^\circ\text{C}$. The electrical properties of GZO films are characterized by Hall measurements. Under the optimal growth conditions, as grown GZO has Hall mobility of $5.97 \text{ cm}^2/\text{V} \cdot \text{s}$.

Under the optimal growth conditions, GZO films with a thickness of 400 nm have sheet resistance of $\sim 25 \text{ } \Omega/\text{sq}$ and transmittance over 85% in the visible wavelength. The transmittance of GZO films is measured using transmission spectroscopy. A blue shift of Ga-doped ZnO is observed due to Burstein–Moss effect associated with high carrier concentration. As the GZO film exhibits high conductivity and high transparency in the visible wavelength, it has potential applications, such as transparent electrode for liquid crystal display (LCD), solar cells, light emitting diodes (LEDs), efficiency energy windows, etc.

Chapter 4 Growth and Characterization of ZnO Nanotips

In chapter 3, we demonstrate the growth of Ga-doped ZnO (GZO) transparent conducting oxide (TCO) films using MOCVD. Sheet resistance of $\sim 25 \text{ } \Omega/\text{sq}$ and transmittance over 85% in the visible wavelength is achieved in MOCVD-grown GZO films with a thickness of 400 nm. Recently, low dimensional ZnO nanostructures have attracted increasing attention due to their unique physical, chemical, electrical and optical properties. These ZnO nanostructures have potential applications, such as gas sensors, biosensors, polymer-based and dye sensitized solar cells. In this category of devices, larger surface area is required to provide anchoring sites for gas molecules, DNA, dye and other chemicals. Nanostructured morphology of ZnO is critical factor to achieve efficient sensing or light harvesting. Various growth technologies, such as thermal evaporation, CVD, PLD and chemical solution synthesis, have been developed for ZnO nanostructure growth. Among these growth technologies, MOCVD offers advantages, such as catalyst-free growth, low crystallization temperature, better control over growth rate, controllable *in-situ* doping, and capability of large-scale mass production. In this chapter, we investigate the growth of ZnO nanotips using MOCVD. The growth parameters, such as chamber pressure, substrate temperature, gas flow rate, and precursor ratios, are optimized. The morphology, crystallinity and optical properties are comprehensively characterized. The growth mechanism of forming well-aligned ZnO nanotips on various substrates, such as GaN, silicon and glass, is studied.

4.1 Growth of ZnO Nanotips on Various Substrates

The formation of ZnO nanostructures during MOCVD growth is very complicated, not only depending on specific chamber design and flow pattern, but also depending on growth parameters, such as chamber pressure, growth temperature, precursor flow rate and ratio. [Figure 4.1](#) shows the morphologies of ZnO nanostructures grown at un-optimized growth conditions. The ZnO nanotips don't have a uniform size, and sharp tip ends, and are in irregular shapes. In order to obtain ZnO nanotips with high crystalline and optical quality, high aspect ratio and good morphology, it is necessary to optimize the growth parameters.

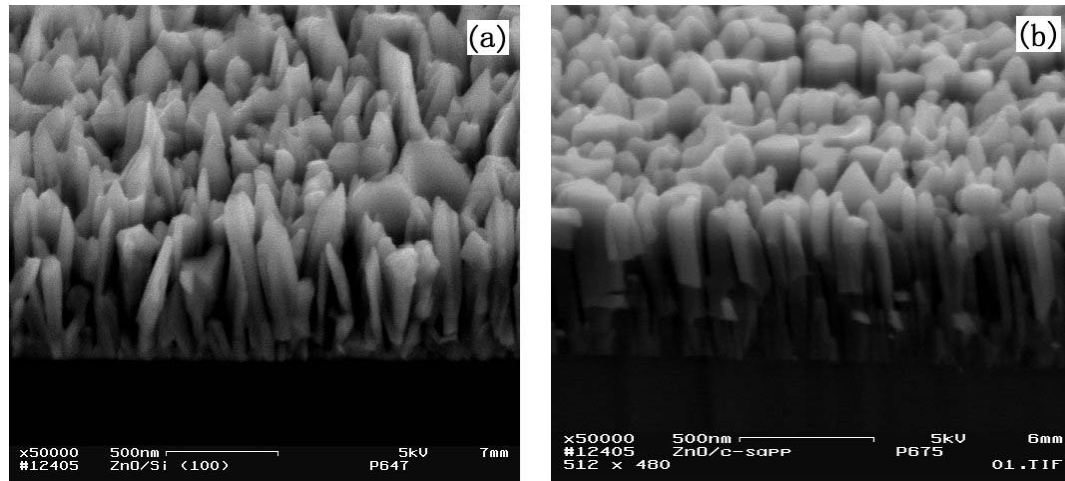


[Figure 4.1](#). Field emission scanning electron microscope (FE-SEM) images of ZnO nanotips grown under un-optimized conditions, (a) on p-Si substrate, (b) on c-Al₂O₃ substrate.

Due to the large Gibbs free energy changes during the MOCVD growth of ZnO, the phase reactions in the chamber may result in particles in the chamber, and these particles accumulate at the growth surface and determinate the sample quality. Chamber pressure decides the average free path of the reactive species. At the exit of the gas injector, the transit time from the injector to the substrates is a critical parameter. At high chamber pressure (above 200 torr), the DEZn molecules have a shorter free path, resulting in a higher probability to interact with the oxygen molecules before reaching the substrate. Meanwhile, at the higher chamber pressure, the reactive species will impinge on the substrate with high downward speed and bounce back to create turbulence, which also increases the interaction of the reaction species. Particles from the phase reaction fall down to growth surface and initiate the random growth ZnO nanostructures on the particles. The typical particles initiated ZnO growth is shown in [Figure 4.2](#).

At lower chamber pressure, the transition time is significantly reduced, resulting in minimized phase reaction before the reactive species reaching the substrates. However, the reactive species will be quickly pumped away before reaching the growth surface, resulting lower growth rate and poor uniformity. It is found that the growth rate of the ZnO nanotips drops to 100 nm/hr when the chamber pressure reduces to below 20 torr. The optimal chamber pressure is found to be ~ 50 torr, at which the phase reactions is significantly suppressed, and the reactive species form a laminar flow above the growth surface, leading to sufficient relaxation time at the growth planes.

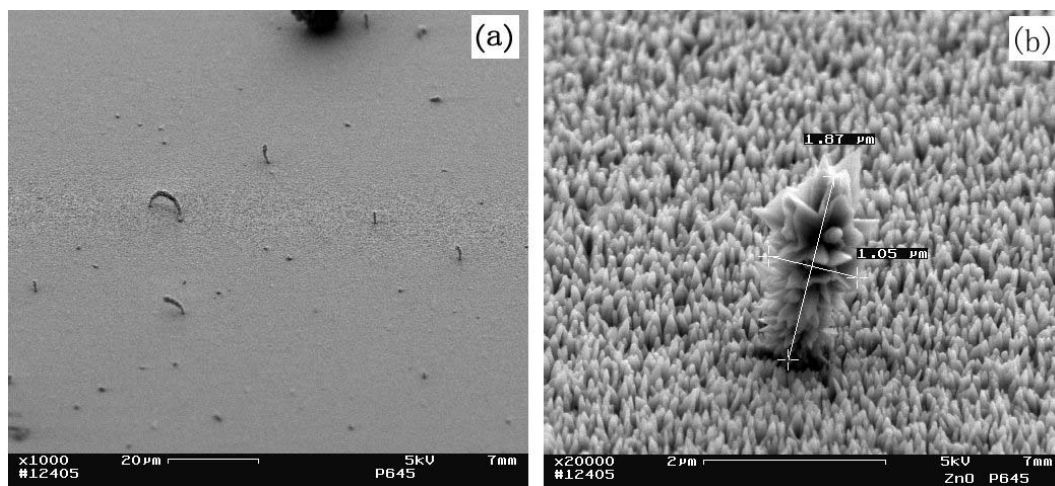


Figure 4.2. Field emission scanning electron (FE-SEM) images, showing morphologies of ZnO nanotips under unoptimized growth conditions. Phase reaction results in nanoparticle and the ZnO nanoparticles initiate random nanotip growth on the surface of ZnO nanotips.

The substrate temperature is an important parameter that affects the morphologies and crystalline quality of the ZnO nanotips. The morphologies of the ZnO nanotips grown at different temperatures are shown in Figure 4.3. At growth temperature of 350°C, the ZnO nanotips are dense with round top ends as shown in Figure 4.3(a), with an average diameter of 70 nm. As the growth temperature increases from 350°C to 480°C, the ZnO nanotips are relatively separate, and the top end of the nanotips become sharper, as shown in Figure 4.3(b)-(c). As the temperature further increases to 550°C, the morphology of ZnO changes from nanotips to nanorods with a flat top end, as shown in Figure 5.3(d). The ZnO nanorods are randomly orientated and pointing away from the substrate surface normal. The growth rate of ZnO nanotips at 350°C is about 0.6 μm/hr. As growth temperature increases to 420°C, the growth rate increases to about 1.0 μm/hr. As the

growth temperature increases further, there is no significant increase in the growth rate. The aspect ratio of the ZnO nanotips grown at 350°C is ~ 4 , while at temperature 420°C and 480°C, the aspect ratio is observed to be ~ 10 . At high growth temperature of 550°C, the aspect ratio drops due to the increase in the diameter of the ZnO nanorods.

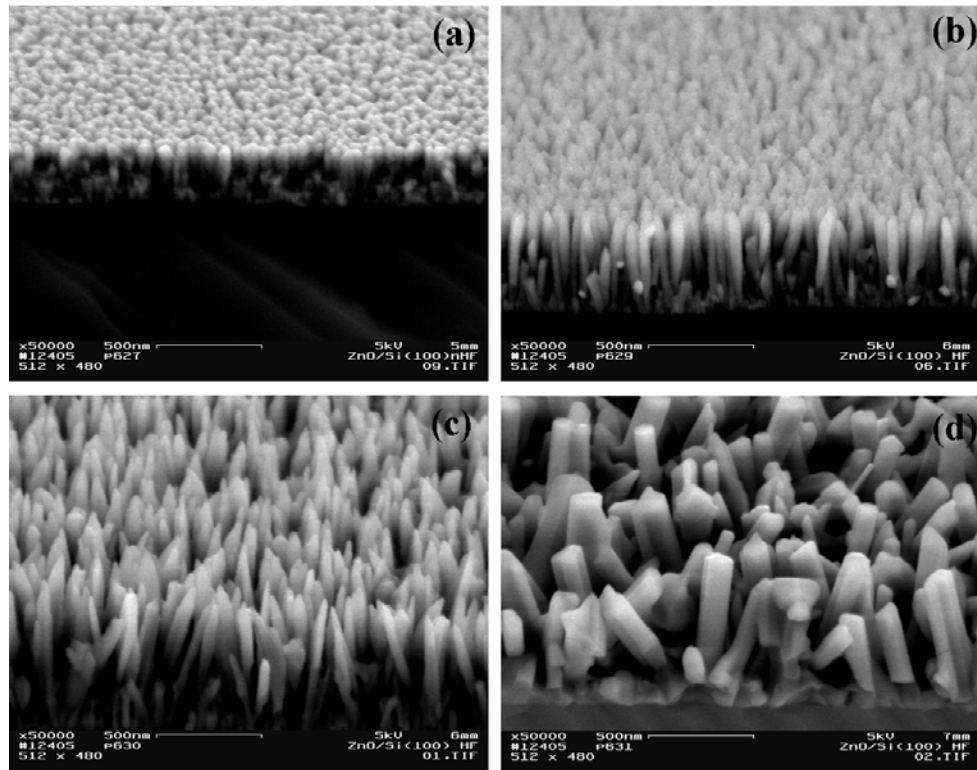


Figure 4.3. Field emission scanning electron microscope (FE-SEM) images of ZnO nanotips grown on Si substrate at growth temperatures: (a) 350°C, (b) 420°C, (c) 480°C, and (d) 550°C.

Figure 4.4 shows the XRD spectra of ZnO nanotips grown on silicon (100) at growth temperatures ranging from 350°C to 550°C, while keeping similar flow conditions and growth time. At the growth temperature of 350°C, 420°C and 480°C, only ZnO (0002)

and (0004) diffraction peaks are observed, as shown in curve a-c, indicating that ZnO nanotips are grown along c-axis orientation of the ZnO nanotips. As the growth temperature increases to 550°C, additional peaks corresponding to ZnO ($10\bar{1}0$), ZnO ($10\bar{1}1$), and ZnO ($10\bar{1}2$) are also observed, as shown in curve d, indicating that these ZnO nanotips are not aligned along the c-axis direction, which is consistent with FE-SEM images. Transmission electron microscope (TEM) characterization reveals that a ZnO nanotip has single crystalline quality with very low defects concentration. [103]

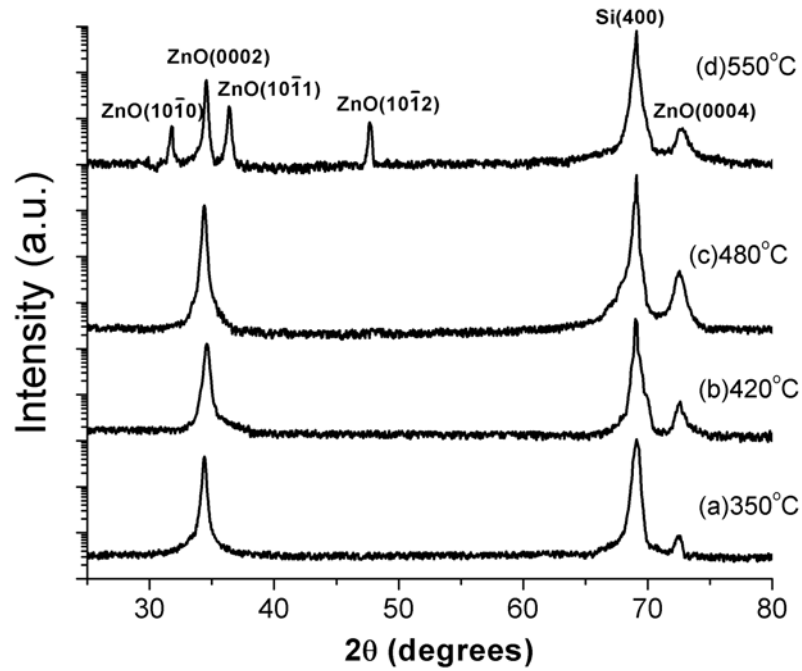


Figure 4.4. X-ray diffraction (XRD) of ZnO nanotips grown on Si (100) substrates at growth temperatures: (a) 350 °C, (b) 420 °C, (c) 480 °C, and (d) 550 °C.

Figure 4.5 shows the room temperature PL spectra of ZnO nanotips grown at different substrate temperatures. The dominant peak at 376 nm (3.30 eV) is the near-band-edge

(NBE) emission of ZnO nanotips. At low growth temperature of 350 °C, the peak

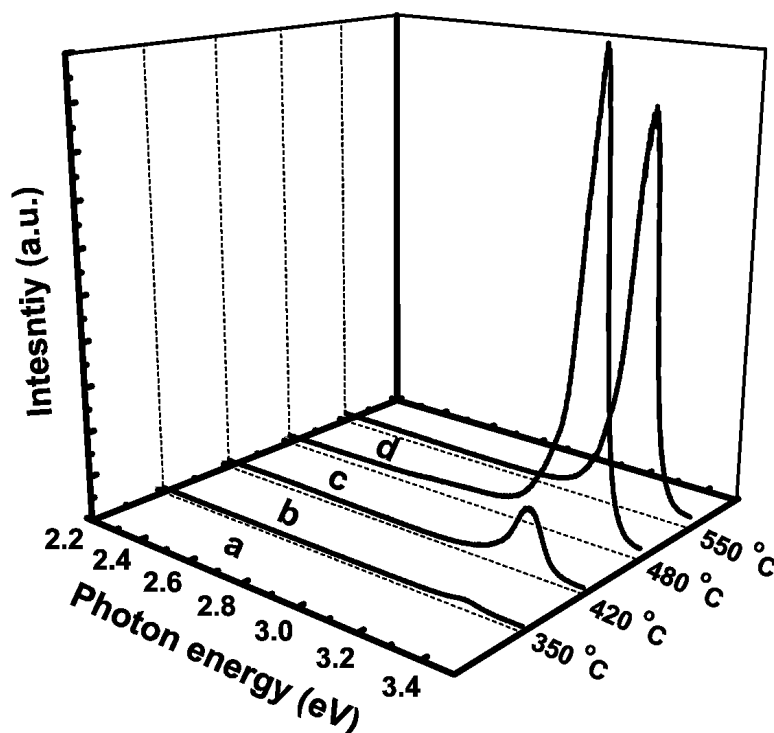


Figure 4.5. Room temperature photoluminescence (PL) spectra of ZnO nanotips grown at substrate temperatures: (a) 350°C, (b) 420°C, (c) 480°C, and (d) 550°C.

intensity of NBE emission is relatively weak, as shown in curve (a). A high concentration of nonradiative recombination centers are formed, though XRD indicated that ZnO nanotips maintain the good crystalline quality and have preferred c-axis orientation at low temperature. The intensity of NBE emission monotonically increases as the growth temperature increases from 350 to 500 °C, as shown in curve (b)-(c). The stronger peak intensity in PL indicates good optical properties of the ZnO nanotips, which may be attributed to the reduced concentration of defects and improved crystallinity. As the substrate temperature increases further to beyond 500°C, the intensity of the NBE

emission drops, possibly due to enhanced bulk diffusion process and defect generation and migration. In addition to the NBE emission, no visible green band emission (~ 2.45 eV), which is reported to be associated with singly ionized oxygen vacancies, [104] is observed in the PL spectra for the temperature range of $350 \sim 550$ °C.

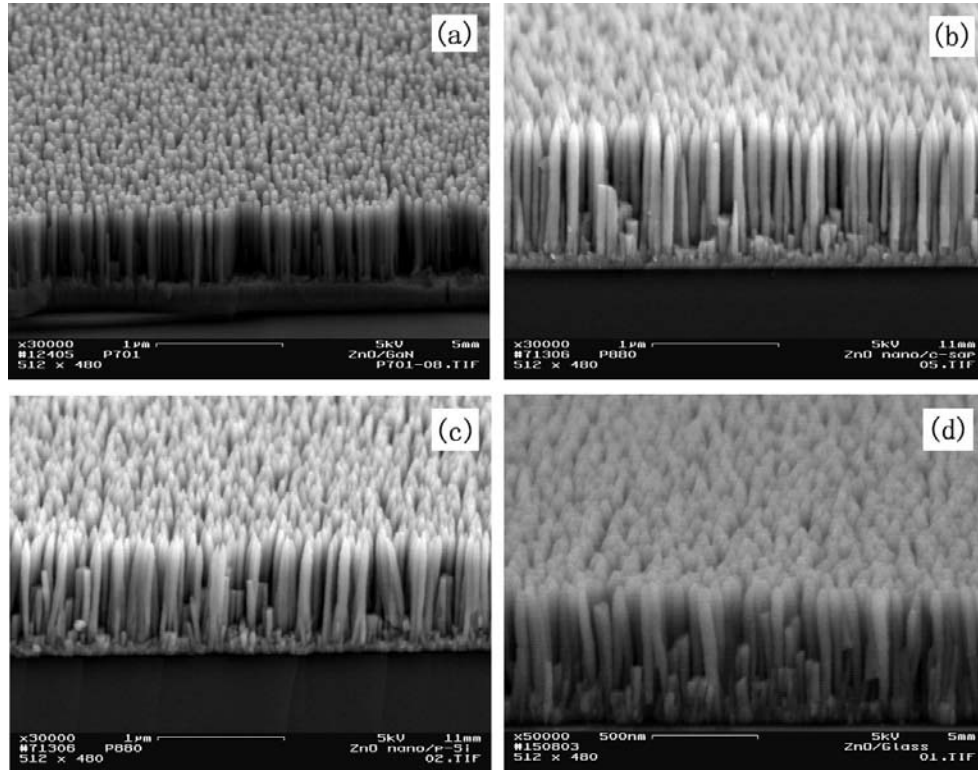


Figure 4.6. Field emission scanning electron microscope (FE-SEM) images of ZnO nanotips grown on various substrates, (a) GaN/c-Al₂O₃, (b) c-Al₂O₃, (c) Si (100), and (d) glass.

ZnO nanotips can be grown on various substrates, including c-Al₂O₃, GaN, Si and glass substrates as shown in Figure 5.7. The growth of ZnO nanostructures on c-Al₂O₃ and GaN substrates is found to have epitaxial relations with the substrates. [105] GaN has the same wurzite crystal structure as the ZnO and closer lattice parameters. ZnO nanotips

grown GaN epilayers follows the epitaxial relations: $\text{ZnO} (0001) // \text{GaN} (0001)$ and $\text{ZnO} [\bar{1}\bar{1}00] // \text{GaN} [\bar{1}\bar{1}00]$. ZnO grown on c- Al_2O_3 follows the epitaxial relations: $\text{ZnO} (0001) // \text{Al}_2\text{O}_3 (0001)$ and $\text{ZnO} [\bar{1}\bar{1}00] // \text{Al}_2\text{O}_3 [2\bar{1}\bar{1}0]$. This epitaxial relationship corresponds to a 90 °C or 30 °C in plane rotation in respect to the basal plane of Al_2O_3 (0001) substrate. The lattice mismatch between ZnO and c- Al_2O_3 is as large as 15%, and the lattice mismatch between ZnO and GaN is less than 2%. Due to the less lattice mismatch between ZnO and GaN, ZnO nanotips grown on GaN are much better aligned along the substrate surface normal than on c- Al_2O_3 . The ϕ scan shows that the full width of maximum (FWHM) is much smaller than those grown on c- Al_2O_3 substrates. Using microscopic study of the initial growth of ZnO on GaN, it was found that the ZnO on GaN templates nucleates and grows via the Stranski-Krastanov mode. [106] An interesting phenomenon is that well-aligned ZnO nanotips can also be grown on lattice-mismatched Si substrate, and even amorphous surfaces like SiO_2 , TiO_2 , glass substrates. Since there is no epitaxial relationship with the substrate, the growth mechanism of ZnO grown on these substrates is different from epitaxial growth.

Our group has reported that a-plane $\text{ZnO} (10\bar{1}2)$ epitaxial film can be grown on r-plane $\text{Al}_2\text{O}_3 (01\bar{1}2)$ substrate. The ZnO films on r- Al_2O_3 substrates follow epitaxial relationship $\text{ZnO} (11\bar{2}0) // \text{Al}_2\text{O}_3 (01\bar{1}2)$ and $\text{ZnO} [0001] // \text{Al}_2\text{O}_3 [01\bar{1}1]$. [107] It is interesting to find that ZnO epitaxial films and ZnO nanotips can be integrated on a single substrate using patterned growth. In order to achieve the selective growth, a thin layer of metal or dielectric is patterned on the r-plane Al_2O_3 , which acts as the seed layer for ZnO nanotips. Figure 4.7 shows the selective growth on ZnO nanotips and ZnO epitaxial films on a Ti-

patterned r-plane Al_2O_3 ($01\bar{1}2$) substrate. The Ti layer is patterned on the r-plane Al_2O_3 ($01\bar{1}2$) by a liftoff process. It is found that the ZnO nanotips are grown on the Ti layers and vertically aligned along substrate surface normal. The ZnO epitaxial films are only grown on r-plane Al_2O_3 ($01\bar{1}2$). Due to the highest growth rate of ZnO along the c-axis direction, the thickness of the ZnO nanotips is higher than that of the ZnO epitaxial film. Figure 4.8 shows the corresponding X-ray diffraction spectrum. Both c-axis (0001) and a-axis ($11\bar{2}0$) ZnO peaks are present, indicating the presence of ($11\bar{2}0$) ZnO film on ($01\bar{1}2$) r-plane sapphire and (0002) ZnO nanotips on the patterned Ti templates. Other peaks present in Figure 4.8 are from the TiO_2 , Ti, and sapphire substrate. Ti thin film is oxidized in the oxygen ambience during the ZnO growth to form rutile (TiO_2). [108] The two peaks of rutile TiO_2 in the X-ray spectrum are TiO_2 (110) and TiO_2 (210), respectively.

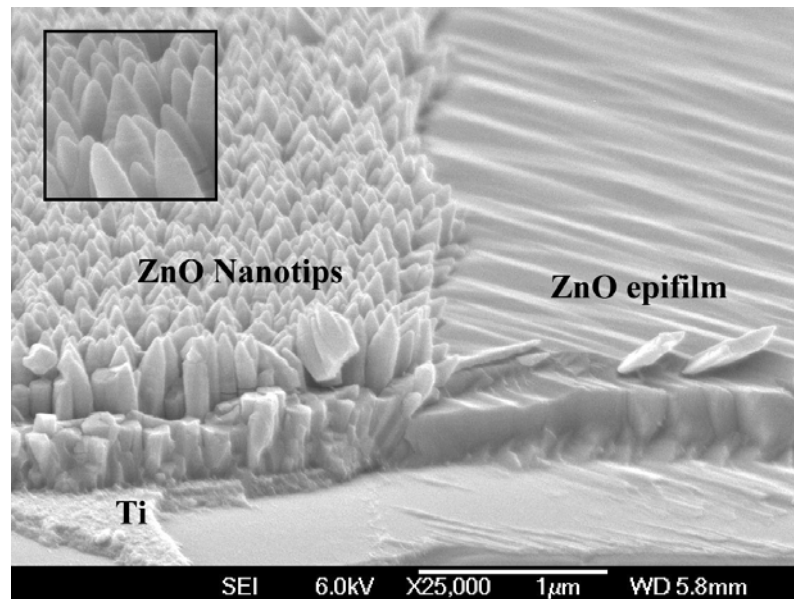


Figure 4.7. A field emission scanning electron microscope (FE-SEM) image of ZnO nanotips and ZnO epitaxial films selectively grown on Ti-patterned r- Al_2O_3 substrate.

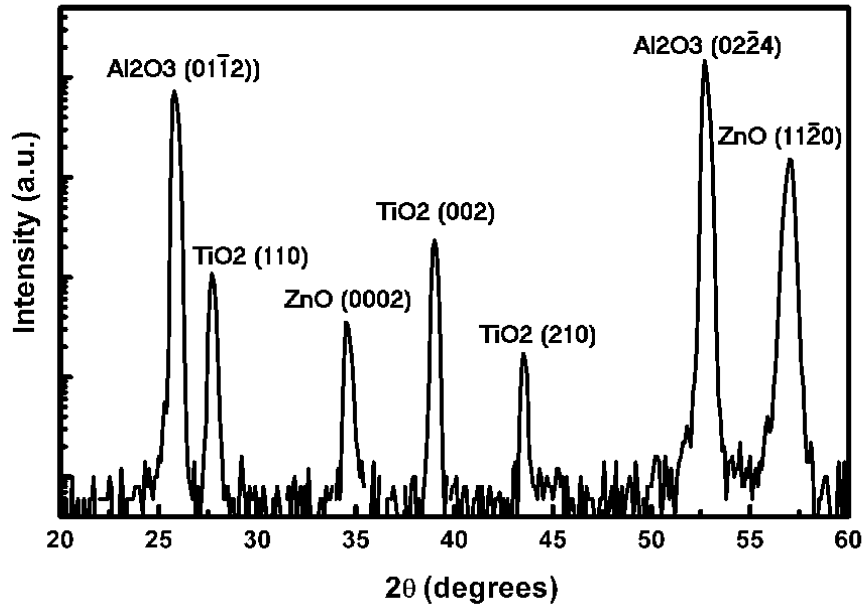


Figure 4.8. X-ray diffraction spectrum of ZnO nanotips and ZnO epitaxial film selectively grown on Ti patterned r-Al₂O₃ substrate.

To further characterize the optical properties of ZnO nanotips. Low temperature micro-cathodoluminescence (MCL) spectra are measured using a JEOL microscopic system. With constant incident beam power of 2.0 μ W, the kinetic energy of the incident electron beam is varied from 1.0 KeV to 20 KeV. The ZnO nanotips have an average length of 500 nm, and the typical diameters at the top and bottom are about 5nm and 60nm, respectively. At beam energy of 1.0 KeV, the maximum excitation depth (D_B) is about 20 nm with a beam diameter (Φ_B) of 10 nm, which is less than the diameter of ZnO nanotip. Hence the electron beam can focus on a single ZnO nanotip and the MCL emission is mainly from the top end of the ZnO nanotips. Sharp excitonic peak is observed at 3.373 eV, which may attribute to the free exciton emission. The energy difference between first

and second peak is about 61 meV. Similar results have been observed in the low temperature PL spectra of ZnO nanotips via VLS mechanism, and the second peak is attributed to the free-to-bound transitions (FB). The energy shift from the second peak to the third peak is ~ 72 meV, and it corresponds to 588 cm^{-1} phonon replica $\nu_{\text{ILO}}(\text{E1})$ of ZnO. As the beam energy increases to 5.0 KeV, the beam penetrates deeper into the ZnO nanotips with a Φ_{B} of 50 nm, the second phonon replica is weakly visible due the increased MCL emission intensity. No green band emission is observed at the beam energy of 1.0 KeV and 5.0 KeV. As the beam energy increases, the beam penetrates further deep into the ZnO nanotip array. At the beam energy of 20 KeV, Φ_{B} increases to 330 nm, and D_{B} is estimated to be about $1.0\text{ }\mu\text{m}$, which is larger than the length of the ZnO nanotips. As a result, the emission from the base of ZnO nanotips can be collected. A broad green band emission centered at 2.5 eV is observed, which may originate from the bottom of the ZnO nanotips. The ZnO and Si substrate has large lattice mismatch between ZnO and Si substrates, significant stress may be induced in the bottom of the ZnO nanotips and defects may also be generated in the initial ZnO layer, which results in the green band emission. No green band emission is observed at low excitation depth, indicating that the crystalline quality of ZnO nanotips varies along the length of the ZnO nanotips, improving towards the end of the ZnO nanotips.

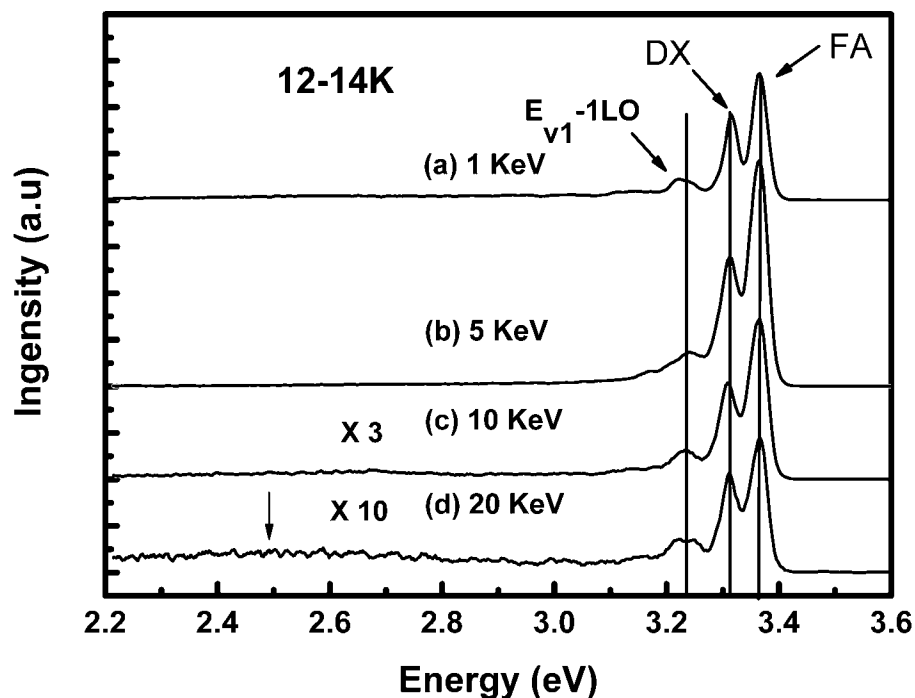


Figure 4.9. Low temperature (12-14 K) micro-cathodoluminescence (MCL) spectra of undoped ZnO nanotips grown on p-Si substrates. The power of the incident electron beam is kept at constant of 2.0 μ W. Curve a-d corresponding to the electron beam energy of 1.0 KeV, 5.0 KeV, 10 KeV and 20 KeV, respectively.

4.2 Growth of ZnO Nanotips on GZO Films

We demonstrated the growth of GZO transparent conducting film and ZnO nanotips using MOCVD. If ZnO nanotips can be grown on GZO films, the combination of ZnO nanotips and GZO films would provide a promising photoelectrode for applications such as dye sensitized solar cells, polymer-based solar cells and transparent electrode for light emitting devices. The n-type semiconductor ZnO nanotips provide large surface area for

dye anchoring in conjunction with direct conduction pathways for charge transport, while the GZO film acts as the transparent electrode.

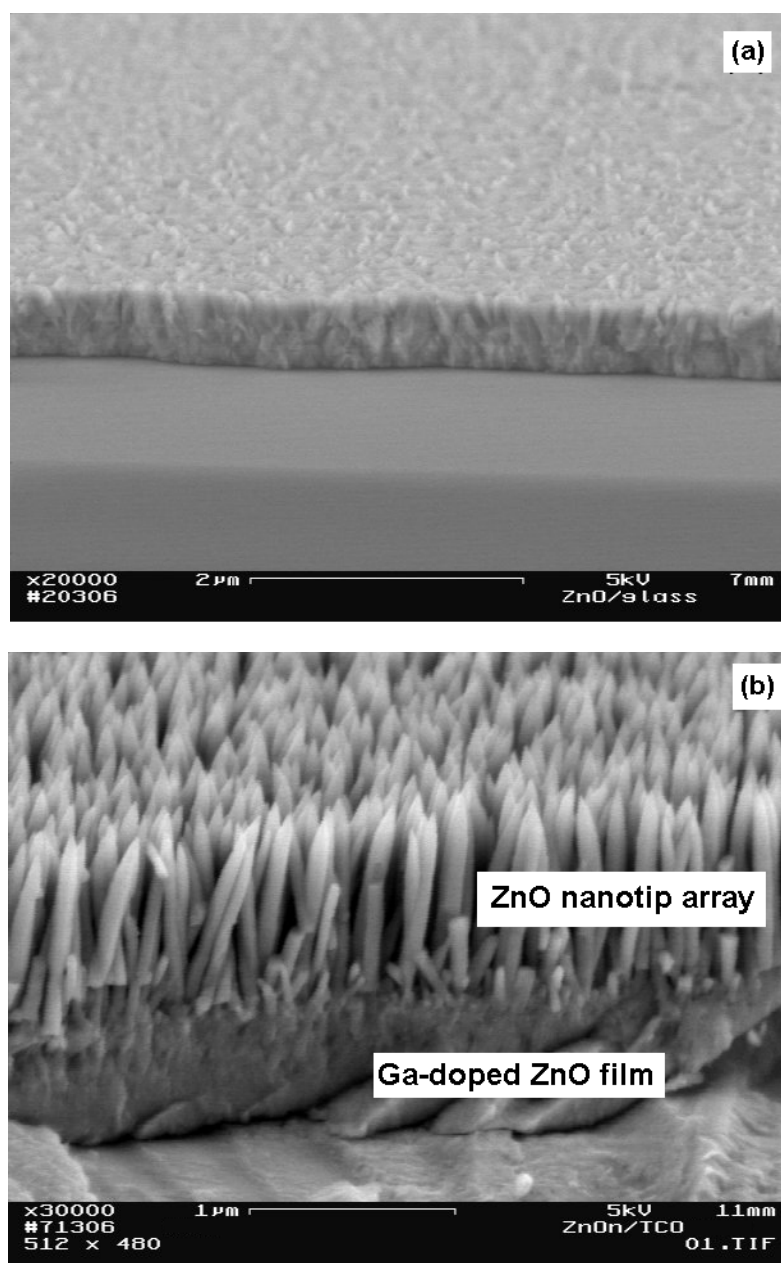


Figure 4.10. A field emission scanning electron microscope (FE-SEM) images of (a) Ga-doped ZnO TCO films; (b) Sequentially grown ZnO nanotips/Ga-doped ZnO film. The Ga-doped ZnO film is grown at low temperature of ~ 400 °C and the undoped ZnO nanotip array is grown at temperature of ~ 470 °C.

Shown in Figure 4.10(a) is the GZO film growth at low temperature of ~ 400 °C. The GZO film exhibits a dense film structure with smooth surface. To grow ZnO nanotips on GZO films, the growth temperature is increased to above ~ 470 °C. Figure 4.10(b) shows a SEM image of ZnO nanotips/GZO structure sequentially grown on the glass substrate. The ZnO nanotips are vertically aligned along the substrate normal direction. Figure 4.11 shows the XRD spectrum of the ZnO nanotips grown on accompanying glass substrate. Only peaks from ZnO (0002) and ZnO (0004) are observed, indicating that ZnO nanotips are c-axis preferably oriented. We speculate that the ZnO nanotips grown on the GZO films also have c-axis preferred orientation.

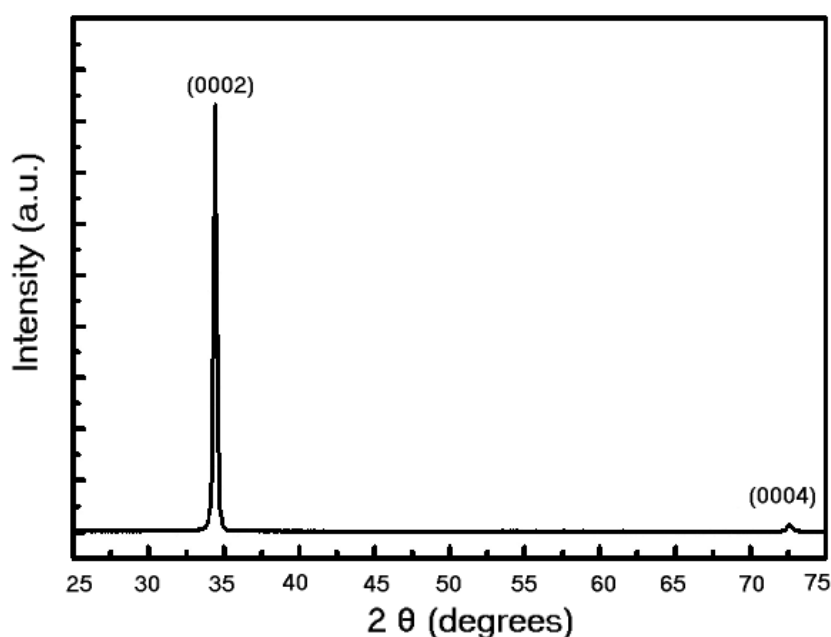
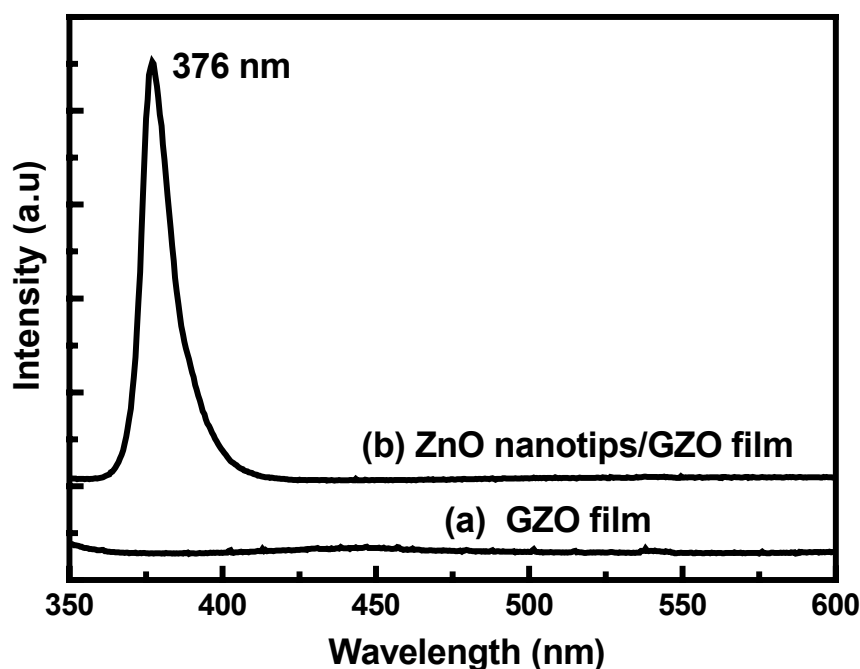


Figure 4.11. X-ray diffraction (XRD) spectrum of ZnO nanotips grown on glass substrate, which is grown under the same growth conditions of the ZnO nanotips grown on Ga-doped ZnO film.

Shown in [Figure 4.12](#) are the room temperature PL spectra of ZnO nanotips/GZO film structure. The near band edge (NBE) emission of GZO films is significantly quenched due to the heavy Ga doping (curve a). The peak at ~ 376 nm (3.30 eV) from the ZnO nanotips/GZO film structure is predominantly from the free exciton emissions of ZnO nanotips (curve b). Due to the larger exciton binding energy of 60 meV, free excitons in high quality MOCVD-grown ZnO nanotips or nanorods can survive up to room temperature. The strong peak intensity in PL indicates good optical property of ZnO nanotips.



[Figure 4.12](#). Room temperature photoluminescence (PL) spectra; (a) GZO film, (b) ZnO nanotips grown on the GZO film.

4.3 Growth Mechanism of ZnO Nanotips

The observation of thin film formation has revealed three basic growth modes: (1) island growth (or Volmer-Weber), (2) layer growth (or Frank-van der Merwe), and (3) combination of island and layer growth (Stranski-Krastanov). The island growth occurs, when the smallest stable clusters nucleate on the substrate and expand in three dimensions to form islands. This happens when the reacting species in the deposition are more strongly bounded to each other than to the substrate. In the layer growth, on the opposite, the extension of the smallest stable nucleus occurs overwhelmingly in two dimensions in the growth surface, resulting in the formation of planar sheets. In this mode, the reactive species are more strongly bounded to the substrate than to each other. The first complete monolayer is then covered with somewhat less tightly bound second layer. Providing the decrease in bounding energy is continuous towards bulk crystal value, the layer growth mode is sustained. The layer plus island growth mechanism is an intermediate combination of the aforementioned. In this case, after forming several monolayers, subsequent layer growth becomes unfavorable and islands form. Any factors that disturb the monotonic decrease in binding energy characteristic of layer growth may be the cause. The substrate, the film materials, and interfacial surface energies determine the prevailing, thermodynamically controlled growth mode.

The growth of the ZnO nanotips involves two stages: the nucleation and subsequent growth. Understanding of the growth mechanism of ZnO nanostructures is important not only for materials science and also for device applications. The growth of CVD films can be understood provided that the Gibbs free energy change ΔG can be approximated by the standard free-energy change ΔG° . In order to grow single crystal films, it is essential

that a single nucleus form as an oriented seed for the subsequent growth. According to the nucleation theory, a small negative value of ΔG , the chemical Gibbs free energy per unit volume is required to foster a low nucleation rate of large critical-sized nuclei. The nucleation rate is a term that describes how many nuclei of critical size form on a substrate per unit time. Nuclei can grow through direct impingement of gas phase atoms, but it is unlikely in the initial stage of ZnO nanotip growth. The nucleation rate at which critical nuclei grown depends on the rate, at which adsorbed monomers (adatoms) attach to it. Energetic vapor atoms that impinge on the substrate and remain on the surface for a length of time τ_s given by

$$\tau_s = \frac{1}{\nu} \exp\left(\frac{E_{des}}{KT}\right) \quad (4.1)$$

where ν is the vibrational frequency of the adatom on growth surface, and E_{des} is the energy required to be desorbed it back to the vapor, K is the Boltzmann constant and T is absolute temperature.

The adatoms, which have not yet thermally accommodated to the substrate, experience random diffusion and may attach to larger atomic clusters or nuclei. When this happens, it is unlikely that these atoms will return to the vapor phase. Changes in E_{des} are particularly expected at substrate heterogeneties. The large atom bonds available at these accommodating sites lead to higher E_{des} value. For this reason, a significantly higher density of nuclei is usually observed near cleavage steps and other substrate imperfection. The presence of impurities similarly alters the E_{des} and the nucleation rates.

The growth rates of ZnO crystal in different low index crystalline directions follow the order: $[0001] > [10\bar{1}0] > [10\bar{1}1] > [000\bar{1}]$. The as-grown ZnO usually exhibits a columnar

structure due to the fastest growth rate along the ZnO [0001] direction. This inherent property of ZnO crystal is the main driving force for the formation of one-dimensional ZnO nanostructures. By properly controlling the growth conditions, ZnO nanowires with aspect ratio of more than 20 can be achieved.

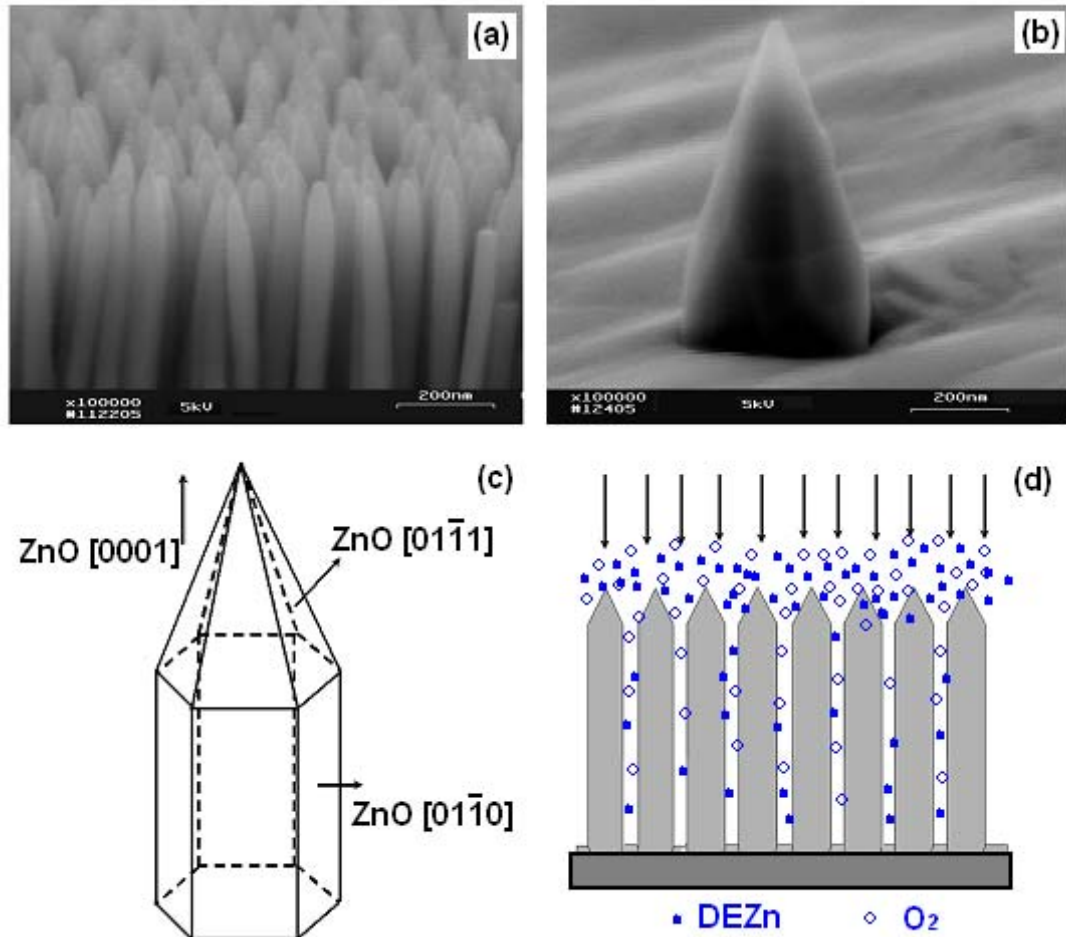


Figure 4.13. (a) Field emission scanning electron microscope (FE-SEM) image of a ZnO nanotip array, (b) A FE-SEM image of a single ZnO nanotip grown out of a-plane ZnO epitaxial film, (c) a schematic of typical morphology of ZnO crystal, and (d) a schematic showing the growth habitat of ZnO nanotips.

However, the growth rate difference between the ZnO low-index crystalline planes is not the only reason for forming ZnO nanotip array with high aspect ratio, the specific growth environment during the MOCVD growth also plays a significantly role. In order to clarify it, an array of ZnO nanotips and an isolated single ZnO nanotip are grown under the same growth conditions. [Figure 4.13\(a\)](#) shows a FE-SEM image of a well-aligned ZnO nanotips array. The nanotips are aligned along the substrate surface normal. The ZnO nanotips in the array have a length of 1.0 μm with an average diameter of ~ 50 nm, resulting in an aspect ratio of ~ 20 . In order to initiate the growth of an isolated ZnO nanotip, a nanoparticle seed is first placed on the r-plane Al_2O_3 surface, which acts as the seed for the ZnO nanotip. ZnO grown on r-plane Al_2O_3 substrate follows the epitaxial relationship: $\text{ZnO } (1\bar{1}\bar{2}0) // \text{Al}_2\text{O}_3 (01\bar{1}2)$ and $\text{ZnO } [0001] // \text{Al}_2\text{O}_3 [10\bar{1}1]$, which implies that the c-axis of the ZnO epifilm is lying inside the growth plane. [\[109\]](#) An isolated ZnO nanotip is grown on the oxide nanoparticle with the c-axis direction parallel to the substrate surface normal. Due the different growth rate of the ZnO nanotips and the ZnO $(1\bar{1}\bar{2}0)$ epitaxial film, the ZnO nanotip outgrows the ZnO $(1\bar{1}\bar{2}0)$ film as shown in [Figure 4.13\(b\)](#). The diameter of the isolated single ZnO nanotip at the base is measured to be 380 nm and the length from the base to tip is around $\sim 1.0 \mu\text{m}$, resulting in an aspect ratio of 2.6. The higher aspect ratio of the ZnO nanotips in the array in comparison to the isolated ZnO nanotip is resulted from the different growth environment. [Figure 4.13\(c\)](#) illustrates the typical morphology of as-grown ZnO crystal. It usually exhibits a pyramid-shaped crystallite faceted with $\{10\bar{1}0\}$ and $\{10\bar{1}1\}$ planes. In both cases, due to the sustaining supply of the reacting species at the tip end of ZnO nanotips, the ZnO nanotips quickly elongate along the c-axis direction as shown in [Figure 4.13\(d\)](#). It is observed that

both the ZnO nanotip in the array and an isolated ZnO have the same length from the base to the top.

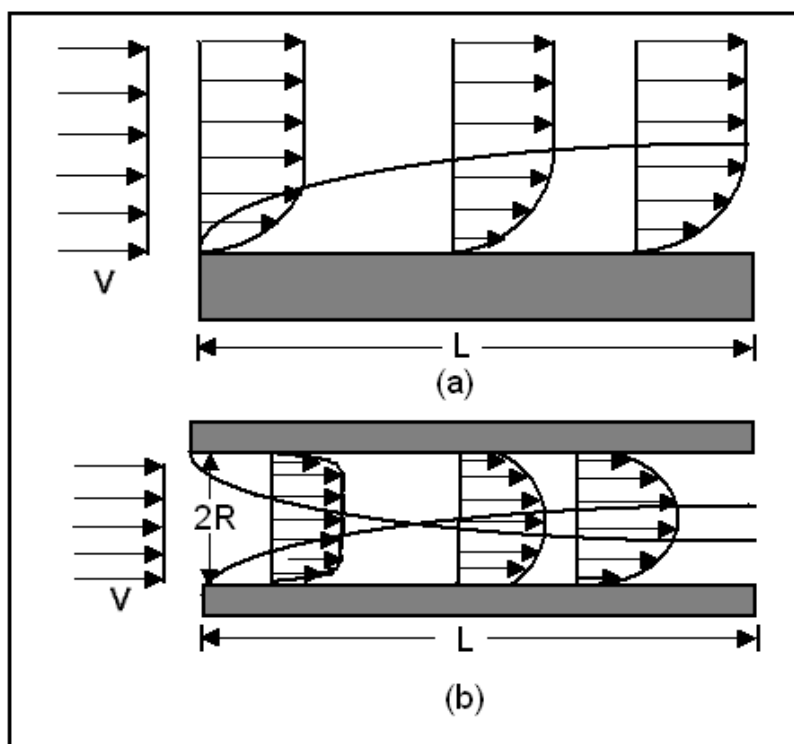


Figure 4.14. Schematic diagrams of laminar gas flow patterns: (a) flow across a flat surface, (b) flow through a circular pipe.

The significant diameter difference between a ZnO nanotip in an array and an isolated ZnO nanotips is related to the different growth environment. At the same conditions, the growth of ZnO nanotips depends on the delivery of reactants to the growth surface. According to the theory of fluid dynamics, gas velocity gradients form during the CVD growth because the gas clings to the growth surface. [Figure 4.14\(a\)](#) shows a schematic diagram of laminar gas flow pattern across a flat surface. [\[110\]](#) Far away from the growth surface, the gas velocity is uniform, but drops to zero at the growth

surface, creating a boundary layer. The incoming reacting species diffuse through the boundary layer and are absorbed at the growth surface. The dissociation of DEZn molecules and oxygen precursors generates Zn and O species, which experience random diffusion at the growth surface and incorporated into the ZnO lattice. In the case of an isolated ZnO nanotip, the flow pattern near the nanotip sidewall is close to the laminar flow pattern across a flat surface. Due the sustaining supply of the reacting species, the sidewalls of the ZnO nanotip expand over time. However, the expansion of the nanotips sidewall in an array is quite different. [Figure 4.14\(b\)](#) shows a simplified diagram of laminar gas flow pattern across a circular tube. The initial uniform axial-flow velocity is altered after the gas enters the tube. Boundary layers develop at the walls and grow with distance along the tube. Beyond certain entry length L , the flow is fully developed and velocity profile no longer changes. The resulting axial flow is proportional to the square of the tube radius R . The slow growth rate of ZnO nanotips' sidewalls can be explained by the laminar flow pattern through a circular tube. The space between neighboring ZnO nanotips is around 5 ~10 nm. The value is below the thickness of stagnant boundary layer and the maximum flow rate in the middle of two neighboring nanotips is significantly reduced. The precursors have difficulties to reach deep into the long “tunnels” of the ZnO nanotip arrays. Therefore, the growth of the sidewalls (ZnO (01 $\bar{1}$ 0) and ZnO (01 $\bar{1}$ l) planes) is mass-transport limited, which depends on the supply of reacting species, and expands slowly due to the scarcity of available precursors. Hence, the high aspect ratio of the ZnO nanotips is not only results from the growth rate difference between crystalline planes; it is also related to the growth environment during the MOCVD growth.

4.4 Summary

Using the same MOCVD growth system, we demonstrate that well aligned ZnO nanotips could be grown on various substrates, such as Si, GaN, c-sapphire and glass. The growth parameters, such as chamber pressure, growth temperature and precursor flows are optimized. The ZnO nanotips have single crystalline quality, high aspect ratio and good optical properties. The morphology and crystalline structure are characterized by scanning electron microscope and X-ray diffraction, respectively. It was found that ZnO grown on various substrates is c-axis preferably oriented. The optical property of the ZnO nanotips is investigated by room temperature and low temperature cathodoluminescence spectroscopy. Strong free exciton emission is observed at 3.37 eV at low temperature of 12-14 K, indicating that MOCVD-grown ZnO has good optical properties. The growth mechanism of forming well-aligned ZnO nanotip array is studied. It is found that the high aspect ratio of ZnO is mainly a result of a spatial blocking effect associated with initial random nucleation on the substrate and the subsequent high growth along ZnO [0001] c-axis direction. After forming vertically aligned ZnO nanotip arrays, the metalorganic precursor vapors barely can reach into the sidewalls of nanotips and the diameter of the ZnO nanotips increases very slowly due the scarcity of available reacting species. The morphology control from GZO film to ZnO to well-aligned ZnO nanotips on a single substrate are realized through temperature modulated growth.

Chapter 5 ZnO Based Dye Sensitized Solar Cells

In previous chapters, we discussed the growth of Ga-doped ZnO TCO films and ZnO nanotip arrays using MOCVD. GZO films with sheet resistance $\sim 25 \Omega/\text{sq}$ and transmittance over 85% in the visible wavelength are achieved. The GZO film is a cost-effective TCO alternative for ITO and FTO. We also demonstrated the growth of well-aligned ZnO nanotip arrays on various substrates. MOCVD-grown ZnO nanotips exhibit high aspect ratio, single crystalline quality, and strong free exciton emission at room temperature. These ZnO nanotips are very promising to be used for the DSSC as the nanostructured semiconductor oxide. In this chapter, we explore the application of these two categories of ZnO material for dye sensitized solar cells.

In recent years, photovoltaic technology has stimulated growing research interest due to the increasing demand for renewable and clean energy. In comparison to conventional solid-state solar cells, the DSSC has attractive features, such as simple process and low-cost fabrication on conductive glass substrate and even plastic substrates. Since Grätzel *et al.* demonstrated a DSSC with overall light-to-electric energy conversion efficiency of 10.4 % in 1991, TiO_2 nanoparticles have been extensively investigated for DSSCs. [6] ZnO is another attractive, but less explored wideband gap semiconductor oxide. DSSCs built from ZnO nanoparticles have achieved the second highest efficiencies after TiO_2 . [12] Various ZnO nanotips of high crystalline quality can be synthesized at low growth temperature. As the MOCVD-grown ZnO is concerned, the combination of well aligned ZnO nanotips and ZnO TCO film provides a promising photoelectrode for dye sensitized

solar cells and polymer-based organic solar cells. Therefore, it is interesting to explore ZnO nanotip/GZO films hybrid structure for solar cell applications.

5.1 Device Structure and Operating Principles

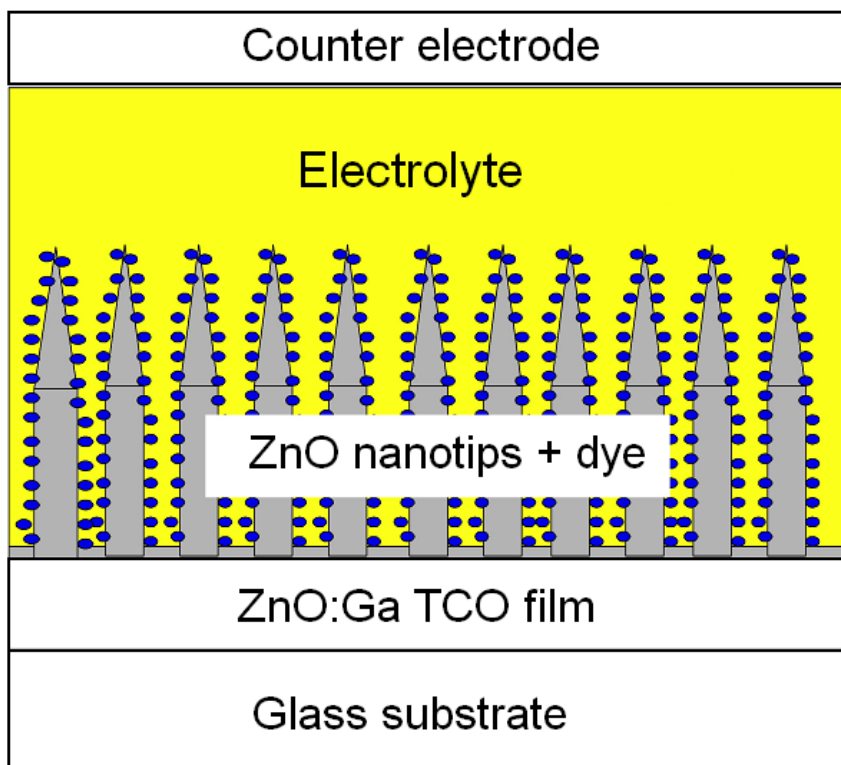


Figure 5.1. A schematic illustration of dye sensitized solar cell using well-aligned ZnO nanotip array and Ga-doped ZnO TCO film as the photoactive electrode.

Figure 5.1 shows the DSSC structure using ZnO nanotips and GZO film. The photoactive electrode consists of a layer of GZO film (~400 nm) and an array of ZnO nanotips (several μm), which are vertically aligned along the substrate surface normal. The GZO film and ZnO nanotips are sequentially grown on glass substrates using

temperature modulated MOCVD growth. To fabricate the solar cells, ZnO nanotips are sensitized by immersing in a 0.3 mM ruthenium polypyridine dye (RuN3, Dyesol) ethanolic solution. A 25 μm microporous polyelofin battery separator (Celgard) soaked with 0.5 M LiI, 0.05 M I_2 , 0.5 M *tert*-Butyl pyridine in methoxypropionitrile electrolyte is placed on the ZnO nanotip array. A platinum foil is clamped with a glass slide on the separator as the counter electrode. The solar cell area is calculated to be 10 mm \times 10 mm.

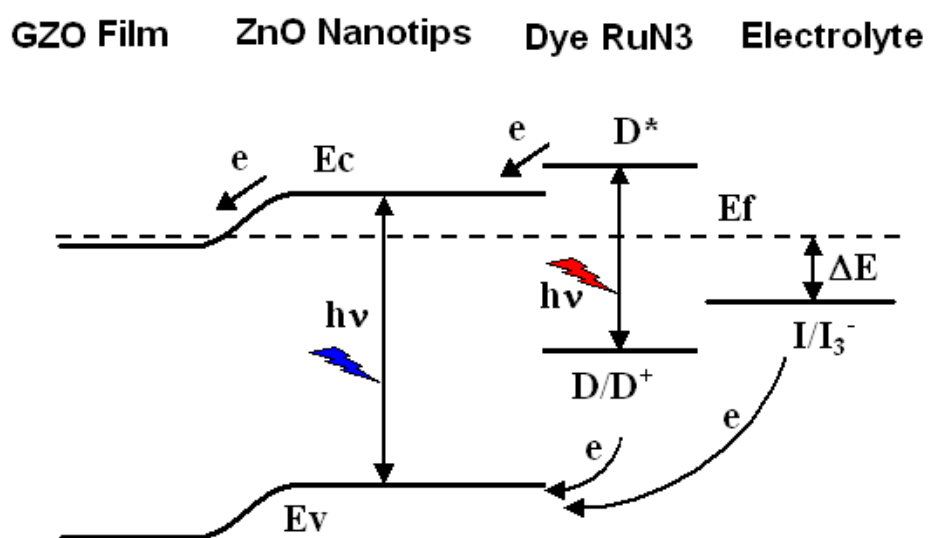
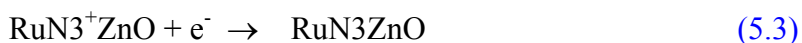
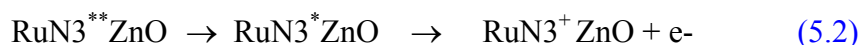
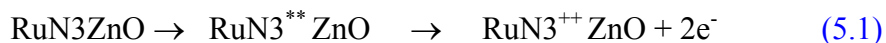


Figure 5.2. A schematic illustration of the energy band diagram of ZnO nanotip/GZO-based dye sensitized solar cells.

The energy band diagram of ZnO nanotip/GZO-based dye sensitized solar cell is shown in [Figure 5.2](#). With an electron affinity of 4.35 eV and a band gap of 3.30 eV, the valence band of ZnO nanotips is 7.65 eV below the vacuum energy level. [\[111\]](#) The redox potential of an electrolyte based on 0.5M LiI and 0.05M I_2 is about +0.3 V versus

normal hydrogen electrode (NHE), corresponding to the 5.0 eV below the vacuum energy level. Since the light is incident from the backside of TCO electrode, UV photons with energy higher than the band gap energy of ZnO (3.30 eV) are absorbed by the ZnO photoelectrode and raise electrons from the valence band to conduction band of ZnO. The photogenerated electrons diffuse through the ZnO nanotip array to the TCO electrode, leaving the holes in the ZnO valence band. As the valence band energy level of ZnO is lower than that of the electrolyte and the electrolyte is in close contact with the ZnO nanotips, the holes in the ZnO valence band are replenished with electrons donated from ions in the electrolyte. The photons with energy lower than the band gap energy of ZnO are harvested by the dye molecules, which are anchored at the surface of ZnO. The photogenerated charges are separated at the dye/ZnO interface. The oxidized dye molecules are reduced by the electrons donated from the ions in the liquid electrolyte.

For good photovoltaic performance, it is important to maximize the absorption of incident photons and ensure the efficient electron injection into the conduction band of semiconductor oxide. The anchoring of the RuN3 dye molecules onto ZnO surface is illustrated in [Figure 5.3](#). The basic photovoltaic processes that occur in the photoactive dye/oxide interface and electron transfer between RuN3 dye molecules and ZnO semiconductor oxide in redox electrolyte are described as following:



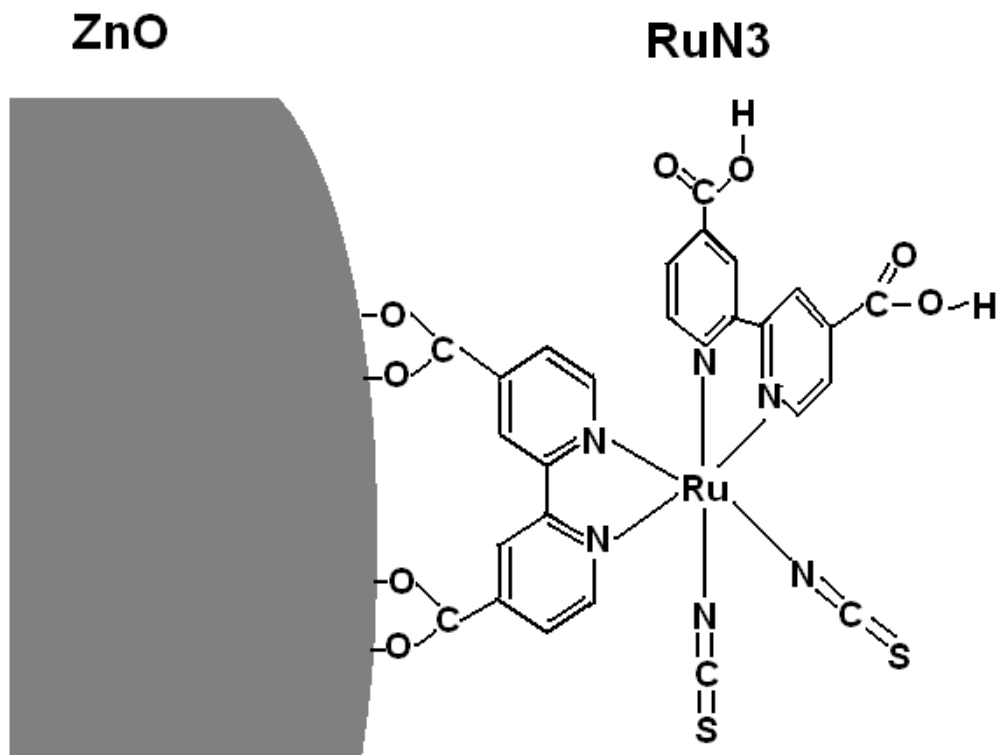


Figure 5.3. The schematic illustration of dye RuN₃ molecules anchoring on ZnO surface.

The RuN₃ dye captures an incident photon and generates a long-lived exciton. (Eq. 5.1 and 5.2) The excitons are separated at the dye/oxide interface and the electron is injected into the conduction band of ZnO nanotip and holes diffused to the opposite side of the device by the means of redox species in the liquid electrolyte. The two possible electron transfer pathways are electron injection from the fully relaxed excited state (RuN₃^{*}), and from nonthermalized, higher lying excited states (RuN₃^{**}). When an electron is injected, the dye cation (RuN₃⁺) is formed together with an electron in the conduction band of ZnO (ZnO(e⁻)). Backward electron transfer from the conduction band of ZnO semiconductor to the dye cation is the unwanted reverse reaction, which restores the original ground state of dye molecules (Eq. 5.3), and does not contribute to the

photocurrent. The ratio of the forward injection and backward electron transfer depends on the relaxation time. It is reported that the forward electron injection process occurs in femtosecond to picosecond time scale, while the backward electron transfer occurs in the range of microsecond to millisecond time scale. [112] The difference of several orders of magnitude between the time constants of electron injection and backward electron transfer is one of the important properties, which makes the RuN3-ZnO interface an efficient light-to-electricity converter. A key issue in the photo-induced processes of dye-sensitized semiconductor films has been the mechanism of ultrafast, sub-hundred femtosecond time scale electron injection, whether it occurs from non-thermalized states prior to energy equilibration or over all electronic, vibrational, and rotational degrees of freedom. The absorption of a photon by a dye molecule happens via an excitation between the electronic states of the molecule. The excitation of the Ru complexes via photon absorption is of metal to ligand charge transfer (MLCT) type. This means that the highest occupied molecular orbital (HOMO) of the dye is localized near the metal Ru ion, whereas the lowest unoccupied molecular orbital (LUMO) is localized at the ligand species, in this case, at the bipyridyl rings. At the photo-excitation, an electron is lifted from the HOMO level to the LUMO level. The LUMO energy level, extending even to the -COOH anchoring groups, is spatially close to the ZnO surface, which means that there is significant overlap between the electron wave functions of the LUMO energy level of dye molecules and the conduction band of ZnO. This directionality of the excitation is one of the reasons for the fast electron transfer process in the dye-ZnO system.

In the DSSCs, the electron transport in the semiconductor oxide is dominated by diffusion since there is no significant electrical field present. In nanoparticle films, the nature of electron transport in oxide nanoparticle films is well understood using time-resolved photocurrent and photovoltage measurements and the corresponding modeling study. [113,114,115] It is found that the electron transport in nanoparticle films is through a trapping-detrapping diffusion process, in which the photogenerated electrons interact with charge traps as they undertake a random walk through the nanoparticle network. In comparison to nanoparticle films, the ZnO nanotips are vertically aligned along the substrate surface normal. They provide direct conduction pathways from the point of charge injection to the TCO electrode. Furthermore, ZnO nanotips are of single crystalline quality with a low defect density. The diffusion of electrons in the ZnO nanotips does not suffer from the scattering at the crystalline boundaries and avoids being trapped in the charge traps, therefore, electron transport speed in ZnO nanotips is expected to be much faster.

Most of the reported DSSCs are built from TiO_2 particle films deposited on FTO substrates. At the FTO/ TiO_2 interface, an electrostatic field creates an energy barrier for electron transfer from the TiO_2 into FTO. [116] Unlike the FTO/ TiO_2 , ZnO nanotips and GZO electrode belong to the same material system. They have the same values of electron affinity and the energy band bending of the ZnO/GZO homojunction is aligned without the presence of a significant energy barrier. The Fermi level difference of ZnO and GZO results in a built-in electric field that favors the electron transfer from the ZnO nanotips into the GZO electrode as shown in [Figure 5.2](#).

5.2 Solar Cell Testing System

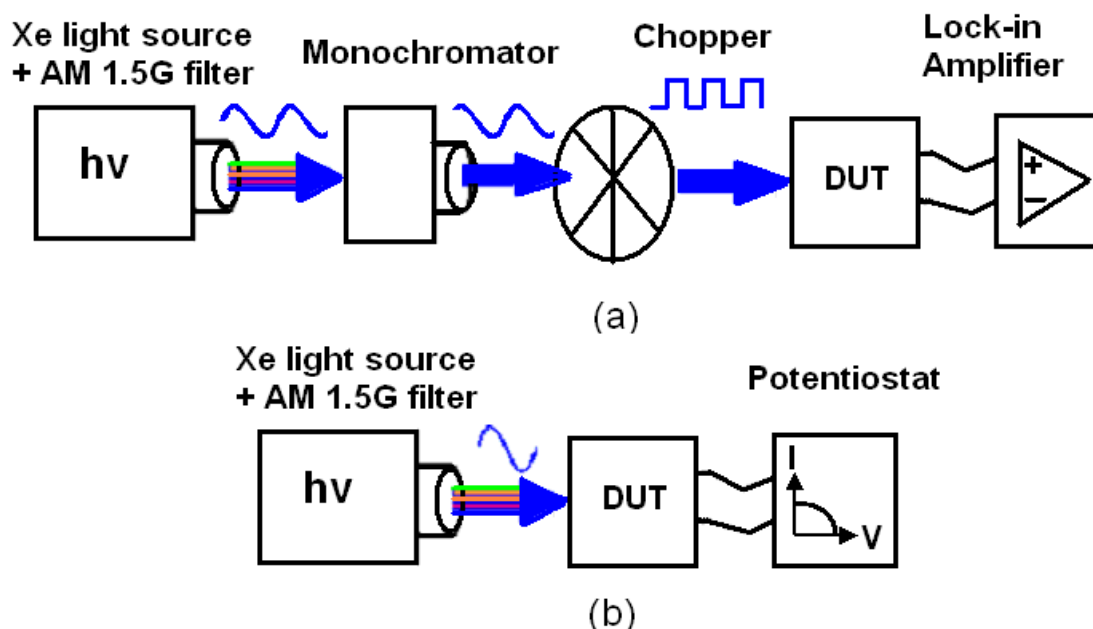


Figure 5.4. Schematic illustration of solar cell testing system, (a) quantum efficiency measurements; (b) power conversion efficiency measurements.

Figure 5.4 shows the schematic illustration of the solar cell testing system. The incident photon-to-current conversion efficiency (IPCE) measurements are performed using a monochromatic chopped light and a lock-in amplifier as shown Figure 5.4(a). Briefly, the light from a 150 W Xe light source (Oriel Q60000) passes through an AM 1.5G filter (100 mA/cm^2) chopped at 20 Hz by a Stanford Research SR540 light chopper. The wavelength of IPCE measurement is scanned from 300 nm to 800 nm with an Oriel Cornerstone 130 monochromator and focused on the sample through fiber optics. The measurements are taken on an area of 0.08 cm^2 , and the measured currents are in the range of several $\mu\text{A/cm}^2$. The light power as a function of wavelength is calibrated prior

to each measurement with a silicon photodiode (Texas Instrument OPT101). The sample photocurrent as a function of incident wavelength is acquired at zero bias voltage with an EG&G 5210 lock-in amplifier. For the power efficiency measurements, the solar cells are directly exposed to the light generated from the 150 W Xe light source (Oriel Q60000) filtered through an AM 1.5G filter (100 mA/cm²). A potentiostat (EG&G 273A) is connected to the device to measure the photocurrent and photovoltage as shown in [Figure 5.4\(b\)](#). The data acquisition, monochromator control and data analysis is integrated with homemade Labview program.

The spectral responsivity $PR(\lambda)$ (A/W) of a solar cell is defined as the variation of the short-circuit current as a function of incident light power, which is given by

$$PR(\lambda) = J(\lambda)/P(\lambda) \quad (5.4)$$

where $J(\lambda)$ (mA/cm²) is short-circuit photocurrent density and $P(\lambda)$ (mW/cm²) is the incident light power as a function of incident wavelength λ .

From [Eq. 5.4](#), the incident photo-to-current conversion efficiency (IPCE) is defined as

$$IPCE(\lambda) = PR(\lambda) \cdot h \cdot c / (q \cdot \lambda) \quad (5.5)$$

where h is Plank constant, c is the speed of light in vacuum, q is the charge of electron, and λ is the wavelength of incident photon.

For broadband variable sunlight simulated measurements, the I - V curves are recorded with an EG&G 273A potentiostat at 200 mV/s in the dark and under variable illumination intensity from a 50 W halogen light source. The light intensity is calibrated for the spectral mismatch with the AM 1.5G (100 mA/cm²) solar spectrum. For one sun conditions, the Xe light source intensity with AM 1.5G filter is adjusted and measured to

be 100 mW/cm^2 with a Newport thermopile. The power conversion efficiency η is calculated from the equation

$$\eta(\%) = (J_{sc}) \cdot (V_{oc}) \cdot FF / (P_{in}) \times 100\% \quad (5.6)$$

where J_{sc} (mA/cm^2) is the short-circuit current density, V_{oc} (V) is the open circuit voltage, FF is the fill factor, which describes the power extraction efficiency of solar cells, and P_{in} (mW/cm^2) is the overall illumination power incident on the solar cells.

5.3 DSSCs Using Liquid Electrolyte

5.3.1 ZnO/Liquid Electrolyte Interface

In the conventional solid-state solar cells, two materials with different types of conductivity form a pn junction and Fermi levels are aligned in equilibrium conditions, which is associated with the displacement of majority carriers within semiconductor near the pn interface and the creation of a depletion region. In the DSSC, when the redox liquid electrolyte is in contact with ZnO surface, there is an analogy with the Fermi level in solid-state pn junction interface. The ions in the redox electrolyte have two different states, i.e. an oxidized state (-ox) Γ^- and a reduced state (-red) I_3^- . The reduced state I_3^- ion is converted to an oxidized state Γ^- ion by acquisition of a negative charge at the anodic electrode, and the process is reversible at the cathode. The potential, at which no current passes at a reversible electrode, is the redox potential, at which both ionic components are at equilibrium.

Figure 5.5 shows the IPCE spectrum of ZnO nanotip/GZO photoelectrode immersed in Γ^-/I_3^- redox electrolyte without dye sensitization. The cell built from $0.8 \text{ }\mu\text{m}$ long ZnO nanotips exhibits an absorption peak at $\sim 378 \text{ nm}$ with an IPCE value of 16.5%. The UV

light harvesting is realized through direct charge exchange between the ZnO photoelectrode and redox electrolyte without the involvement of dye molecules. The UV photon is absorbed by the ZnO photoelectrode and the photo-induced electrons in ZnO conduction band diffuse through ZnO nanotips to the TCO electrode, leaving the holes in the ZnO valence band, which are replenished with electrons donated from the red- I_3^- ions. The high IPCE peak centered at 378 nm indicated that the back transfer of conduction band electron of ZnO nanotips to the electrolyte is much slower in comparison to the forward electron transfer to the TCO electrode. The UV light harvesting could be exploited to improve the device stability of DSSCs under high illumination by preventing dye molecules from UV exposure.

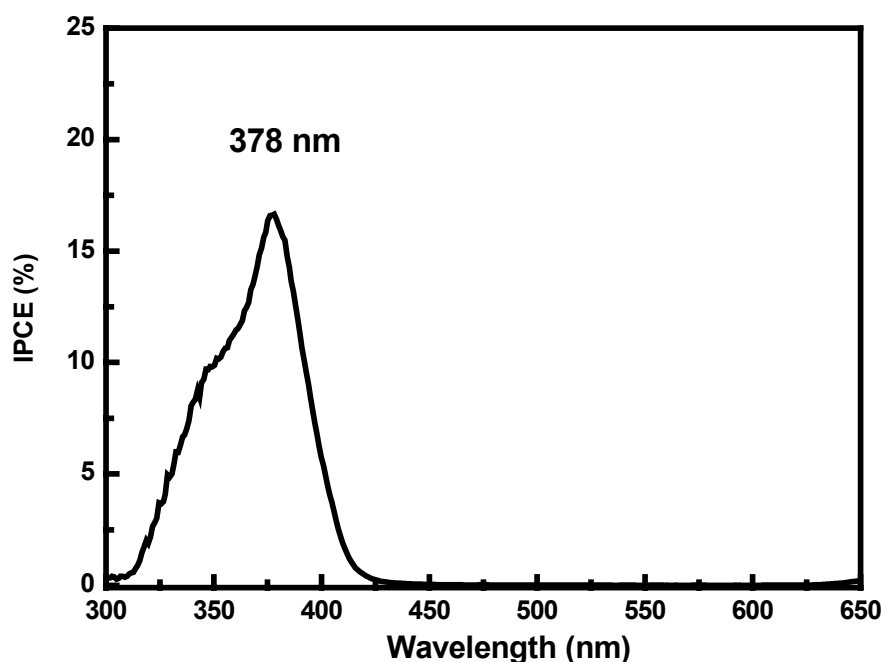


Figure 5.5. An incident photon-to-current conversion efficiency (IPCE) spectrum of the ZnO nanotips in contact with the liquid I^-/I_3^- redox electrolyte.

5.3.2 Photoresponse of ZnO Nanotip-based DSSCs

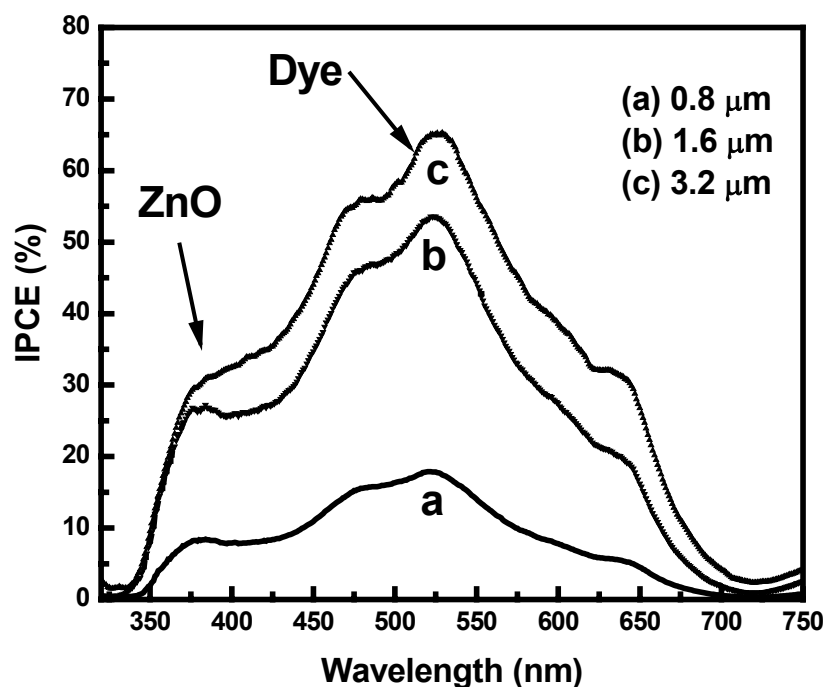


Figure 5.6. Incident photon-to-current conversion efficiency (IPCE) spectra of the ZnO nanotip-based dye sensitized solar cells with three different ZnO nanotip lengths of 0.8 μm, 1.6 μm, and 3.2 μm.

Figure 5.6 shows the IPCE spectra of DSSCs with three different ZnO nanotip lengths. The maximum absorption peaks are observed at the incident wavelength of ~530 nm. It was found that IPCE increases with the ZnO nanotips length, with values of 18%, 53%, 65% for 0.8 μm, 1.6 μm, and 3.2 μm ZnO nanotip length, respectively. In addition, another photocurrent peak at 378 nm is clearly observed in all the curves. The values of IPCE at 378 nm are 8%, 26% and 31% for 0.8 μm, 1.6 μm, and 3.2 μm nanotip length, respectively. This photocurrent peak is attributed to the UV light harvesting by the ZnO

nanotips and GZO films. ZnO has a band gap of ~ 3.3 eV at room temperature and exhibits a strong UV absorption. This charge transfer pathway is confirmed by the observation of the photocurrent peak at ~ 378 nm in the absence of dye sensitization. The oxidized dye molecules are restored by electrons donated transferred from the I_3^-/I^- electrolyte.

Many dyes, including organic dyes and transition metal complexes, have been employed in DSSCs. Transition metal complexes based on Ru(II), Os(II), Pt(II), Fe(II), Re(I) and Cu(I) have been extensively investigated for DSSC applications. Up to date, Ru(II)-based charge-transfer polypyridyl complexes show the highest energy conversion efficiency. This is because of their intense charge-transfer (CT) absorption in the whole visible range, moderately intense emission with fairly long lifetime in fluid solutions at ambient temperatures, high quantum yield for the formation of lowest CT excited state, and redox reactivity and ease of tunability of redox properties. Photoexcitation of the metal-to-ligand charge-transfer (MLCT)-excited states of adsorbed dye leads to an efficient injection of electrons into the conduction band of oxide. From [Figure 5.6](#), it is observed that at the wavelength above ~ 630 nm, the IPCE is dramatically decreased, which indicates a low light harvesting percentage at longer visible wavelength. The low IPCE value at longer visible wavelength is a major drawback of Ru based dye molecules. In order to improve the light harvesting efficiency, dyes with high light absorption overlap with the solar spectrum have to be developed.

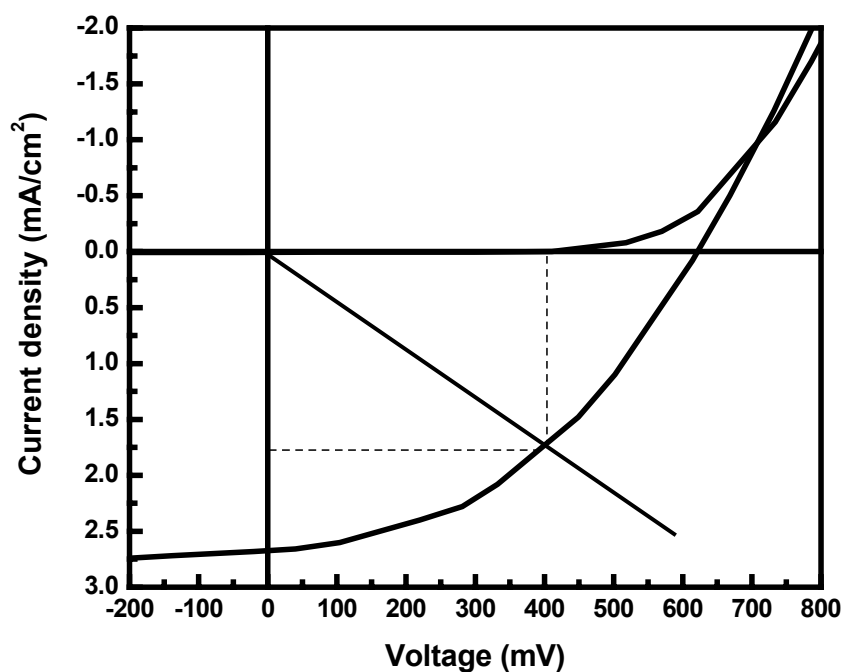


Figure 5.7. I - V characteristics of 3.2 μm ZnO nanotip-based dye sensitized cells in the dark and under the illumination of Xe AM 1.5G (100 mA/cm^2) simulated sunlight.

Figure 5.7 shows the I - V characteristics of a dye-sensitized solar cell built from 3.2 μm long ZnO nanotips. In the dark, the cell shows rectifying characteristics. Under the illumination of AM 1.5G (100 mA/cm^2) simulated sunlight, the I - V curve is shifted downwards to the fourth quadrant, indicating power generation. The short circuit current density J_{sc} and power efficiency η as a function of ZnO nanotip length are shown in Figure 5.8.

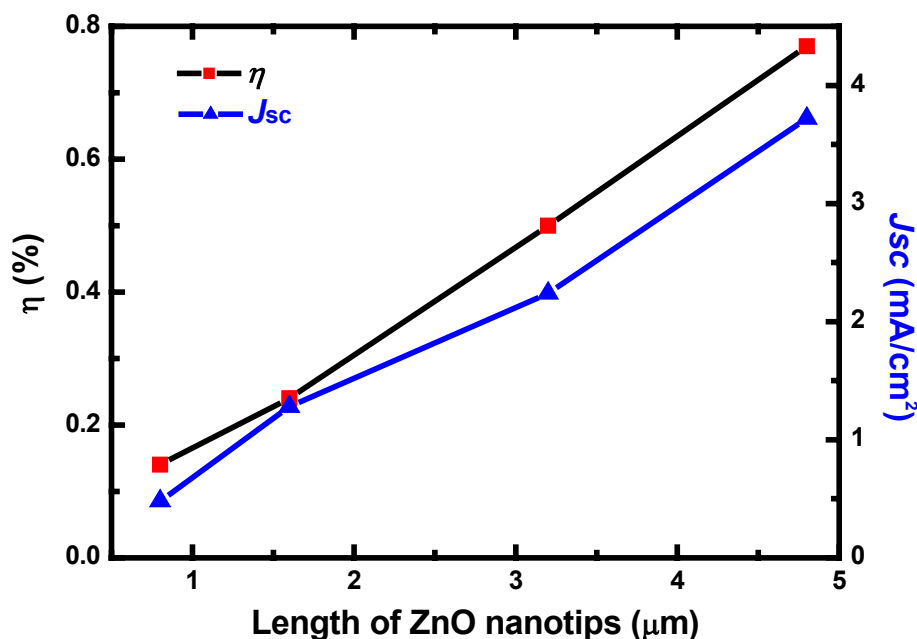


Figure 5.8. Power conversion efficiency (η) and short-circuit current density (J_{sc}) of DSSCs as a function of ZnO nanotip length. The photoresponse is measured under the illumination of Xe AM 1.5G simulated sunlight (100 mW/cm^2) with a 1.0 cm^2 cell area.

For the cell with 0.8 μm ZnO nanotips, the short-circuit current density J_{sc} and the open circuit voltage V_{oc} are 1.0 mA/cm^2 and 0.367 V , respectively. The low value of V_{oc} might be caused by the insufficient dye coverage and the direct contact of liquid electrolyte with the GZO electrode. The low value of J_{sc} is attributed to less available ZnO surface area for dye anchoring and inefficient light harvesting, as the surface area of ZnO nanotips is approximately proportional to the ZnO nanotip length. As the length of ZnO nanotip increases, the open circuit voltage increases. The typical open circuit voltage for 3.2 μm ZnO nanotip is $610 \sim 630 \text{ mV}$. The short circuit current density of the

cells built from 0.8 μm , 1.6 μm , 3.2 μm , and 4.8 μm long ZnO nanotips are 1.0, 1.7, 2.8, and 4.1 mA/cm^2 , respectively. The corresponding power efficiency is calculated to be 0.14%, 0.24%, 0.5% and 0.77 % for 0.8, 1.6, 3.2 and 4.8 μm ZnO nanotips. The monotonously increase of power efficiency with nanotips length indicates that dye loading is the main limiting factor, and further improvement in power efficiency can be achieved by increasing the ZnO nanotip length. The fill factor is calculated to be ~ 0.40 for cells built from 3.2 μm ZnO nanotips and is relatively constant at light intensity from 40 to 260 mW/cm^2 . This value of fill factor is lower than typical TiO_2 DSSC solar cells (0.6~0.7). This might be attributed to the recombination of photo-excited carriers between the ZnO nanotips and triiodide ions in the electrolyte. It may also be attributed to the relatively large area of the solar cell (1.0 $\text{cm} \times 1.0 \text{ cm}$). As the device area is reduced to 0.28 $\text{cm} \times 0.28 \text{ cm}$, the fill factor is increased to 0.55 and the power efficiency is increased from 0.77 to 1.11% for the 4.8 μm ZnO nanotips. Lowering the sheet resistance of the GZO electrode and using grid electrode are expected to achieve better fill factors.

5.3.3 Electron Transport in ZnO Nanotips

The electron transport in nanostructured photoelectrode is mainly through diffusion, since there is no significant electrical field present in the dye/ZnO interface. The diffusion current density is given by

$$I = q \cdot D_n \cdot \frac{d^2 n(x)}{dx^2} \quad (5.7)$$

where q is the charge of electron, D_n is the diffusion coefficient of electrons in the semiconductor oxide, and $n(x)$ is photogenerated carrier concentration.

The diffusion coefficient of electron D_n is related to the carrier mobility through the Einstein equation, which is given

$$D_n = \frac{KT}{q} \mu_n \quad (5.8)$$

where K is the Boltzmann constant, T is the absolute temperature, q is the charge of electron, and μ_n is the carrier mobility in semiconductor oxide.

In order to improve the charge transport efficiency, high electron μ_n mobility in the photoelectrode is required. In nanoparticle-based DSSCs, the high density of grain boundaries and the poor connection between nanoparticles induce defects and interface states, which act as charge trapping centers and slow down the electron diffusion. The electron transport efficiency decreases as the concentration of photo-generated carriers increases, which is due to the high density of charge traps. In comparison to the nanoparticles, the ZnO nanotips have well-aligned vertical columnar structure. TEM characterization revealed that a single ZnO nanotip is of single crystalline quality with low defect density. The electron diffusion in ZnO nanotips is not affected by potential barrier induced by grain boundaries and particle interface. Hence, ZnO nanotip array provides direct conduction pathways for charge transport, and the electron transfer time from the point of carrier generation to the collection electrode is significantly reduced.

To compare the electron transport speed in ZnO nanotips with ZnO nanoparticles, we prepared both ZnO nanotips and ZnO nanoparticle-porphyrin sensitized solar cells. The ZnO are deposited on 100 nm Au coated substrate with a 20 nm Ti layer as the adhesion layer. The ZnO nanotips uniformly covered the Au substrate so that no gold surface is in contact with the electrolyte. ZnO nanotips and ZnO nanoparticle film are sensitized by immersion in a 0.4 mM EtOH solution, rinsed and immediately sealed with the Pt-coated

FTO counter electrode. The electrolyte solution (0.05 M I_2 , 0.10 M LiI, 0.6 M TBAI in 3-methoxypropionitrile) is introduced in the cells by capillary force. Both dye-sensitized nanostructured ZnO solar cells give good solar spectral response, clearly reflecting the characteristic porphyrin absorption spectrum. IPCE values in the order of 30% are achieved for both ZnO nanotips and ZnO nanoparticles. A comparison of electron transport times in the two types of nanostructured ZnO solar cells measured under the illumination of ~ 640 nm wavelength and electron transport time is shown in Figure 5.9.

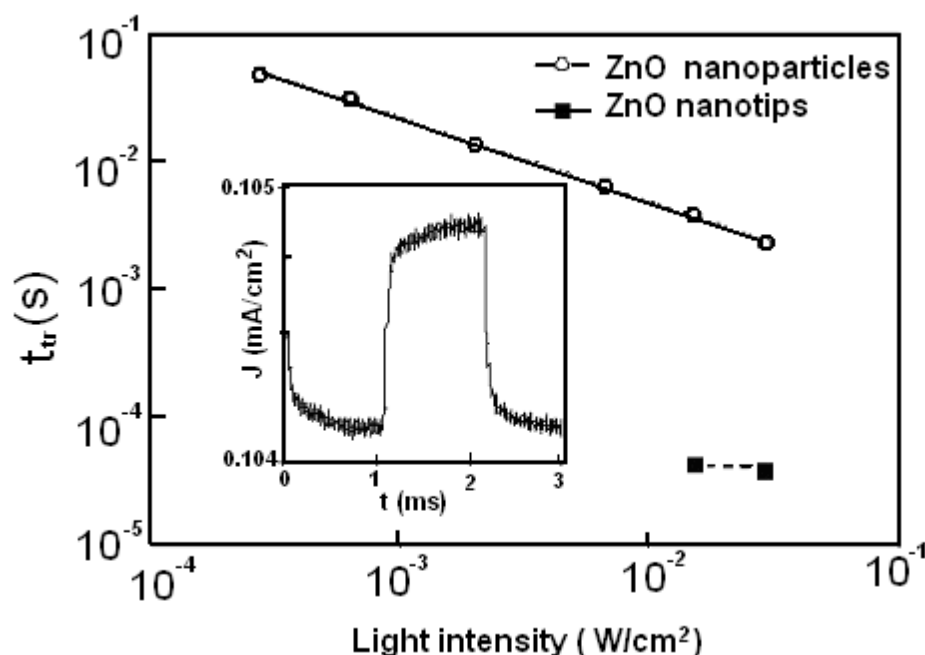


Figure 5.9. Electron transport times of DSSCs built from well aligned ZnO nanotips and ZnO nanoparticles as a function of light intensity (monochromatic light ~ 640 nm). Electron transport times are determined from the short circuit photocurrent response to a small square wave modulation of the light intensity. The inset shows the time-resolved photocurrent of ZnO nanotips-sensitized cells.

The charge present in the ZnO nanotips and ZnO particle films under short-circuit conditions is estimated by switching off the light and then integrating the decaying current. Electron transport speed in ZnO nanoparticle film is relatively slow (10 ms), and is comparable to that found in colloidal TiO₂ films. The transport time decreases slightly with illumination intensity. The photocurrent response time in ZnO nanotips is about two orders of magnitude faster ($\sim 30 \mu\text{s}$). This can be explained partly by the difference in film thickness, as the ZnO nanoparticle layer is about four times thinner. Taking this into account, the photocurrent response time in ZnO nanotips is around 4-5 times faster than in nanoparticles. This implies that the electron transport in the ZnO nanotips is improved as expected for the highly vertical columnar structure. The transport of electrons in ZnO nanoparticle films appears to be limited by large amount of localized electronic states in the band gap of the oxide, which acts as traps and determine the rates of transport and recombination of photogenerated electrons. [117] The actual electron transport time in the nanotip may be much faster than the measured $\sim 30 \mu\text{s}$, as the response speed of photocurrent will be limited by the RC -time of the testing system, where the resistance R is determined by the series resistance of the electrodes ($\sim 10\Omega$) and the capacitance C by the capacity of the electrode/electrolyte interfaces.

5.3.4 Equivalent Circuit Model of DSSCs

In order to improve the cell performance, it is important to clarify the performance limiting factors of the solar cells. Construction of theoretical models and simulation are necessary to understand the device parameters. An ideal solar cell can be represented by a

current source connected in parallel with a rectifying diode. The corresponding I - V characteristics is described by the solar cell equation

$$I = I_{ph} - I_o \cdot (e^{\frac{qV}{KT}} - 1) \quad (5.9)$$

where I_{ph} is the photocurrent, I_o is the diode saturation, K is the Boltzmann constant, T is the absolute temperature, and q is the charge of electron.

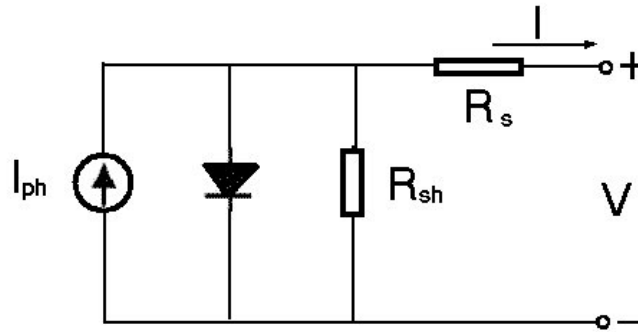


Figure 5.10. An electrical equivalent circuit model of solar cells. R_s and R_{sh} are resistors that represent electrical losses.

The I - V characteristics of a real solar cell usually differ to some extent from the ideal characteristics. The DSSC can be analyzed using a simple equivalent circuit as shown in Figure 5.10. In this equivalent circuit, the current source I_{ph} results from the excitation of excess carriers by incident solar radiation. A diode in parallel with a shunt resistor (R_{sh}) represents the oxide/oxide interface, and a series resistor (R_s) represents the resistance around the circuit loop. The shunt resistance is due to leakage current across the pn junction around the cell edge, and the presence of crystal defects and/or impurities in the bulk and at the surface of semiconductor oxide. The series resistance is mainly caused by

the bulk resistance of semiconductor materials, metallic contacts, and interconnections, and contact resistance between the metallic contacts and semiconductor oxide.

The photocurrent I_{ph} , can be calculated by integrating the product of an incident photon flux density $I(\lambda)$ and the incident photon-to current conversion efficiency $IPCE(\lambda)$ over the wavelength λ of incident light, which is given by

$$I_{sc} = \int q \cdot I(\lambda) \cdot (1 - r(\lambda)) \cdot IPCE(\lambda) \cdot d\lambda \quad (5.10)$$

where q is the electron charge, $I(\lambda)$ is the incident photon flux density, $r(\lambda)$ is the incident light loss associated with the light reflection and absorption of conducting glass substrate, and $IPCE(\lambda)$ is the incident monochromatic photon-to-current conversion efficiency.

In the case of ZnO nanotip-based DSSC, light absorption occurs mainly at the light-absorbing dye molecules, the IPCE is expressed as:

$$IPCE(\lambda) = \eta_{ha} \cdot \eta_{in} \cdot \eta_{ex} \quad (5.11)$$

where η_{ha} is the light-harvesting efficiency, η_{in} is the electron injection efficiency, and η_{ex} is the electron extraction efficiency.

The light harvesting efficiency of DSSCs depends on (1) the properties of dye molecules, such as the band gap, absorbance, and extinction coefficient, (2) dye loading efficiency in the oxide surface, (3) the optical path within the electrode. The I-V curves of DSSCs based dye sensitized solar cells are described with a one-diode equivalent circuit

$$I = I_{ph} - I_o \cdot \left(\exp\left(\frac{V + I \cdot R_s}{\eta V_T}\right) - 1 \right) - \left(\frac{V + I \cdot R_s}{R_{sh}} \right) \quad (5.12)$$

where I_{ph} (mA/cm²) is the photocurrent, I_o (mA/cm²) is the diode saturation current, η is the diode ideality factor, R_s is the series resistance, and R_{sh} is the shunt resistance. The short circuit current is given by

$$I_{sc} = I_{ph} - I_o \cdot [\exp(\frac{I_{sc} \cdot R_s}{n V_T}) - 1] - \frac{I_{sc} \cdot R_s}{R_{sh}} \quad (5.13)$$

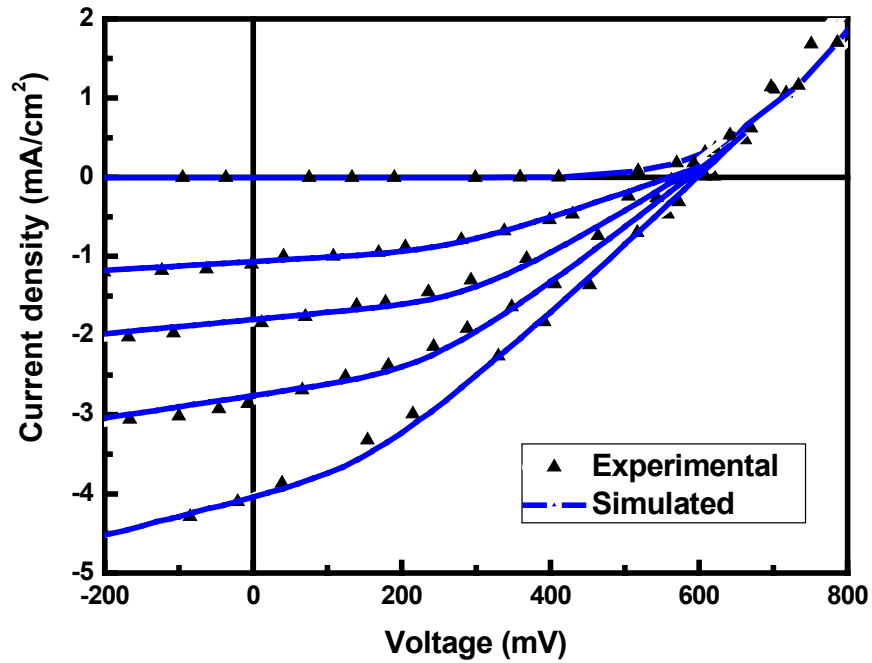


Figure 5.11. The experimental and simulated I - V characteristics of ZnO cells built from ZnO nanotips with length of 0.8, 1.6, 3.2 and 4.8 μm .

Shown in Figure 5.11 are the experimental and simulated I - V characteristics of the cells built from four different ZnO nanotips lengths, i.e. 0.8, 1.6, 3.2 and 4.8 μm . The curves represented by the triangle symbol are from the experimental results and the curve in solid line is the simulated results using the one-diode equivalent model. It is found that the two sets of I - V curves agree well at the biasing voltage from -200 mV to 650 mV.

The ideality factor of the diode is around 1.05, indicating good rectifying properties of the dye/oxide interface. The shunt resistance is of the order of $\sim 10^3 \Omega \cdot \text{cm}^2$. As the photocurrent density increases, the shunt resistance decreases, photoconductive current is observed. The photoconductive current may be attributed the backward electron transfer from the ZnO conduction band to the ZnO electrolyte. The series resistance of the cells is $\sim 100 \Omega \cdot \text{cm}^2$ and is relatively high in comparison to solar cells built from TiO_2/FTO , which results in a low fill factor. The series resistance of the cells is $\sim 100 \Omega \cdot \text{cm}^2$ and is relative high, which results in a low fill factor of 0.31. The series resistance of the solar cells is mainly attribute to the relatively high sheet resistance of the GZO films. As the device area is reduced $1.0 \text{ cm} \times 1.0 \text{ cm}$ to $0.28 \text{ cm} \times 0.28 \text{ cm}$, the fill factor is increased to 0.55 and the power efficiency is increased from 0.77 to 1.11% for the $4.8 \mu\text{m}$ ZnO nanotips. The recombination rate at the dye/ZnO does not increase significantly with the ZnO nanotip length as attested by the constant value of fill factor (resp. 0.28, 0.33, and 0.32 for 1.6, 3.2, $4.8 \mu\text{m}$ ZnO nanotips). We attribute the low recombination rate to the non-trap limited electron transport in the ZnO nanotips. The improvement of short circuit current could be achieved by increasing the length of ZnO nanotips, which improves the dye/oxide interface for better light absorption. By increasing the length of ZnO to $6.4 \mu\text{m}$ and reducing the shunt resistance to $10 \Omega \cdot \text{cm}^2$, power conversion efficiency of 3.94 % is predicted from the simulation using the equivalent circuit model.

5.4 DSSCs Using Gel Electrolyte

Grätzel *et al.* demonstrated a DSSC with overall light-to-electric energy conversion efficiency of 10.4 % in 1991. [6] Since then, little progress has been made in absolute

power conversion efficiency. This efficiency value is competitive with amorphous silicon thin film solar cells. However, besides power conversion efficiency, two other requirements must be met for ensuring a successful commercial future of this technology, i.e. (i) very low-cost fabrication and (ii) high device stability. In recent years, DSSC has stimulated growing research interest due to the increasing demand for renewable and clean energy. Although DSSCs based on liquid redox electrolytes have reached high efficiency, however, the liquid electrolyte has low thermal and chemical stability. Furthermore, the liquid may evaporate when the cell is imperfectly sealed. The permeation of water or oxygen molecules and their reaction with electrolytes may also degrade cell performance. Liquid electrolytes also reduce the manufacturability of multi-cell modules because cells must be series connected electrically but separated chemically to achieve desired output voltage, preferably on a single panel. [118] Recently, many attempts have been made to solve the above problems by replacing liquid electrolyte with solid or quasi solid-state hole conductors. Compared with those using liquid-phase redox electrolytes, the efficiency of solid-state DSSCs utilizing p-type semiconductors has yet to be improved. The recent progress of solid-state DSSCs, including solid-state hole conductors and previous research on the mechanism of solid-state DSSCs was reported by Li. [1]

An alternative choice to improve the device stability is to use semi-solid gel electrolyte, which has the properties of relatively high ionic conductivity and easy solidification. The use of conducting polymers as electrolytes or electrode materials for the development of plastic-like electrochemical devices is an appealing concept that dates back to the late 1980s. Ionically conducting polymers, such as poly (ethylene oxide)

(POE) could be used in solid-state lithium-ion batteries in conjunction with the common inorganic oxide intercalation cathodes. From then on, polymer electrolytes have been widely used in lithium batteries, redox type laminated supercapacitors, and multi-chromatic optical windows.

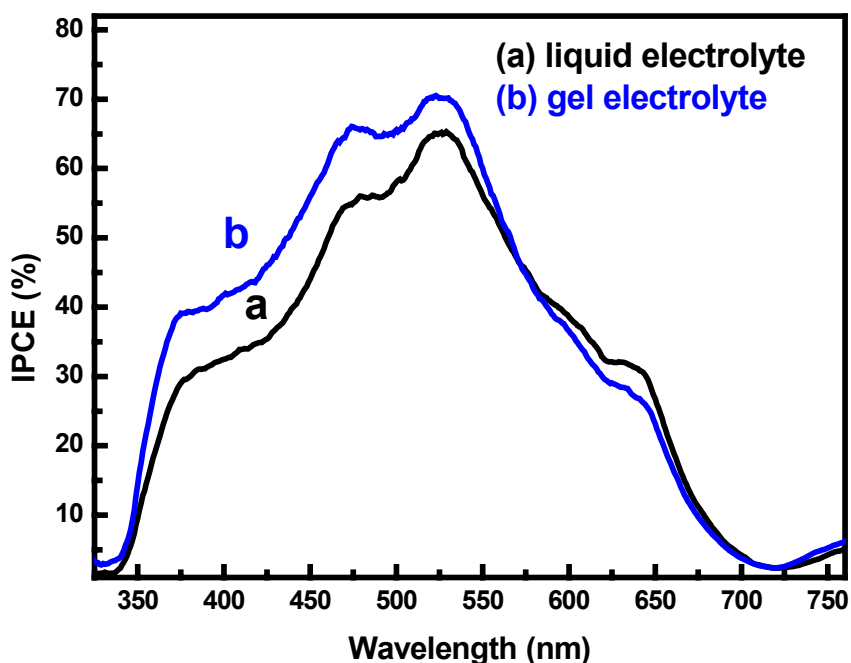


Figure 5.12. Incident photo-to-electrical conversion efficiency (IPCE) spectra of 3.2 μm ZnO nanotip-based dye sensitized solar cells using gel and liquid electrolyte.

In this part, we investigate the feasibility of replacement of liquid electrolyte with semi-solid gel electrolyte in the DSSCs. A polymer based on N-Methyl pyrrolidinone (NMP) gelled with poly(vinyl-difluoroethylene-hexafluoropropylene) copolymer (PVDF-HFP) is used as the semi-solid gel electrolyte. NMP is an ideal solvent for PVDF-HFP copolymers and PVDF homopolymers as stable gels can be formed by their mixtures. Gel electrolytes containing liquid electrolyte and gelator are first injected into

photoelectrode. The impregnation of the solar cells is achieved by heating the cells at temperature of $\sim 80^{\circ}\text{C}$.

Dye sensitized solar cells (DSSC) are built with $3.2\ \mu\text{m}$ ZnO nanotip arrays grown on GZO films. Gel electrolyte provides high device stability compared with liquid electrolyte. However, the fill-in process in nanoparticle-sensitized solar cells presents a challenge as the gel electrolyte usually has higher viscosity than the liquid electrolyte. Lower power conversion efficiency in TiO_2 nanoparticle sensitized solar cells is observed when using the gel electrolyte. Compared with nanoparticle films, MOCVD-grown ZnO nanotips are well aligned along the substrate surface normal; therefore, form straight “trenches” from the top to the base of the ZnO nanotip array. The diameters of the “trenches” between the neighboring nanotips are in the range of 5~10 nm, which is larger than the porous size of typical nanoparticle film. Therefore, the gel electrolyte can easily penetrate into the ZnO nanotips array and efficiently contact with the dye sensitized ZnO surface.

Figure 5.12 compares the incident photo-to-current conversion efficiency (IPCE) spectra of DSSC using gel electrolyte and liquid electrolyte built from the same ZnO nanotips under the same impregnation conditions. The peak IPCE values (at $\sim 530\ \text{nm}$) for the gel and liquid electrolyte are 70% and 65%, respectively. The higher IPCE value in gel electrolyte indicates that the backward electron transfer from ZnO conduction band to the electrolyte is lower than that using liquid electrolyte. The higher internal quantum efficiency in semi-solid gel electrolyte based DSSC is achieved.

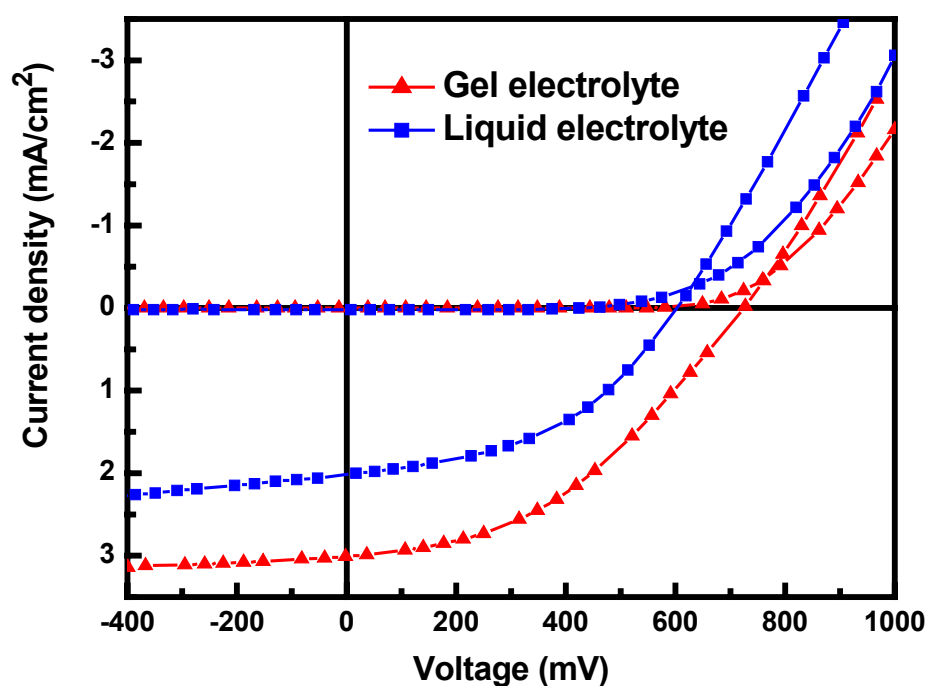


Figure 5.13. I - V characteristics of DSSCs built from $3.2\ \mu\text{m}$ ZnO nanotips impregnated with both liquid electrolyte and gel electrolyte. The photoresponse is measured under the illumination of Xe AM 1.5G simulated sunlight ($100\ \text{mW}/\text{cm}^2$) with a $1.0\ \text{cm}^2$ cell area.

Figure 5.13 compares the photoresponse of DSSCs built from $3.2\ \mu\text{m}$ ZnO nanotips impregnated with MPN-based liquid electrolyte and NMP-based gel electrolyte. The short-circuit current density is $1.9\ \text{mA}/\text{cm}^2$ and $2.9\ \text{mA}/\text{cm}^2$ for liquid and gel electrolyte, respectively. The open circuit voltage, V_{oc} using gel electrolyte is $\sim 726\ \text{mV}$ in comparison to $\sim 610\ \text{mV}$ for the liquid electrolyte counterpart. The V_{oc} increases could be attributed to the negative shift of the conduction band edge of ZnO with respect to the redox potential of I_3^-/I^- couple due to the basicity of NMP molecules that adsorb to ZnO surface. Similar to the case of the observed increase in V_{oc} with in TiO_2 nanoparticle-

based DSSCs using NMP gel electrolyte. [119] An improvement in fill factor is also observed with the NMP gel electrolyte, which leads to higher overall power conversion efficiency. The increase in fill factor is also reflected in the higher parallel resistance of the cells using NMP gel electrolyte. The cells using liquid electrolyte exhibit a power efficiency of 0.77%, and higher power conversion efficiency of 0.89% is achieved when the NMP electrolyte is gelled with 20 wt.% PVDF-HFP (at 100 mW/cm²). The adsorption of NMP molecules at the ZnO surface may also reduce back electron transfer.

The use of NMP gel electrolyte also improves the stability of dye-sensitized solar cells, by slowing down the solvent evaporation and minimizing the dye detachment from the ZnO surface. To evaluate the device stability, aging test is conducted with both liquid NMP and NMP-gelled electrolyte under thermal stress conditions. Both cells are illuminated with halogen light source producing the equivalent of one sun irradiation at the temperature of ~100°C. Figure 5.14 shows power conversion efficiency changes as a function of thermal stress time. Under the same conditions, the power efficiency of the cells with NMP liquid electrolyte rapidly drops by 80% because of rapid solvent evaporation as shown in curve (a). In the case of unsealed cells with NMP-gelled electrolyte, the power efficiency of the cell drops rapidly first, then recovers and is stabilized at 60% of the initial power efficiency as shown in curve (b), which is attributed to better gel impregnation of the ZnO nanotips, and retention of a fraction of the initial solvent contents. The initial decrease of power efficiency may be attributed to the loss of liquid electrolyte contacting the ZnO nanotips; however, after further irradiation (>300 seconds), the melting of the gel onto the surface of the ZnO nanotips causes the efficiency recovery. For DSSC using liquid electrolyte, the sealing is the challenging

issue and yet to be resolved. In comparison, the sealing of the DSSC using NMP-gelled electrolyte can be achieved using epoxy. The curve (c) (Figure 7) shows the power efficiency changes of the cell sealed with epoxy as a function of thermal stress time. The decrease of power efficiency with stress time is slow and rapid efficiency drop is not observed. When epoxy-sealed cells are continuously exposed to one sun of AM 1.5G light, the power conversion efficiency are stabilized at 60% over several hours, and daily repeating tests of the cell efficiency indicates no further degradation over one week period.

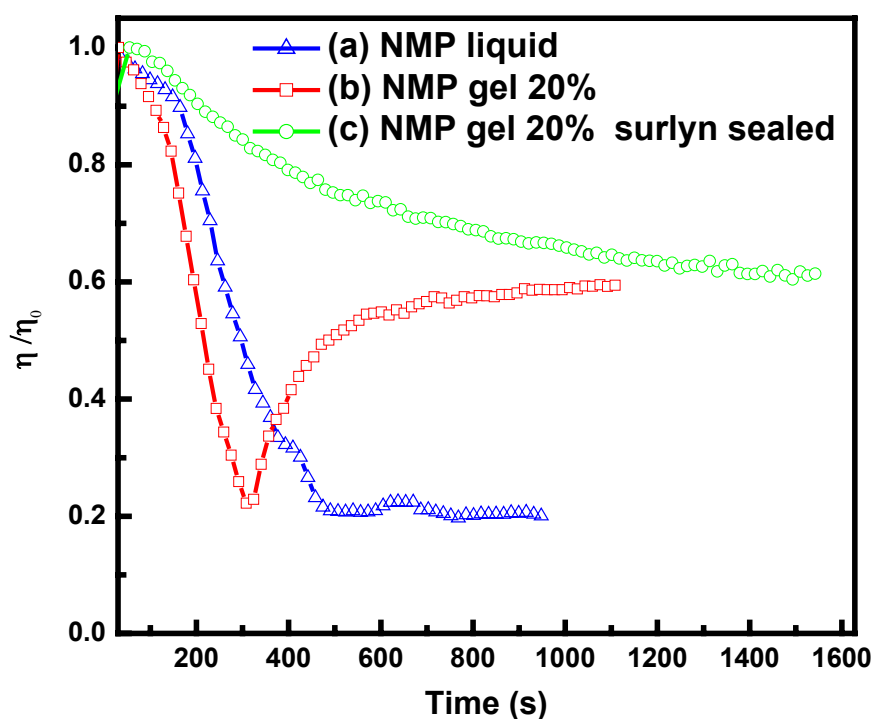


Figure 5.14. Power efficiency changes as a function of thermal stress time under the illumination of halogen light source producing the equivalent of one sun irradiation at the temperature of $\sim 100^\circ\text{C}$.

5.5 Summary

In summary, we demonstrated prototype dye sensitized solar cells using a novel ZnO photoelectrode. The photoelectrode consists of well aligned ZnO nanotips and GZO TCO films. The quantum efficiency and power conversion efficiency are tested using simulated sunlight. It is found that the power conversion efficiency and short circuit of DSSCs increase with the length of ZnO nanotips. The electron transport speed in ZnO nanotips is four times faster than in the ZnO nanoparticles due to the single crystalline quality and direct conduction pathways of ZnO nanotips. A peak IPCE value of 65% at wavelength of ~ 530 nm and a power conversion efficiency of 0.77% is achieved in $3.2\ \mu\text{m}$ ZnO nanotips using liquid electrolyte. In order to improve the device stability, N-Methyl pyrrolidinone (NMP) gelled with poly(vinyl-difluoroethylene-hexafluoropropylene) copolymer (PVDF-HFP) is used as the semi-solid gel electrolyte. It is found that the impregnation of gel electrolyte in ZnO nanotip is relatively easy in comparison to the nanoparticle films. DSSCs using gel electrolyte exhibit higher open circuit voltage of 726 mV and a power conversion efficiency of 0.89% in $3.2\ \mu\text{m}$ ZnO nanotips in comparison to 610 mV and 0.77% for liquid electrolyte. The open circuit voltage increases may be attributed to the negative shift of the conduction band edge of ZnO with respect to the redox potential of I_3^-/I^- couple due to the basicity of NMP molecules that adsorb to oxide surface. Under thermal stress, the efficiency of DSSC using gel electrolyte is stabilized at 60% of the initial efficiency in comparison to 10% using the liquid electrolyte.

Chapter 6 Conclusions and Future Work

6.1 Conclusions

In this dissertation, we developed a novel nanostructured photoelectrode, consisting a Ga-doped ZnO (GZO) transparent conducting film and well-aligned ZnO nanotips, and explored its applications for dye-sensitized solar cells.

Ga-doped ZnO TCO films are grown on glass substrates at low temperature using MOCVD. The growth parameters, such as chamber pressure, substrate temperature and precursor flow ratio, are optimized to achieve GZO films with low sheet resistance and high transmittance. At low growth temperature ($\sim 380^\circ\text{C}$), the GZO films possess a dense polycrystalline structure. As the growth temperature increases above 400°C , the GZO films start forming a columnar structure. It is found that the optimal growth temperature is in the range of $370 \sim 400^\circ\text{C}$. Under the optimal growth conditions, the GZO films (400 nm) have sheet resistance of $\sim 25 \Omega/\text{sq}$ and transmittance over 85% in the visible wavelength. A blue shift of absorption edge in the transmission spectrum is observed in the GZO films due to Burstein–Moss effect associated with high carrier concentration in the ZnO conduction band.

We also demonstrate MOCVD growth of well-aligned ZnO on various substrates, including Si, GaN, c- Al_2O_3 and glass. In comparison to other growth technologies for ZnO nanostructure, MOCVD shows advantages, such as catalyst-free growth, low crystallization temperature, high reproducibility, large area and uniform deposition, *in-situ* doping for tailing the conductivity, and a variety of substrate choices. SEM in conjunction with XRD measurements show that the ZnO nanotips are well aligned along

the substrate surface normal with c-axis preferably orientation. The ZnO nanotips have single crystalline quality and show free exciton emission (3.30 eV) at room temperature. It is found that the formation of well-aligned ZnO nanotips with high aspect ratio results from the highest growth rate of ZnO along the c-axis direction and a subsequent spatial blocking effect. After the random nucleation on the substrate, ZnO nanotips with c-axis parallel to the substrate normal quickly dominate the growth and form a ZnO nanotip array. Due to the narrow space between the neighboring ZnO nanotips, the reacting species can barely access the sidewalls of nanotips. Therefore, the ZnO nanotips quickly increase in length and slowly expand in diameter, resulting in a high aspect ratio.

The combination of GZO TCO films and ZnO nanotips provide a promising nanostructured photoelectrode for dye sensitized solar cells. In the DSSC, GZO films act as the optical window and collecting electrode, while the ZnO nanotips provide large surface for dye molecule anchoring and direct conduction pathways for photogenerated charges. The ZnO photoelectrodes are sensitized with dye RuN3 and are impregnated with either liquid redox electrolyte or semi-solid gel electrolyte. It is found that the power conversion efficiency of the cells increases with the length of ZnO nanotips. By using liquid redox electrolyte, the DSSC built from 3.2 μm ZnO nanotips exhibits a peak quantum efficiency of 65% at $\sim 530\text{nm}$ and a power conversion efficiency of 0.77% under one sun illumination. UV light harvesting, which is directly generated by ZnO photoelectrode, is observed. It is found that electron transport speed in a ZnO nanotip based DSSC is 4~5 times faster than in a nanoparticle-based DSSC. The I - V characteristics of DSSCs are analyzed with a one-diode equivalent circuit model. In order to improve the cell stability, the DSSCs are also impregnated with gel electrolyte. N-

Methyl pyrrolidinone (NMP) gelled with poly(vinyl-difluoroethylene-hexafluoropropylene) copolymer (PVDF-HFP) is used as the semi-solid gel electrolyte. It is found that the impregnation of gel electrolyte into ZnO nanotips is easier than in nanoparticle films as ZnO nanotips are vertically aligned along the substrate surface normal and form straight “trenches” between neighboring nanotips. By replacing the liquid electrolyte with gel electrolyte in the DSSC with the same structure, the open circuit voltage is increased from 610 mV to 726 mV, and the overall power efficiency is increased to 0.89%. The increase in open circuit voltage is attributed to the downshift of the conduction band edge of ZnO with respect to the redox potential of I_3^-/I^- couple. The aging testing shows that the DSSC using gel electrolyte has better stability than its liquid electrolyte counterpart. Under thermal stress, the efficiency of DSSC using a gel electrolyte is stabilized at 60% of the initial power efficiency.

6.2 Suggestions for Future Work

Even with extensive research efforts on dye sensitized solar cells in recent years, this field is still in the early stage of development. ZnO material, including both TCO films and nanostructures, is promising for low cost DSSCs. Further research work is required in order to understand its unique physical and electrical properties and achieve practical device applications. The following directions are recommended for the future research and development of the novel ZnO-based photovoltaic devices:

Ga-doped ZnO TCO films: Sheet resistance and transmittance are the two most important parameters for TCO films. As the polycrystalline GZO film has a high carrier concentration of $10^{20} \sim 10^{21} \text{ cm}^{-3}$, the high electron concentration is countered against high transmittance due to the mobile electron scattering. In such case, improving the electron mobility is the viable approach to achieve high conductivity and transmittance. In order to improve the mobility of GZO films, plasma enhanced CVD growth is preferred. The plasma improves the kinetic energy of reactive species, while reducing thermal budget and improves the crystalline quality, leading to higher electron mobility. By reducing thermal budget, the GZO films is possible to be grown on flexible substrate at low temperature, which will reduce the cost of solar cells.

ZnO Nanotips: MOCVD growth of ZnO nanotips for DSSCs also faces some limitations, which need to overcome. First, the growth rate of ZnO nanotips needs to be significantly improved, therefore, specific reactor designs, including gas flow pattern,

precursor flow rate and chamber pressure, need to be considered. Second, ZnO nanotips can be easily etched by both acid and base solutions; therefore, chemical stability during the dye sensitization and in contact with electrolyte is critical. $\text{Mg}_x\text{Zn}_{1-x}\text{O}$ nanotips are suggested to improve the cell stability. Alloying ZnO with MgO to form a $\text{Mg}_x\text{Zn}_{1-x}\text{O}$ ternary compound can improve the device reliability as the $\text{Mg}_x\text{Zn}_{1-x}\text{O}$ is more resistant to acid and base solutions. Third, undoped ZnO nanotips present a high series resistance in DSSCs. The high sheet resistance reduces the cells' fill factor; therefore, power conversion efficiency. It is suggested to grow ZnO nanotips with *in-situ* Ga doping during MOCVD to provide better cell performance.

Solar Cell Applications: For n-ZnO nanotips/GZO structure-based DSSCs, only preliminary results have been presented and their efficiency has yet to be improved. The advanced solid-state photovoltaic devices have typical efficiency from 5.5% to 12% in commercial solar cell modules. Even though ZnO-based DSSC has high spectral response at certain wavelength. The light absorption of dye molecules in the longer wavelengths is low and more efficient dyes that fully use the solar spectrum need to be developed. For ZnO photoelectrode, the length of ZnO nanotips needs to be further improved to achieve better power efficiency. A new DSSC structure with ZnO nanotip array embedded in nanoparticle film is suggested. It would combine the advantage of ZnO nanotips' faster electron transport speed and nanoparticle films' larger surface area. In this structure, undoped or Ga-doped ZnO nanotips provide grid-like conducting pathways and the nanoparticles provide large surface area for dye anchoring. Solid-state DSSCs either

using p-type ion conductor or polymer gel electrolytes are the future direction, as these devices offer better device stability and are easy for package.

References

1. B. Li, L. Wang, B. Kang, P. Wang, and Y. Qiu, Sol. Energy Mater. & Sol. Cells **90**, 549 (2006).
2. K. Yamamoto, M. Yoshimi, K. Suzuki, T. Tawada, Y. Okamoto, and A. Nakajima, Appl. Phys. A **69**, 179 (1999).
3. J. Yang, A. Banerjee, K. Lord, and S. Guha, Proc. 2nd World Conf. On Photovoltaic Solar Energy Conversion, Vienna, 387 (1998).
4. R. D. Wieting, Proc. 29th IEEE Photovoltaic Specialists Conf., New Orleans, 480 (1998).
5. Y. S. Tyan and E. A. Perez-Albuern. Proc. 16th IEE Photovoltaic Specialists Conf., San Diego, 798 (1982).
6. O'Regan, B. and Grätzel, M. A, Nature (London) **353**, 737 (1991).
7. M. K. Nazeeruddin, A. Kay, I. Rodicio, R. Humphrybaker, E. Muller, P. Liska, N. Vlachopoulos, and M. Grätzel, J. Am. Chem. Soc. **115**, 6382 (1993).
8. T. Minami, Semicond Sci. Technol. **20**, 53(2005).
9. J. W. Bae, S. W. Lee, and G. Y. Yeom, Electrochem. Soc. **154**, 34 (2007).
10. Z. L. Wang, J. Phys.: Condens. Matter. **16**, 829 (2004).
11. W. Park, G.C. Yi, M. Kim, S. J. Pennycook, Adv. Mater. **14**, 1841(2002).
12. K.Keis, E. Magnusson, H. Lindstrom, S.E. Lindquist, and A. Hagfeldt, Sol. Energy Mater. Sol. Cells **73**, 51 (2002).
13. V. Bhosle, A. Tiwari, and J. Narayan, Appl. Phys. Lett. **88**, 032106 (2006).
14. J. Owen, M. S. Son, K. H. Yoo, B. D. Ahn, and S. Y. Lee, Appl. Phys. Lett. **90**, 033512 (2007).
15. O. Dulub, L. A. Boatner, and U. Diebold, Surface Science **519**, 201 (2002).
16. O. Dulub, U. Diebold, and G. Kresse, Phys. Rev. Lett. **90**, N1, 016102 (2003).
17. A. Mang, K. Reimann, and St. Rübenacke, Solid State Commun. **94**, 251 (1995).
18. K.Huemmer, Phys. Status Solidi. B **556**, 249 (1973).
19. Z. K. Tang, G. L. Wong, P. Yu, M. Kawasaki, A. Ohtomo, H. Koinuma, Y. Segawa, Appl. Phys. Lett. **72**, 3270 (1998).
20. N. Ashkenov, B. N. Mbenkum, and C. Bundesmann, J. Appl. Phys. **93**, N11, 126 (2003).
21. K. Vanheusden, C. H. Seager, W. L. Warren, D. R. Tallant, and J. A. Voigt, Appl. Phys. Lett. **68**, 403 (1996).
22. K. Vanheusden, C. H. Seager, D. R. Tallant, J. Caruso, M. J. Hampden-Smith, T .T. Kudas, and J. Lumin, Appl. Phys. Lett. **75**, 11(1997).
23. D. C. Look, D. C. Reynolds, J. R. Sizelove, R. L. Jones, C. W. Litton, G. Cantwell, and W. C. Harsch, Solid State Commun. **105**, 399 (1998).
24. A. F. Kohan, G. Ceder, D. Morgan, and C. G. Van de Walle, Phys. Rev. B **61**, 15019 (2000).
25. C. G. Van de Walle, Phys. Rev. Lett. **85**, 1012 (2000).
26. C. G. Van deWalle, Physica B **308**, 899 (2001).
27. A. F. Kohan, G. Ceder, D. Morgan, and C. G. Van de Walle, Phys. Rev. B **61**, 15019 (2000).

28. D. C. Look, B. Claflin, Ya. I. Alivov, and S. J. Park, *Phys. Stat. Sol.* **201**, N 10, 2203 (2004).
29. D. C. Look, D. C. Reynolds, C. W. Litton, R. L. Jones, D. B. Eason, and G. Cantwell, *Appl. Phys. Lett.* **81**, 1830(2002).
30. A. Tsukazaki, A. Ohtomi, T. Onuma, M. Ohtani, etc, *Nature Materials* **4**, 41 (2005).
31. K. Minegishi, Y. Koiwai, and K. Kikuchi, *Jpn. J. Appl. Phys.* **36**, 1453 (1997).
32. T. Yamamoto and H. Yoshida, *Jpn. J. Appl. Phys. Part 2* **38**, 166 (1999).
33. A. Teke, U. Ozgur, S. Dogan, X. Gu, H. Morkoc, B. Nemeth, J. Nause, and H. O. Everitt, *Phys. Rev. B* **70**, 195207 (2004).
34. U. Ozgur, Ya. I. Alivov, C. Liu, A. Teke, M. A. Reshchikov, S. Dogan, V. Avrutin, S. J. Cho, H. Morkoc, *J. Appl. Phys.* **98**, 041301 (2005).
35. B. K. Meyer, H. Alves, D. M. Hofmann, etc., *Phys. Stat. Sol. B* **241**, 231(2004).
36. Y.P. Varshni, *Physica (Amsterdam)* **34**, 149 (1967).
37. L. Wang and N.C. Giles, *J. Appl. Phys.* **94**, 973 (2003).
38. D.S. Ginley and C. Bright. *MRS Bull.* **25**, 15 (2000).
39. T. Minami, *MRS Bull.* **25**, 38 (2000).
40. T. Minami, *Semicond. Sci. Technol.* **20**, 35 (2005).
41. S. Bose, S. Ray, and A.K. Barua, *J. Phys. D: Appl. Phys.* **29**, 1873 (1996).
42. T. Minami, T. Miyata, and T. Yamamoto, *J. Vac. Sci. Technol. A*, **17**, 1822 (1999).
43. N. Malkomes, M. Vergohl, and B. Szyszka, *J. Vac. Sci. Technol. A* **19**, 414 (2001).
44. B. Szyszka, *Thin Solid Films* **351**, 164 (1999).
45. N. R. Aghamalyan, E.A. Kafadaryan, R.K. Hovsepyan, and S. I. Petrosyan, *Semi. Sci. Technol.* **20**, 80 (2005).
46. G. A. Hirata, J. McKittrick, J. Siqueiros, O. A. Lopez, T. Cheeks, O. Contreras, J. Y. Yi, *J. Vac. Sci. Technol. A* **14**, 791 (1996).
47. N. F. Mott, "Metal-Insulator Transition", Taylor and Francis, London, (1974).
48. V. Bhosle, A. Tiwari, J. Narayan, *Appl. Phys. Lett.* **88**, 032106 (2006).
49. O. Nakagawara, Y. Kishimoto, H. Seto, and Y. Koshido, *Appl. Phys. Lett.* **89**, 091904 (2006).
50. J. Hupkes, B. Rech, S. Calnan, O. Kluth, U. Zastrow, H. Siekmann, and M. Wuttig, *Thin Solid Films* **502**, 286 (2006).
51. J. Springer, B. Rech, W. Reetz, J. Muller, and M. Vanecek, *Solar Energy Materials & Solar Cells* **85**, 1 (2005).
52. J. Song, K. Kim, S. Park, T. Seong, *Appl. Phys. Lett.* **83**, 479 (2003).
53. J. Lim, D. Hwang, H. Kim, J. Oh, J. Yang, R. Navamathavan, and S. Park, *Appl. Phys. Lett.* **85**, 6191 (2004).
54. J. Lim, D. Hwang, H. Kim, J. Oh, J. Yang, R. Navamathavan, and Seong-Ju Park, *Appl. Phys. Lett.* **85**, 6191 (2004).
55. Z. L. Wang, *J. Phys.: Condens. Matter.* **16**, 829 (2004).
56. Y. Wu, H. Yan, M. Huang, B. Messer, J. Song, and P. Yang, *J. Chem. Eurp.*, 1260 (2002).
57. R.S. Wagner, W.C. Ellis, *Appl. Phys. Lett.* **4**, 889 (1964).
58. R.S. Wagner in *Whisker Technology* (Ed.: A. P. Levitt), Wiley, New York (1970).
59. M. Hanson, "Constitution of Binary Alloys", McGraw-Hill Book Co., Inc. (1985).
60. X. Wang, Y. Ding, C. J. Summers, and Z. Wang, *J. Phys. Chem. B* **108**, 8773 (2004).

-
61. H. Yan, R. He, J. Pham, and P. Yang, *Adv. Mater.* **15**, **402** (2003).
 62. D. Zhao, C. Andreazza, and P. Andreazza, *Phys. Stat. Sol. C* **2**, 1137 (2005).
 63. P. Gao and Z. Wang, *J. Phys. Chem. B* **108**, 7534 (2004).
 64. X. Wang, C. J. Summers, and Z. Wang, *Nano Lett.* **4**, 423 (2004).
 65. H. Chik, J. Liang, S. G. Cloutier, N. Kouklin, and J. M. Xu, *Appl. Phys. Lett.* **84**, 3376 (2004).
 66. W. I. Park and G. C. Yi, *Adv. Mater.* **16**, 87 (2004).
 67. B. P. Zhang, N. T. Binh, K. Wakatsuki, Y. Segawa, Y. Kashiwaba, and Kaga, *Nanotechnology* **15**, 382 (2004).
 68. W. I. Park, D. H. Kim, S.W. Jung, G. C. Yi, *Appl. Phys. Lett.* **80**, 4232 (2002).
 69. W. Park, G.C. Yi, M. Kim, and S. J. Pennycook, *Adv. Mater.* **14**, 1841(2002).
 70. J. Zhong, S. Muthukumar, Y. Chen, Y. Lu, H. M. Ng, W. Jiang, and E. L. Garfunkel, *Appl. Phys. Lett.* **83**, 16 (2003).
 71. B. P. Zhang, N. T. Binh, K. Wakatsuki, Y. Segawa, Y. Yamada, N. Usami, M. Kawasaki, and H. Koinuma, *J. Phys. Chem. B*, EST: 3.9 (2004).
 72. K. Ogataa, K. Maejimab, Sz.Fujitac, and Sg. Fujitab, *J. Crystal Growth* **248**, 25 (2003).
 73. D. Lee, J. Park, Y. Yun, Y. Hong, J. Moon, B. Lee, and S. Kim, *J. Crystal Growth* **276**, 458 (2005).
 74. J. Wu, S. Liu, *J. Mater. Chem.* **12**, 3125 (2002).
 75. R. C. Wang, C. P. Liu, J. L. Huang, and S. J. Chen, *Appl. Phys. Lett.* **86**, 251104 (2005).
 76. H. Fan, F. Bertram, A. Dadgar, J. Christen, A. Krost, and M. Zacharias, *Nanotechnology* **15**, 1401 (2004).
 77. J. Jie, G. Wang, Y. Chen, X. Han, Q. Wang, B. Xu, and J. Hou, *Appl. Phys. Lett.* **86**, 031909 (2005).
 78. Y. L. Ji, L. Guo, H. Xu, P. Simon, and Z. Wu, *J. Am. Chem. Soc.*, **124**, 14864 (2002).
 79. F. Fabregat-Santiago, I. Mora-Sero, G. Garcia-Belmonte, and J. Bisquert, *J. Phys. Chem.* **98**, 5552 (1994).
 80. M. Law, L. E. Greene, J. C. Johnson, R. Saykally, and P. Yang, *Nature Materials* **4**, 455, (2005).
 81. E. M. J. Johansson, M. Hedlund, H. Siegbahn, and H. Rensmo, *J. Phys. Chem. B* **109**, 22256 (2005).
 82. K. Keis, E. Magnusson, H. Lindstrom, S. E. Lindquist, and A. Hagfeldt, *Sol. Energy Mater. Sol. Cells* **73**, 51 (2002).
 83. Z. L. Wang, *J. Phys.: Condens. Matter.* **16**, 829 (2004).
 84. W. Park, G. C. Yi, M. Kim, and S. J. Pennycook, *Adv. Mater.* **14**, 1841 (2002).
 85. K. Kim, J. Liu, and L. Carroll, *Appl. Phys. Lett.* **88**, 181911 (2006).
 86. J. B. Baxter, and E. S. Aydil, *Appl. Phys. Lett.* **86**, 053114 (2005).
 87. H. O. Pierson, "Handbook of Chemical Vapor Deposition (CVD)", Noyes Publication, New Jersey, 1992.
 88. J. G. Noltes, Zinc Chemicals, M. Fornsworth and C. H. Kline, Zinc Institute Inc, New York, (1973).
 89. M. H. Abraham, *J. Chem. Soc.* 4130 (1960).

90. K. Vanheusden, C. H. Seager, W. L. Warren, D. R. Tallant, and J. A. Voigt, Appl. Phys. Lett. **68**, 403 (1996).
91. T. Yamamoto and H. K. Yoshida, Jpn. J. Appl. Phys. **38**, L166 (1999).
92. D. G. Thomas and J. J. Lander, J. Chem. Phys. **25**, 1136 (1956).
93. G. A. Shi, M. Saboktakin, M. Stavola, and S. J. Pearton, Appl. Phys. Lett. **85**, 5601 (2004).
94. K. Ellmer, J. Phys. D: Appl. Phys. **34**, 3097 (2001).
95. K. Kakinuma, K. Kanda, H. Yamamura, J. Mater. Sci. **38**, 7, (2003).
96. M. Hiramatsu, K. Imaeda, N. Horio, and M. Nawata, J. Vac. Sci. Technol. A **16**, 669 (1998).
97. V. Assuncao, E. Fortunato, A. Marques, A. Goncalves, I. Ferreira, H. Aguas, and R. Martins, Thin Solid Films **442**, 102 (2003).
98. R. A. Laudise and A. A. Ballman, J. Phys. Chem. **64**, 688 (1960).
99. M. Yan, H. T. Zhang, E. J. Widjaja, and R. P. H. Chang, J. Appl. Phys. **94**, 5240(2003).
100. M. Ritala, M. Leskelä, Nanotechnology **10**, 19 (1999).
101. J. A. Anna Selvana, A. E. Delahoya, S. Guo, and Y. Li, Sol. Energy Mater. Sol. Cells **90**, 3371 (2006).
102. N. R. Aghamalyan, E.A. Kafadaryan, R.K. Hovsepyan, and S. I. Petrosyan, Semi. Sci. Technol. **20**, 80 (2005).
103. S. Muthukumar, H. Sheng, J. Zhong, Z. Zhang, N. W. Emanetoglu, and Y. Lu, IEEE Nanotech. **2**, 50 (2003).
104. K. Vanheusden, C. H. Seager, W. L. Warren, D. R. Tallant, and J. A. Voigt, Appl. Phys. Lett. **68**, 403 (1996).
105. J. Zhong, G. Saraf, H. Chen, Y. Lu, H. M. Ng, T. Siegrist, A. Parekh, D. Lee, and E. A. Armour, J. Electronic Materials, Published online, (2007).
106. T. P. Smith, W. J. Mecouch, P. Q. Miraglia, A. M. Roskowski, P.J. Hartlieb, and R. F. Davis, J. Crystal Growth **257**, 255 (2003).
107. C. R. Gorla, S. Liang, W.E. Mayo, and Y. Lu, J. Appl. Phys. **87**, 3736 (2000).
108. P. Chen, C. Kuo, F. Pan, and T. Tsai, Appl. Phys. Lett. **84**, 3888 (2004).
109. C. R. Gorla, N. W. Emanetoglu, S. Liang, W. E. Mayo, M. Wraback, H. Shen, and Y. Lu, J. Appl. Phys. **85**, 2595 (1999).
110. M. Ohring, "Materials Science of Thin Films Deposition and Structure", Academic Press, (1990).
111. J. A. Aranovich, D. G. Golmayo, A. L. Fahrenbruch, R. H. Bube, J. Appl. Phys. **51**, 4260 (1980).
112. Neil A. Anderson and T. Lian, Annu. Rev. Phys. Chem. **56**, 491, (2005).
113. J. Krüger, R. Plass, M. Grätzel, P. J. Cameron, and L. M. Peter, J. Phys. Chem. B **107**, 7536 (2003).
114. J. Nelson, Phys. Rev. B **59**, 15374 (1999).
115. J. Van de Lagemaat and A. J. Frank, J. Phys. Chem. B **105**, 11194 (2001).
116. S. Rühle and D. Cahen, J. Phys. Chem. B **108**, 17946 (2004).
117. J. Nelson, Phys. Rev. B **59**, 374 (1999).
118. K. Tennakone, V. P. S. Perera, I. R. M. Kottegoda, and G. Kumara, J. Phys. D: Appl. Phys. **32**, 374 (1999).

-
119. M. G. Kang, K. M. Kim, K. S. Ryu, S. H. Chang, N. G. Park, and K. J. Kim, *J. Electrochem. Soc.* **151**, E257 (2004).

Curriculum Vita

HANHONG CHEN

EDUCATION BACKGROUND

- Sep. 1995 – June 1999
B. S. In Materials Science and Engineering
Zhejiang University, Hangzhou, China
- Sep. 1999 – June 2002
M.S. In Materials Science and Engineering
Zhejiang University, Hangzhou, China
- Sep. 2002 – Jan. 2008
Ph. D. In Electrical and Computer Engineering
Rutgers, the State University of New Jersey, New Jersey

RESEARCH EXPERIENCE

Research projects in Rutgers University (June 2004 – Jan. 2007)

1. MOCVD growth and property characterization of ZnO and $\text{Mg}_x\text{Zn}_{1-x}\text{O}$ films and nanostructures on various substrates.
2. Development of Ga-doped ZnO transparent conducting oxide films using MOCVD.
3. Dye sensitized solar cells using ZnO nanotips and Ga-doped ZnO TCO films.
4. Fabrication and characterization of ZnO/p-Si heterojunction diodes.
5. Fabrication and characterization of ZnO-based transparent thin film transistors.

Research projects in Zhejiang University (Sep. 1995 – June 2002)

1. Growth of ZnO films using DC and RF magnetron sputtering.
2. Material characterization using XRD, SEM, TEM, XPS, Hall, etc.
3. Material characterization of PZT electronic ceramics.

TEACHING EXPERIENCE

1. Teaching assistant, *Introduction to Electrical Engineering*, (Sep. 2002 - June 2004).

PUBLICATIONS

Journal Papers

1. “Dye sensitized solar cells using Nanostructured Photoelectrode and Gel electrolyte”, **H. Chen**, A. Du Pasquier, Z. Duan, Y. Lu, submitted to *J. Appl. Phys.* (2007).
2. “ZnO TFT Devices Built on Glass Substrates”, J. Zhu, **H. Chen**, G. Saraf, Z. Duan, Y. Lu and S. T. Hsu, submitted to *TMS & IEEE J. Electronic Materials* (2007).

3. "Dye sensitized solar cells using ZnO nanotips and Ga-doped ZnO film", **H. Chen**, G. Saraf, J. Zhong, Y. Lu, and A. Du Pasquier, accepted to *Semi. Sci. and Tech.* (2007).
4. "Interface Properties of ZnO Nanotips Grown on Si Substrates", **H. Chen**, J. Zhong, G. Saraf, Y. Lu, D.H. Hill, S. T. Hsu, Y. Ono, *TMS & IEEE J. Electronic Materials* 35, 1314 (2006).
5. "Properties of ZnO nanotips selectively grown by MOCVD", **H. Chen**, J. Zhong, G. Saraf, Z. Zhang, Y. Lu, L. A. Fetter, and C. S. Pai, *Proceedings of SPIE* 5592-31, 164 (2004).
6. "Integrated ZnO Nanotips on GaN Light Emitting Diodes for Enhanced Emission Efficiency", J. Zhong, **H. Chen**, G. Saraf, Y. Lu, C.K. Choi, J.J. Song, D.M. Mackie, and H. Shen, *Appl. Phys. Lett.* 90, 203515 (2007).
7. "Dye Sensitized Solar Cells using well-aligned ZnO Nanotip Arrays", A. Du Pasquier, **H. Chen**, and Y. Lu, *Appl. Phys. Lett.* 89, 253513 (2006).
8. "Fast and Reversible Wettability Transitions of ZnO Nanostructures", Z. Zhang, **H. Chen**, J. Zhong, G. Saraf, and Y. Lu, *TMS & IEEE J. Electronic Materials* 36, 895 (2007).
9. "Structural and Optical Properties of ZnO Nanotips Grown on GaN Using Metalorganic Chemical Vapor Deposition", J. Zhong, G. Saraf, **H. Chen**, Y. Lu, H. M. Ng, T. Siegrist, A. Pwerekh, D. Lee, and E. A. Armour, *TMS & IEEE J. Electronic Materials* 36, 654 (2007).
10. "Fast Electron Transport in MOCVD Grown Dye-sensitized ZnO Nanorod Solar Cells", E. Galoppini, J. Rochford, **H. Chen**, G. Saraf, Y. Lu, A. Hagfeldt, G. Boschloo, *J. Phys. Chem. Lett. B* 110(33), 16159 (2006).
11. "ZnO nanotips Grown on Silicon Substrates by Metal-Organic Chemical-Vapor Deposition", J. Zhong, G. Saraf, S. Muthukumar, **H. Chen**, Y. Chen, and Y. Lu, *TMS & IEEE J. Electronic Materials*, 33, 654 (2004).
12. "Binding studies of molecular linkers to ZnO and MgZnO nanotip films", O. Taratula, E. Galoppini, D. Wang, D. Chu, Z. Zhang, **H. Chen**, G. Saraf, and Y. Lu, *J. Phys. Chem. B* 110, 6506 (2006).

Patent

1. "Integrated ZnO Nanotips and Transparent Conductive Films for Photovoltaic Devices", Y. Lu, A. Du Pasquier and **H. Chen**, US patent (provisional), 2007.